Continuous Artery Monitoring Based on Decomposition of Ultrasound Radiofrequency Signals

By

Shane Steinberg

A thesis submitted to the Faculty of Graduate and Postdoctoral Affairs in partial

fulfillment of the requirements for the degree of

Master of Applied Science

in

Biomedical Engineering

Carleton University

Ottawa, Ontario, Canada

Abstract

Ultrasound can noninvasively monitor the mechanical and dynamical properties of the artery. Scattering and overlap of adjacent tissue boundary echoes with those from the artery wall affect the estimation accuracy of the artery properties and impede continuous and automatic monitoring. Decomposition of the ultrasound radiofrequency (RF) signals using matching pursuit with particle swarm optimization is proposed to isolate the echoes arising from the tissue boundaries of the carotid artery wall for subsequent estimation of the wall thickness and diameter changes during the cardiac cycle. The proposed method exhibited less variance in the estimation of artery wall thickness when compared to manual estimation by a clinical method. Artery wall motion tracking by the proposed method was more robust compared to tracking achieved through the conventional cross-correlation technique when applied to the ultrasound RF signals from a wearable ultrasound sensor that contain a high volume of scattering echoes.

Acknowledgement

I extend my sincere gratitude to my academic supervisors, Dr. Y. Ono and Dr. S. Rajan, for their investment in my development as an engineer and applied scientist. They have been instrumental in the enhancement of my technical communication skills and application of the scientific method. During this research they have offered abundant encouragement and support.

Special thanks to the Natural Sciences and Engineering Research Council of Canada, and the Carleton University COVID-19 Rapid Response Grant for financial support during this thesis.

Thanks for my mother, J. Kulp and S. Iaboni for their support and encouragement during this thesis research. Thanks to my colleagues A. Fernandes, and K. Tran for our discussions. I am also grateful to S. Venugopoal for making the *in-vivo* data available for use in this thesis.

Contents

List of Figures

List of Tables

Acronyms

IMT   Intima-Media Thickness. v, viii, ix, xi, 6–8,
         24–27, 33–36, 49–51, 53–72, 77, 84, 85

M-mode   Motion-mode. iii, iv, vii, ix, x, 14, 15, 22, 24,
         30, 31, 34–36, 39, 41, 42, 50–52, 54, 65–69,
         72–79, 82, 84, 85, 88

MP   Matching Pursuit. 44–46, 50, 69, 84, 87

PVDF   Polyvinylidene Diflouride. 18–20, 91

RF   Radio-frequency.   viii–x, 2–8, 12–14, 21–23,
         26, 27, 29–39, 41, 42, 45–47, 49–51, 53, 55–
         58, 60, 61, 64, 65, 67, 68, 72–75, 79, 84–86,
         88, 91

UT   Ultrasonic Transducer. vii, ix, 2, 5, 6, 9, 12–
         17, 21, 22, 30, 31, 33, 37, 41, 42, 65–67, 91

WUS   Wearable Ultrasound Sensor. vii, ix, x, 3–5,
         7, 9, 15, 18–24, 29–34, 54, 64, 72, 73, 75–78,
         83, 85, 86, 91

Glossary

B FWHM bandwidth of GMS echo model.

J Cost function for matching pursuit.

R Residual of MP iteration.

T Sample time interval.

Δ Displacement estimate of isolated echo.

α Bandwidth factor of the GMS echo model.

β Magnitude of the GMS echo model.

δ IMT estimate.

ϕ Phase of the GMS echo model.

θ Parameter vector of the GMS echo model.

c Speed of sound in biological tissue.

d Depth location of the GMS echo model.

g GMS echo model.

s Model of M-mode ultrasound.

x Depth.

Chapter 1

Introduction

1.1 Overview

As the aging population in Canada continues to grow to an expected 25% of the total population through the next 60 years [1], there will be an increase in demand for healthcare. One of the feasible and desirable solutions to meet the increasing demand for care of the elderly could be remotely and automatically monitoring the health of subjects in their homes [2]. A serious health concern among older populations is the risk of developing cardiovascular diseases (CVD). Approximately 12% of those aged 60 to 64 are currently estimated to have CVDs in Canada, and this estimation increases steeply to 31% by age 75 to 79 [3]. Early identification and continuous monitoring of risk indicators along with appropriate interventions are therefore crucial in mitigating and preventing disease progression [4].

Health indicators that are obtained through monitoring the artery dynamics and structure may be used to assess the state of the cardiovascular system. Motion

tracking of the artery walls during the cardiac cycle and measurement of the arterial

diameter and wall thicknesses can be achieved using appropriate sensors. From these

measurements, properties of the cardiovascular system such as the viscoelasticity of

the artery tissues and the continuous blood pressure [5] can be estimated and used

to assess cardiovascular health.

Ultrasound imaging is commonly used for clinical assessment of the arteries ow-

ing to its non-invasiveness and ability to characterize the dynamical properties of

biological soft tissues [6]. Automatic and continuous monitoring of the artery proper-

ties using ultrasound is hindered by its inherent resolution limitations and scattering

noises in the acquired ultrasound radiofrequency (RF) signals. The finite frequency

bandwidth of the ultrasonic transducers (UTs) determines the spatial pulse-width

of the acquired ultrasound and thus controls the depth resolution of the system.

This depth resolution limitation and the multiple echoes arising from tissues adja-

cent to the artery can result in interference with the echoes reflected from the tissue

boundaries of the artery wall, obscuring their precise location. This creates difficulty

when seeking to automatically identify the location of the artery tissue boundaries

for the subsequent estimation of the structural and dynamical properties. Errors

in the quantitative assessment of the artery structure and dynamics may change

the physiological interpretation of the acquired ultrasound data [7]. Therefore, the

ability to isolate the echoes reflected from the tissue boundaries of the artery wall

may be beneficial for methods of automatic and continuous artery monitoring using

ultrasound.

For instance, artery wall thicknesses are commonly evaluated using a clinical

ultrasound imaging system that employs focused ultrasound beams. Echoes from the artery wall tissue layers are used to determine the thicknesses of the artery wall layers for cardiovascular diagnosis [8]. The boundary location of each tissue layer may be obscured if the axial resolution is greater than the layer thickness to be estimated, or if there are adjacent tissue echoes within the distance of the axial resolution. In these cases, an overlap with the tissue boundary echoes of the artery wall will occur and can introduce errors in the estimated thickness.

Furthermore, isolation of the echoes arising from the artery wall has applications in emerging health monitoring technologies using ultrasound. A wearable ultrasound sensor (WUS) system using non-focused ultrasound beams has been proposed for long-term, automatic, and hand-free monitoring of artery dynamics and diameter [9]. The ultrasound signals acquired by this WUS for artery monitoring contain a high volume of scattering echoes. This is caused by the reduced lateral resolution of the WUS (see **Appendix A.2**), a property that is determined by the unfocused beam and large area of the sensor. This complicates the automatic identification and isolation of the artery wall boundaries for tracking the diameter changes over the cardiac cycle. For example, the method of artery wall motion tracking in [9] requires manual identification of the initial location of the artery wall boundary echo, which is often challenging given the high volume of scattering in the acquired ultrasound RF signals from the WUS.

A method that can isolate the artery wall boundary echoes from interference is beneficial for accurate and automatic monitoring of the artery using ultrasound. This has application for conventional clinical ultrasound imaging systems, in addi-

tion to emerging WUS systems.

1.2 Problem Statement

Isolation of the echoes reflecting from the tissue boundaries of the carotid artery wall is beneficial for accurate, continuous, and automatic monitoring using ultrasound. Overlap of these echoes arises due to the limited axial or lateral resolution of the ultrasound system, in addition to scattering echoes in the acquired ultrasound RF signals. Development of a digital signal processing (DSP) algorithm is required to isolate the echoes reflecting from the tissue boundaries of the artery and subsequently monitor cardiovascular parameters, such as the thickness of the artery wall tissues and the diameter changes during the cardiac cycle.

1.3 Objective

This thesis concerns the preliminary development of a DSP algorithm that can isolate the echoes arising from the tissue boundaries of the carotid artery wall (hereafter called the "artery wall echoes") within acquired ultrasound RF signals, and subsequently estimate the artery wall layer thickness and diameter change during the cardiac cycle. Towards this goal, the following objectives are defined:

1. **Develop a model of the ultrasound RF signal composed of multiple echoes.**

   A model of the acquired ultrasound RF signals is to be developed and used as a framework for investigating DSP algorithm development for isolation and

tracking of the artery wall echoes. The signal model will incorporate prior knowledge about the ultrasound system (ultrasound frequency and bandwidth of the UT) and account for the acoustic properties (sound speed) of biological soft tissue.

2. **Develop DSP algorithms to isolate the desired echoes in ultrasound RF signals for thickness estimation of the artery wall and tracking of artery wall motion.**

   Based on the mathematical equation of the ultrasound RF signal model, a DSP algorithm to isolate the desired artery wall echoes is to be developed. In addition, methods for estimating the tissue layer thickness of the artery wall and tracking the motion of the isolated artery wall echoes will be developed.

3. **Evaluate the proposed methodology with numerical simulation and *in-vivo* experiments.**

   Numerical simulation experiments will be performed to evaluate the feasibility of the proposed method for artery wall thickness estimation with varied thicknesses and ultrasound frequencies. *In-vivo* experiments will be conducted using a clinical focused ultrasound system and the WUS system for preliminary evaluation of the proposed method. The efficacy of the proposed method for its use in artery wall echo isolation, wall thickness estimation, and motion tracking will be discussed.

1.4   Contributions

This thesis presents the following contributions:

- **A mathematical model of the ultrasound RF signals is developed based on prior knowledge of the ultrasound system characteristics.**

  The ultrasound RF signal is modelled as a summation of Gaussian modulated sinusoidal (GMS) echoes. Decomposition of the acquired ultrasound RF signals to their composing echoes assumed by the mathematical model is performed by matching pursuit and optimized using particle swarm optimization.

- **A technique for estimating the intima-media thickness (IMT) is developed using the signal model.**

  A technique for estimating the IMT using the parameters of the echo model is developed. The thickness is estimated using the echo model parameters that correspond to the appropriate tissue boundaries of the artery wall.

- **A technique for tracking the motion of isolated echoes is developed based on the signal model.**

  A technique for motion tracking based on the parameters of the echo model is developed. The motion is estimated by computing the phase change of the echo model parameters across successive ultrasound RF signals obtained by a UT.

- **The proposed method is evaluated by numerical simulation and *in-vivo* experiments.**

Numerical simulation experiments were performed to evaluate the accuracy of the proposed method for IMT estimation with varying thickness and ultrasound frequency. For realistic IMT values $(0.4 - 0.8$ mm), the error was less than 0.025 mm with simulation conditions imitating the clinical ultrasound system used in this thesis. When evaluating the effect of the ultrasound frequency on the accuracy, the upper limit of errors in the IMT estimates for 5 MHz or above was 20%.

The proposed method demonstrated less variance in the IMT estimates using *in-vivo* ultrasound data obtained by a clinical ultrasound imaging system when compared to manual estimation by a clinical method. Artery wall motion estimation by the proposed method was more robust to the high volume of scattering echoes in the ultrasound RF signals obtained using the WUS when compared to the conventional cross-correlation (CC) technique of motion estimation.

1.5   Publications

The research performed in this thesis resulted in the following publications:

Conferences:

- S. Steinberg, Y. Ono, S. Rajan, and S. Venugopal, "Continuous artery wall motion tracking using flexible and wearable ultrasonic sensor by signal decomposition", *Proc. IEEE International Conference on Flexible, Printable Sensors and Systems*, pp. 1-4, June, 2021.

- S. Steinberg, K. Tran, S. Rajan, Y. Ono, "Estimation of intima-media thickness of carotid artery by ultrasound radiofrequency signal decomposition using matching pursuit", *Proc. IEEE International Ultrasonics Symposium*, Sept, 2021.

Magazine:

- S. Steinberg, A. Huang, Y. Ono and S. Rajan, "Continuous artery monitoring using a flexible and wearable single-element ultrasonic sensor", *IEEE Instrumentation and Measurement Magazine*, (Submitted, 2021).

1.6   Organization

Chapter 2 details background information on the artery physiology and anatomy and the ultrasound systems and data used in this work.

Chapter 3 provides a literature review of existing algorithms for IMT estimation and artery wall motion tracking using ultrasound.

Chapter 4 provides a description of the received ultrasound RF signal model, reviews signal decomposition methods, describes the proposed signal decomposition method, and presents the motion tracking and IMT estimation methods.

Chapter 5 presents and discusses the results of numerical simulation and *in-vivo* experiments using the proposed methodology for IMT estimation and artery wall motion tracking.

Chapter 6 concludes the thesis work accomplishments and describes areas of future research.

Chapter 2

Technical Background

This chapter provides an overview of the related technical background of the artery physiology, medical ultrasound systems, and fundamental concepts used in this work.

Section 2.1.1 contains details of the physiology and anatomy of the artery. The relation of the artery mechanical properties to cardiovascular health assessment is discussed.

Section 2.2 details the fundamentals of medical ultrasound imaging and the ultrasound systems used in this work. Details of the WUS and clinical ultrasound systems are given as well as discussion of the UT material properties of each. The relevant ultrasound modes for artery motion monitoring are described, and example images are given from *in-vivo* measurements of the carotid artery. A description of the *in-vivo* human experiment configuration is given.

2.1 Artery

2.1.1 Physiology

The arteries are blood vessels that are responsible for the circulation of oxygen and nutrients throughout the body. The structure of the artery wall is composed of smooth muscle fibers, elastic tissue, and structural support layers that expand and contract with the changes in blood pressure experienced over the cardiac cycle. This viscoelasticity of the artery tissue is an important feature of the circulatory system that helps to damp the rapid changes in blood pressure that would otherwise be experienced at the peripheral arteries where perfusion of nutrient-carrying blood to the organs occur [10]. This aids in the maintenance of the conditions required for blood perfusion to the organs. Thus, the mechanical properties of the arteries are important indicators that are used to assess the state of cardiovascular health. Often, this is quantified through parameters such as the arterial compliance, stiffness, diameter, and the characteristics of the pulsatile motion of the artery walls during the cardiac cycle [11]. Further discussion of the artery properties used for evaluation of the cardiovascular health is presented in **Section 3**.

2.1.2 Anatomy

Fig.2.1 shows an illustration of the layered structure of the artery wall. Three distinct layers, namely, the adventitia, the media, and the intima form the structure of the artery. This composite structure of the artery wall produces the viscoelastic properties that enable hemodynamic regulation [13]. Degradation of the tissue
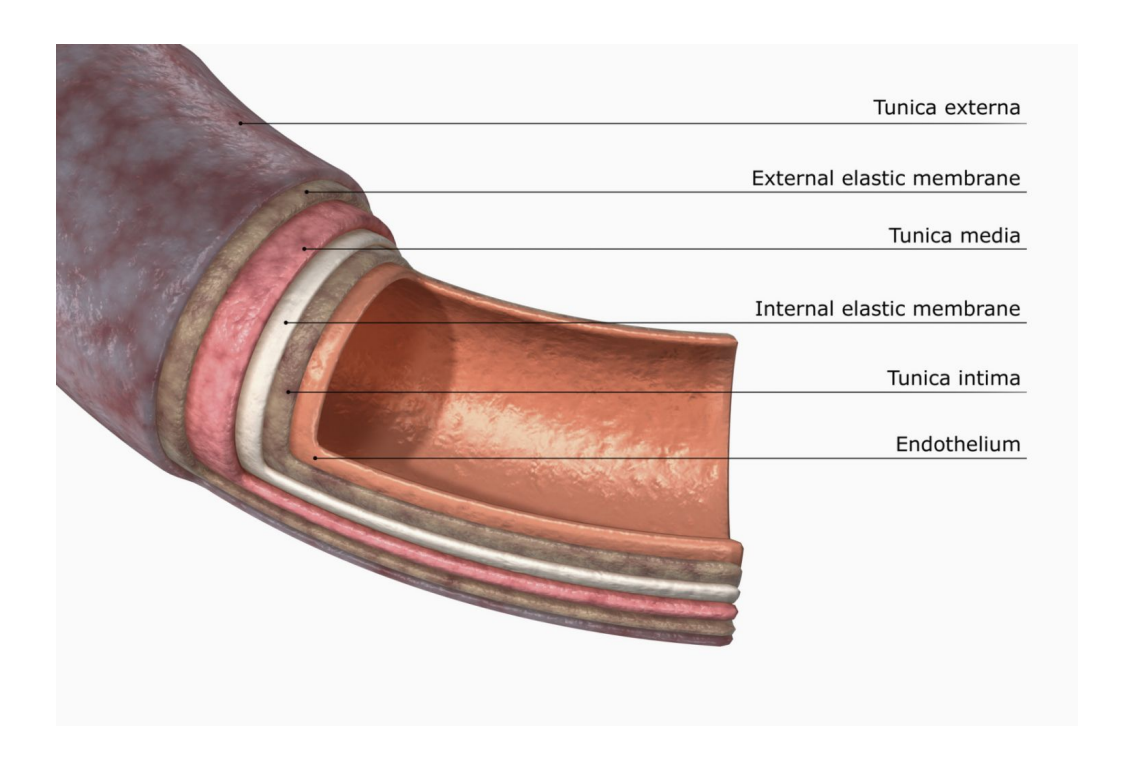
Figure 2.1: *Layered structure of the artery wall tissues. Illustration adapted from*
[12].

properties in each layer can lead to a variety of health issues and disease.

The outermost layer, called the adventitia or externa, consists mainly of con-
nective tissues that provide structural support to prevent excessive expansion and
contraction of the vessel over the cardiac cycle. The media is the middle layer
and primarily consists of smooth muscle fibers and an elastic membrane that fa-
cilitates the change in vessel diameter responsible for regulating changes in blood
pressure and volume. The elastic fibers are nonrenewable after infancy and degrade
with age, leading to stiffening of the artery and contributing to the development of
hypertension-related organ damage [14]. The intima is the innermost layer made up
of endothelial cells that provide a selectively permeable membrane to contain the
blood cells while allowing the diffusion of various other substances [15]. Dysfunc-

tion of the endothelial cells results in impaired diffusion of the vessel and is a risk indicator for atherosclerosis and other cardiovascular diseases [16], [17].

2.2   Ultrasound Data Acquisition Modes

Medical ultrasound imaging is a noninvasive imaging modality that makes use of high frequency (> 20 kHz) sound waves to probe internal structures of the body. In the ultrasound pulse-echo technique [18], UTs are electrically excited to produce pulsed ultrasound waves that propagate into the monitored area. When the ultrasound pulse travels through an interface of two materials with differing acoustic impedance, some of the acoustic energy is reflected back toward the UT and is recorded for analysis (see **Appendix A.1** for additional information on scattering conditions). These pulse-echo ultrasound signals contain information regarding the physiological structure of the tissues in the propagation path and can be used for visualization and tissue characterization of tendons, muscles, vessels, and internal organs [19]. Several modes of ultrasound data acquisition are used in medical imaging, characterized by different UT and excitation configurations [20].

2.2.1   A-mode

Amplitude-mode (A-mode) is the fundamental ultrasound RF data. A UT sends an ultrasound pulse into the tissue and the ultrasonic echoes reflected from tissue boundaries in the media are acquired. This results in a signal that contains structural information of the tissues along the depth in the propagation path. Fig.2.2 shows an ultrasound RF signal in A-mode that was obtained from the carotid artery. The

artery wall echoes are at 15 mm (near wall) and 24 mm (far wall). These echoes correspond to the tissue interfaces of the artery walls.
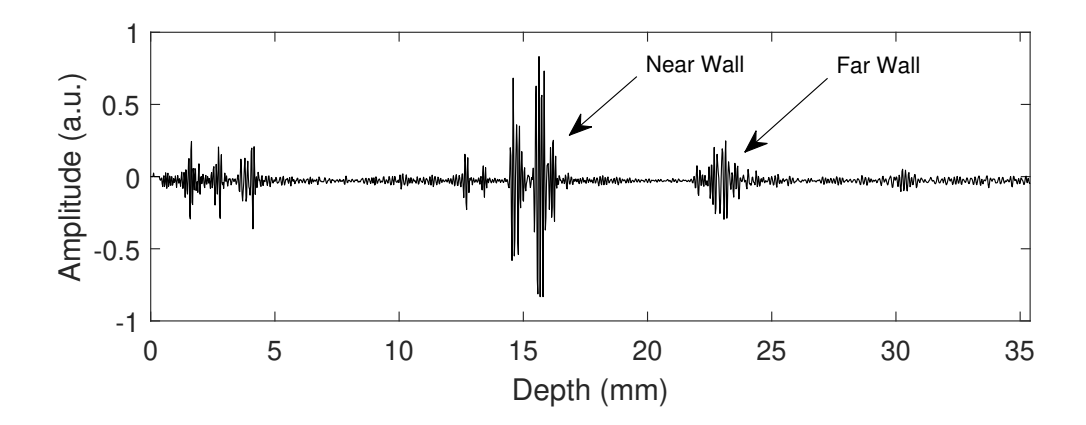
Figure 2.2: *A-mode signal of the carotid artery.*

2.2.2   B-mode

Using an array of UTs, a series of A-mode signals can be obtained by scanning the ultrasound beam along the geometry of the UT array. The resulting set of ultrasound RF signals contain lateral spatial information in addition to the depth spatial information of each A-mode (see **Section A.2** for discussion on the resolution of ultrasound systems). Further processing of the set of acquired ultrasound RF signals to obtain the envelopes results in a cross-sectional image called the Brightness-mode (B-mode) image. This image can be used to visualize subcutaneous structures of the body in 2-dimensions. Fig.2.3 shows a B-mode image of the carotid artery along the longitudinal direction. The near and far walls of the artery appear at approximately 17 mm and 24 mm, respectively. The A-mode scanline corresponding to Fig.2.2 is indicated.
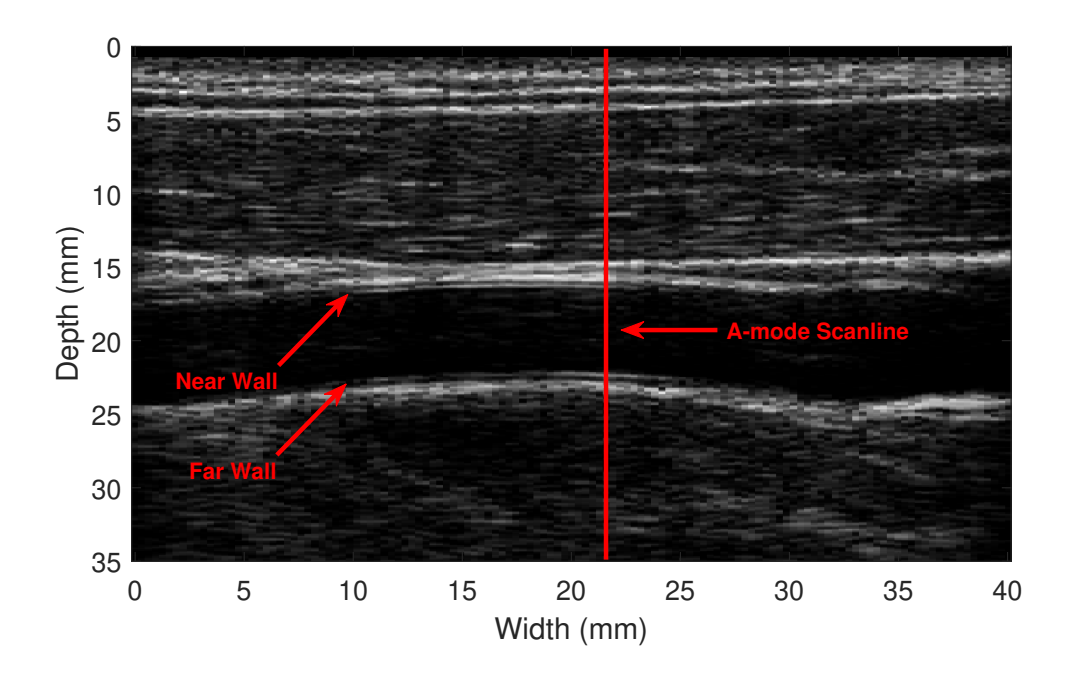
Figure 2.3: *Longitudinal B-mode image of the carotid artery.*

2.2.3 M-mode

Motion-mode (M-mode) images are formed by acquiring ultrasound RF signals from a single UT in regular succession with respect to an acquisition interval. The envelopes of these RF signals can be computed, and displayed as an image which contains temporal and depth information. This can capture the dynamics of the reflecting tissues in the depth information of the image. Fig.2.4 displays an M-mode image of the carotid artery over a period of 6 seconds. The motion of the artery walls can be seen at 12.5 mm and 20 mm.
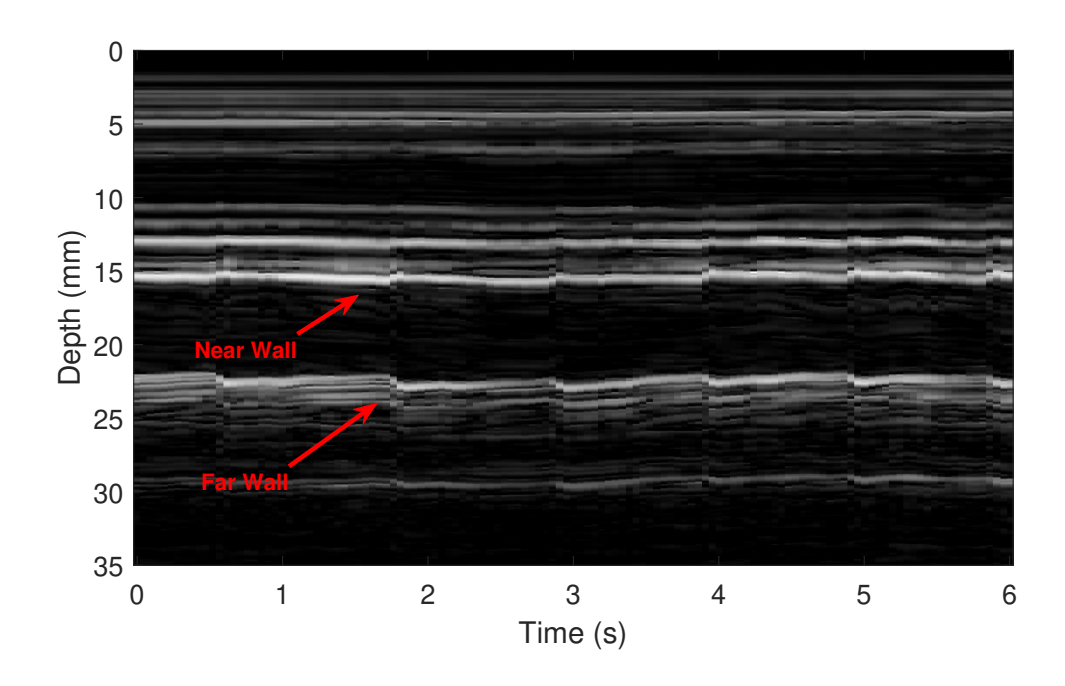
Figure 2.4: *M-mode image of the carotid artery.*

2.3   Ultrasound Data Acquisition Systems

Ultrasound data acquisition systems are composed of a piezoelectric UT, an excitation system, and a data acquisition system. The piezoelectric characteristics of the UTs used for excitation and the acquisition conditions of the ultrasound data affect the resulting signal quality. These characteristics include the emitted ultrasound frequency and bandwidth, sensing area of the UT, and electro-mechanical conversion efficiency. A clinical ultrasound imaging system and the WUS system [9] were used for *in-vivo* experiments in this work. The following subsections detail the system characteristics used for the experiments in this work and provide discussion of the measurement model for artery monitoring.

2.3.1 Clinical Ultrasound Imaging System

Fig.2.5 a) and b) show the clinical ultrasound imaging system (Model: PICUS, Esaote Europe) and a linear array ultrasound imaging probe (Model: L10-5 Esaote, Europe). A similar system was used for the *in-vivo* experiments in this research. The sampling rate of the clinical imaging system was 33.3 MHz (corresponds to 23 μm depth sampling interval), and the B-mode image frame rate was 30 Hz. Assuming the ultrasound frequency was 7.5 MHz, the axial resolution was roughly 300 μm (estimated from the spatial pulse-width). The lateral resolution at 7.5 MHz is comparable to the wavelength at the focal point: approximately 205 μm assuming the speed of sound is 1540 m/s.

(a)   (b)
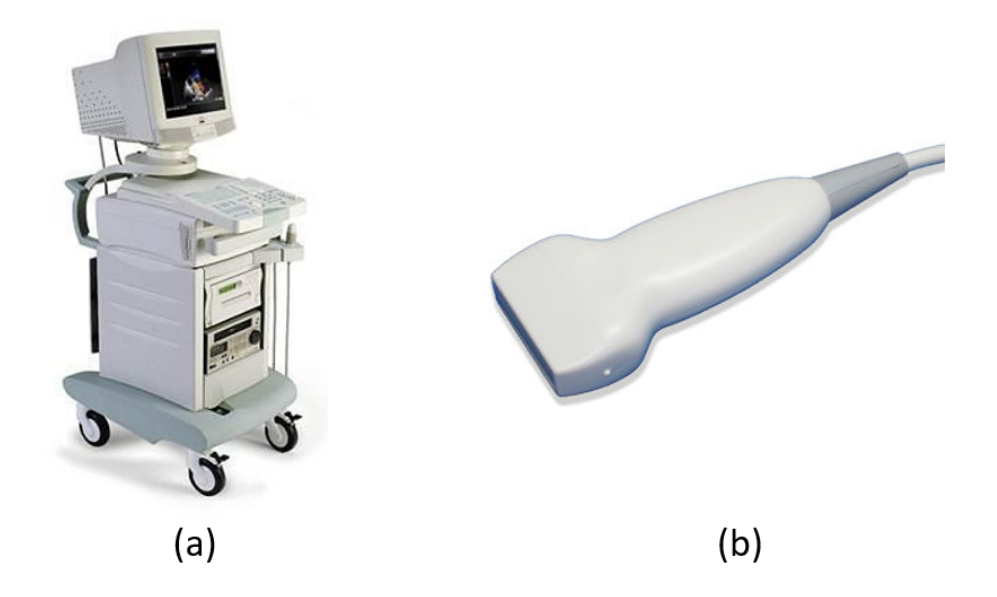
Figure 2.5: *a) PICUS clinical ultrasound imaging system used for in-vivo experiments. b) Linear array ultrasound imaging probe.*

The clinical probe contains 128 UTs in a linear array that spans 40 mm. Each UT is 315 μm wide and can emit focused ultrasound beams that result in high-

resolution cross-sectional B-mode images. The simple beamforming algorithm used by the clinical system results in ultrasound data that can only detect motion that is parallel to the propagation direction.

2.3.1.1 Measurement Model
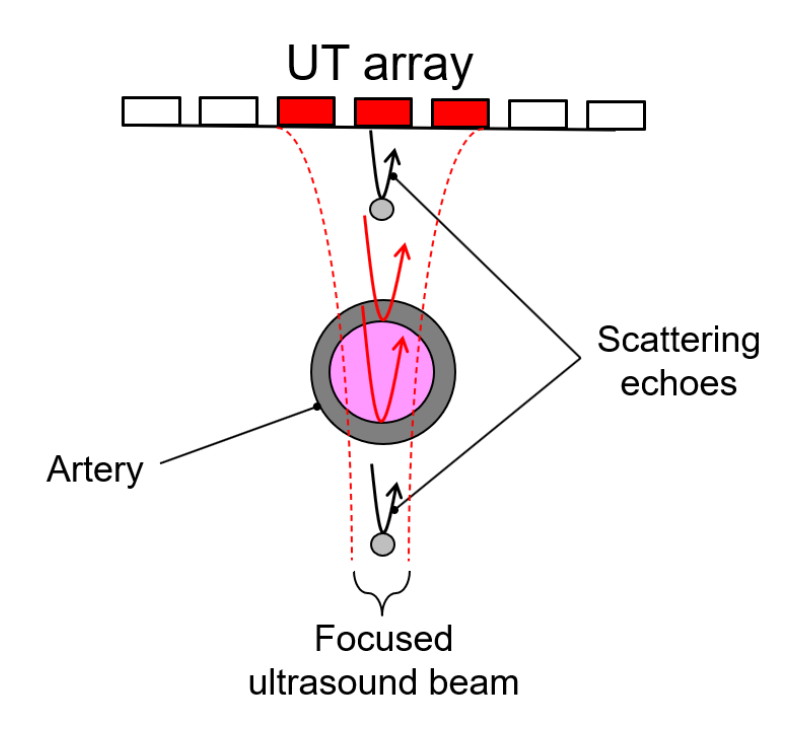
Figure 2.6: *An illustration of the measurement model for artery monitoring using the focused beam of the UTs from the clinical ultrasound imaging system.*

Fig.2.6 illustrates the ultrasound signal model for artery monitoring using the clinical ultrasound imaging system. The linear array of ceramic UTs produce a focused ultrasound beam and have a width smaller than the artery diameter. Thus, the probe must be centered over the diameter cross-section of the artery to obtain accurate measurement of the artery diameter and wall thicknesses. The focused ultrasound beam and small sensing area of the ceramic UTs in the clinical imaging

probe produce a relatively low amount of scattering echoes in the acquired signals compared to the WUS.

2.3.2   Wearable Ultrasound Sensor System

WUS systems are emerging technologies that have a variety of applications for continuous biomedical monitoring. Estimating the muscle contractile parameters using a WUS system has been demonstrated [21]. This has implications for assessment of the muscle properties during physical training and rehabilitation, as well as for the diagnosis and monitoring of neuromuscular disorders. In [22], the authors proposed a WUS system using an array of ultrasonic transducers (UTs) for measurement of the bone motion *in-vivo* for sports medicine and surgical navigation applications. The feasibility of prosthetic control through evaluation of the muscle and tendon activity in the forearm using WUS technology has been recently demonstrated by predicting the individual finger flexions [23], [24]. Inferring the desired hand movement using the ultrasound signals has demonstrated advantages over the more conventional surface electromyography sensor approach that is hindered by low signal-to-noise ratio and lack of spatial information of the deep tissues. In this research, monitoring the artery motion and diameter changes using the WUS is considered.

2.3.2.1   Piezoelectric Material

The WUS is constructed out of polyvinylidene diflouride (PVDF), a piezoelectric polymer film possessing desirable characteristics for wearable biomedical monitoring such as flexibility and light weight [25]. PVDF is also a low-cost material making

the sensor disposable, a useful feature for monitoring where sterile conditions are required. In addition, PVDF has an acoustic impedance close to biological soft tissue, thereby removing the requirement for acoustic matching layers to ensure propagation of the acoustic waves into the monitored tissue area [26], [27]. Although a matching layer is not strictly necessary to ensure propagation into the monitoring area, PVDF polymer requires a high excitation voltage compared to piezoceramic UTs due to the relatively high dielectric and mechanical losses [28]. Thus, the WUS was excited using a laboratory ultrasonic pulser/receiver system (Model: DPR300, JSR Ultrasonics, Pittsford, NY, USA) for the *in-vivo* experiment. The laboratory ultrasonic pulser is capable of producing high voltage (100-475 V) impulses that overcome the weak electro-mechanical conversion of the PVDF film and result in received ultrasound pulse-echo signals that penetrate to depths suitable for monitoring the far wall of the artery.

The WUS was excited at a pulse repetition frequency of 1 kHz and the received pulse-echo signals were digitally sampled at 125 MHz. It is noted that for a fully wearable device, the excitation voltages and sampling rates are impractical. However, for preliminary development of the DSP algorithm for artery monitoring, avoiding the additional technical challenges associated when operating under power constraints allows the problem of motion tracking to be worked on in isolation.

2.3.2.2   Design and Construction

Fig.2.7 a) depicts a schematic diagram of the WUS structure. The WUS was designed and constructed in the biomedical engineering lab at Carleton University [27]. The WUS was constructed from a PVDF piezoelectric polymer film having a
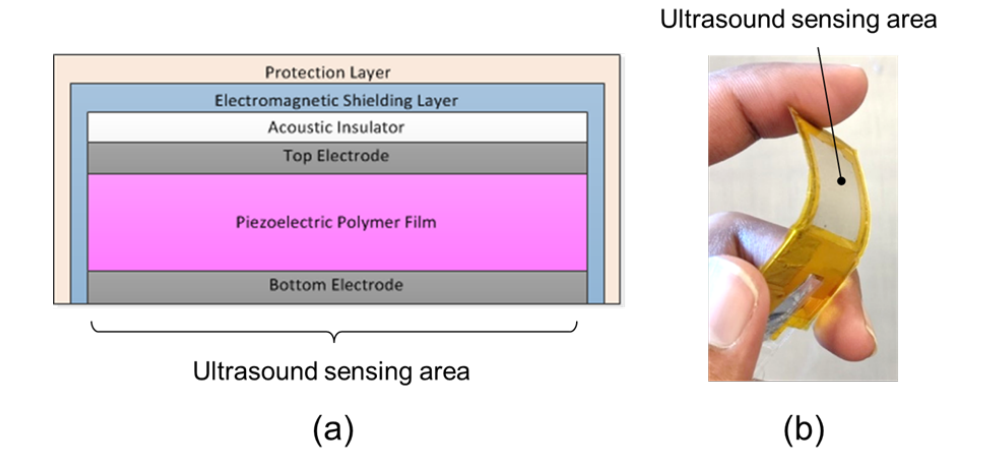
Figure 2.7: *a) Schematic diagram of the WUS structure. b) A photograph of the constructed WUS.*

top and bottom electrode. The ultrasonic active sensing area is determined by the overlapping area of the top and bottom electrodes. The sensing area was selected to be large enough to cover the artery of interest even with slight lateral motion shifts of the artery during the measurements. The sensor was covered by an acoustic insulator and electromagnetic shielding layer for acoustical and electrical noise shielding, respectively. The outer layer is a protection layer that uses non-conductive polymer films for sensor protection, electrical insulation, and waterproofing. The sensor is flexible and lightweight so that it can be attached onto a curved and deformable body surface without deforming underlying soft tissues such as the artery or restricting the underlying tissue motion.

A photograph of the constructed WUS is presented in Fig.2.7 b). It had an active ultrasonic area (electrode size) of 20 mm by 20 mm, and the total thickness and the weight of the sensor were 0.2 mm and less than 1 g, respectively. A single-layer PVDF film was used for the WUS in this study; however, the film thickness and

number of piezoelectric film layers of the sensor may be designed based on desired

ultrasonic characteristics (center frequency and bandwidth) [21].

2.3.2.3   Measurement Model
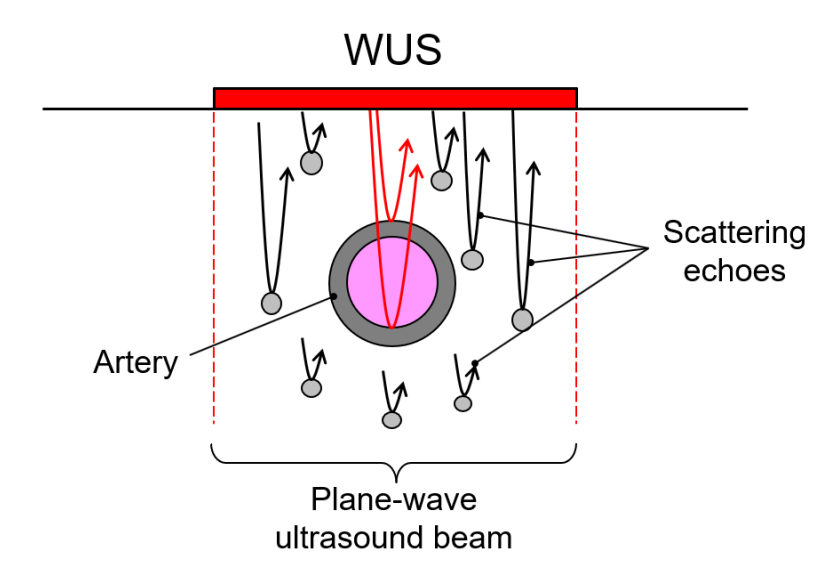
Figure 2.8: *An illustration of the measurement model for artery monitoring using the WUS with a plane-wave ultrasonic beam.*

Fig.2.8 illustrates the ultrasound signal model for artery monitoring using WUS. The WUS composed of a single-element UT emits plane-wave ultrasound beams with widths greater than the diameter of an artery. The plane-wave emission and large sensing area of the WUS introduces more scattering echoes from adjacent tissues to the artery, obscuring the artery wall echoes in the acquired ultrasound RF signals.

2.4 *In-vivo* Human Experiment

An *in-vivo* human experiment was conducted with the approval of the Carleton University Research Ethics Board. Due to COVID-19 pandemic limitations preventing the ability to acquire data over the course of this thesis research, the data used in [29] was also used in this research work. Ultrasound RF signals were obtained at the common carotid artery (CCA) of a healthy human subject using both the clinical imaging system and the WUS system. A cardiovascular specialist guided the *in-vivo* data acquisition. Obtaining the B-mode images of the carotid artery using the clinical ultrasound imaging system required the probe array to be centered over the mid-point of the longitudinal direction of the artery. The WUS does not require precise placement of the UT due to the large surface area and therefore is easier to use than the clinical ultrasound imaging system. The data used in this work consisted of a 6 second B-mode image recording using the clinical ultrasound imaging system, and a 4 second M-mode image using the WUS.
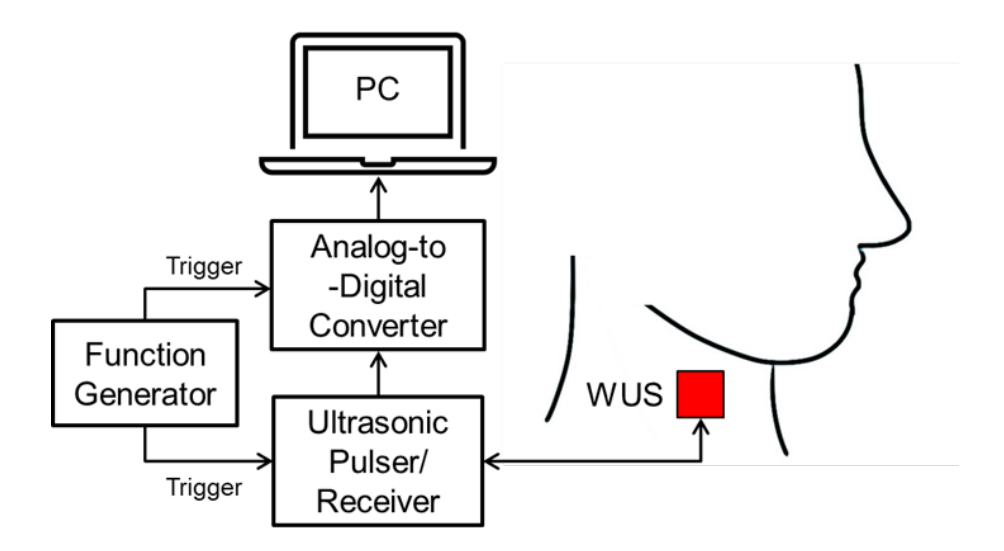
Figure 2.9: *A block diagram of the measurement configuration for artery moni-toring using the WUS.*

The system configuration for artery monitoring using the WUS in the pulse echo technique is shown in Fig.2.9. As shown, the WUS was secured over the CCA. The WUS was attached on the skin surface of a subject with a layer of ultrasonic couplant material between the sensor and skin surface. The ultrasound couplant material could be liquids, gel, adhesives, glues, adhesive tape, or double-sided adhesive film, for instance. The WUS was driven by an ultrasonic pulser/receiver. The ultrasound RF signals received by the pulser/receiver was digitized by an analog-to-digital converter and sent to a personal computer for signal analysis.

Chapter 3

Literature Review

This chapter provides a literature review of existing methods for artery wall motion tracking, and IMT estimation using ultrasound. Both B-mode and M-mode ultrasound are discussed for each.

Section 3.1 reviews literature on IMT estimation techniques using ultrasound. Considerations for IMT estimation when the resolution is lowered and when there is overlap of the tissue boundaries are discussed.

Section 3.2 reviews literature on motion tracking techniques using B-mode and M-mode ultrasound. The limitations preventing application of the existing methods to the WUS system are discussed for each.

Section 3.3 summarizes the literature review and highlights the shortcomings of the existing methods for motion tracking and IMT estimation.

3.1   Intima-Media Thickness Estimation

The intima-media thickness (IMT) is a measurement of the combined thickness of the two innermost layers of the artery wall - the intima and media [30] (shown in Fig.2.1). It is used to quantify the degree of atherosclerosis, a disease caused by the buildup of plaques on the endothelial cells of the intima layer [31]. The thickness of the layer of endothelial cells cannot be assessed directly using ultrasound due to resolution constraints of the system. Thus, the thickness of the intima-media complex is used as surrogate measure to quantify the degree of atherosclerosis [32]. The carotid IMT also serves as an important risk factor for ischemic stroke and myocardial infarction [33], [34]. 0.1 mm increments in the carotid IMT correspond to 10-15% increase in myocardial infarction risk, and 13-18% increase in stroke risk [35], thus there is a need for precise IMT estimation.

The spatial pulse-width of a received echo is dependent on the ultrasound sys-
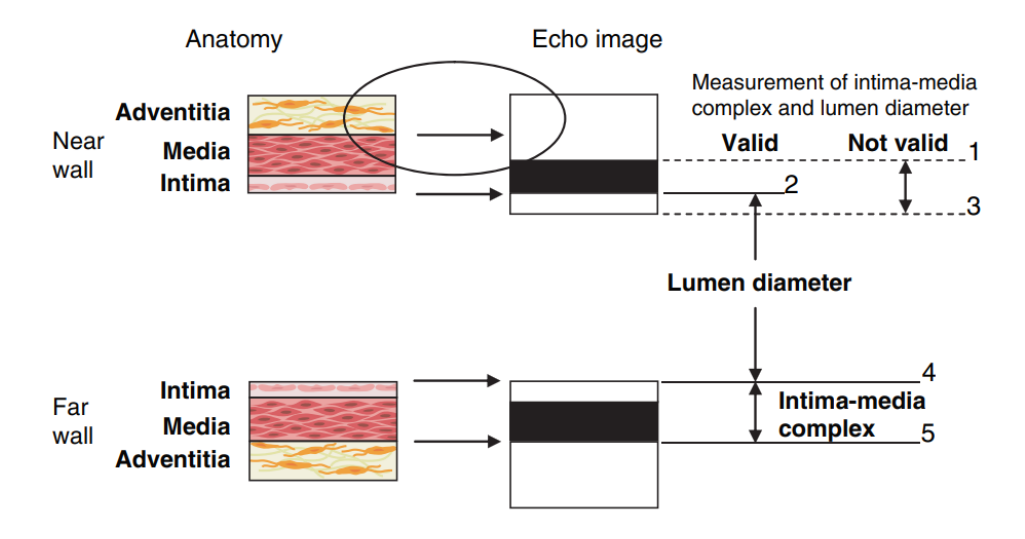
Figure 3.1: *Illustration of the leading edge method of IMT and lumen diameter measurement. Figure adapted from [36].*

tem used for imaging and does not provide anatomical information. Thus, manual estimation of the IMT using ultrasound images is generally done by medical professionals. In this manual estimation, IMT is defined as the interval between the upper edges of the echoes corresponding to the lumen-intima and media-adventitia boundaries [36]. Fig.3.1 illustrates this method of IMT estimation. The leading edge, defined as the upper border of the echo envelope, is used for all manual thickness measurements with ultrasound images. Accordingly, this method relies on the resolution of the ultrasound system (i.e., spatial pulse-width and image pixel resolution) to be high enough so that the leading edges of the boundary layer echoes are well defined.

Several automatic segmentation methods based on the B-mode image have been proposed for IMT estimation [37]. These include parametric contour fitting of the boundary layers in the B-mode image [38], estimation of the local envelope statistics for identification of the wall boundaries based on tissue characterization [39], dynamic programming [40], and utilization of the Hough transform for boundary identification [41]. Almost all of the segmentation methods in the literature employ B-mode imaging. As B-mode analysis is computationally expensive, such IMT estimation algorithms may not be suitable for continuous and automatic artery monitoring. Alternatively, IMT estimation using the RF signal has high computational efficiency compared to B-mode image techniques [42] and is therefore considered in this research work.

B-mode methods usually rely on high frequency ultrasound with center frequency 7 to 17 MHz [37], [43] to produce clearly defined artery wall tissue boundaries. For

assessing the IMT of non-superficial major arteries, such as the aorta, the upper limit of the ultrasound frequency that can be used is constrained due to the frequency-dependent attenuation in biological tissues. Thus, the existing methods may not be suitable for ultrasound systems operating at lower frequencies or when the tissue boundaries used for IMT estimation are occluded by scattering noises from adjacent tissues. Use of the RF signal decomposition for isolation of the appropriate tissue boundaries in cases where the lower resolution and scattering interferences produce overlapping echoes could be one approach to improving the IMT estimation accuracy. Further discussion on this is presented in **Section 4.4**.

3.2   Artery Wall Motion Tracking

As mentioned in **Section 2.1.1**, the artery wall is an elastic tissue that expands and contracts with changes in blood pressure during the cardiac cycle. This mechanical property of the artery wall tissue is important for hemodynamic regulation. Reduction of the tissue elasticity, known as arterial stiffening, occurs due to the loss of elastin with age [44], plaque buildup [45], and hypertension [46]. This has widespread detrimental impact on the cardiovascular function.

Artery stiffening generally precedes thickening of the vessel wall (assessed through the IMT) in the development of atherosclerotic disease [47], [48]. Large fluctuation in blood pressure at the peripheral arteries caused by the inability of the arteries to damp these changes is damaging to the organs with low vascular resistance, such as the brain and kidneys [49]. This is linked to stroke, dementia, and cognitive decline [50]. Further, artery stiffness is used as a risk indicator for myocardial infarction

and all-cause mortality [51]. In addition to the extensive damage caused by artery stiffening, a positive feedback between hypertension and increased stiffness also exists [52], [53]. Thus, early identification and intervention is beneficial to reduce the progression of CVD.

Stiffness of the artery may be assessed by analysis of the diameter changes during the cardiac cycle [54]. This requires accurate motion tracking of the artery walls during the cardiac cycle. Ultrasound offers a noninvasive method of assessment; however, the current manual delineation of these diameter changes in the resulting measurements is highly time-consuming and subject to human error [55]. Therefore, accurate and automated motion tracking of the artery walls has received considerable attention in the literature.

3.2.1   B-mode Techniques

Currently, most of the existing literature for artery motion tracking utilize B-mode imaging. This section provides a review of existing B-mode methods.

Block matching techniques [56] have been widely applied to artery wall motion tracking. To implement block matching for motion estimation, an image segment is first windowed, then the centroid (spatial mean) of the pixels within the window is computed. The maximum correlation of the centroids between two B-mode images is computed to obtain the estimated displacement across the images. Longitudinal motion of the artery was estimated using block matching in [57]. In [58], block matching was used to estimate the artery motion parallel to the ultrasound propagation direction. In [59], the authors propose a block matching approach for

estimating the arterial wall movements in two dimensions. Block matching is a model-free approach to motion estimation that uses correlation of local envelope statistics in an area of the B-mode images to compute the relative displacement across frames. It is therefore sensitive to scattering and measurement noise in the B-mode image area used for motion estimation.

To address the sensitivity to noise and resolution limitations that corrupt the local statistics in the conventional block matching, the authors in [55], [60] presented a model based on a state space representation of the artery dynamics. The state function of the artery dynamics is assumed to be described as a Van der Pol oscillator, and the state variation is assumed to be described by a Markov process. To approximate the nonlinear dynamics of the artery, a nonlinear state transfer function was used. An unscented Kalman filter based on the block matched observations was used to estimate the state variations of the artery wall [61]. This method again relies on the centroid of an image segment as the input to the state space model. Estimating the displacement across frames using local statistics may not be suitable for application to the WUS system because of the plane-wave emission that introduces a high volume of additional scattering in the signals. Errors could be introduced by these additional echoes when computing the centroids in each frame, leading to inaccurate displacement estimation.

Recently, a deep learning method for artery motion tracking using ultrasound RF signals in B-mode was proposed in [62]. Using a Siamese neural network architecture of fully convolutional neural networks [63], adjacent scanlines of the ultrasound RF signals in a region of interest were matched using a similarity score of the cor-

responding feature maps. This method was proposed to improve the accuracy of the motion estimates compared to block matching. While the simulation studies presented in the paper indicate the possibility of extracting dynamics using the M-mode RF signals with this technique, this method faces limitations that could prevent straightforward implementation in the WUS system: deep learning methods do not provide interpretability of the resulting predictive model. Further, automatic identification and isolation of the wall boundary echoes using the RF signal was not considered, with the focus of the study being on improving the accuracy of the motion estimate over conventional block matching. Additionally, successful implementation of deep learning models usually require a high volume of labelled training data due to the large number of model parameters [64].

Similarity measures are generally used to determine the displacement across frames in most of the B-mode tracking algorithms. For instance, CC is a commonly used technique for estimating the displacement across successive images. Local statistics or features from the B-mode image segments may be used for computation of these similarity measures. These techniques generally work well when focused UTs are used, due to the sensitivity of the local statistics and features to noises in the image segments. A short survey of the literature that use correlation techniques for motion tracking in M-mode is given in the next subsection.

3.2.2   M-mode Techniques

Motion tracking of the artery wall using the M-mode sequence of RF ultrasound signals has received less attention in the literature compared to B-mode image tech-

niques. However, for motion tracking, M-mode methods generally require fewer computations compared to the B-mode as the latter requires additional processing to construct the B-mode image from an array of UTs. Reducing computational complexity could be a necessity while implementing the WUS system for long-term and continuous monitoring as tracking using M-mode leads to lower power, memory and computational requirements. Further, compared to envelope-based methods of signal processing, using the time-series of A-mode ultrasound RF signals allows the extraction of useful phase information from which robust motion estimation can be inferred. Thus, artery monitoring techniques based on the RF ultrasound signals acquired in M-mode may lead to robust motion tracking.

Methods of motion tracking using M-mode sequences of ultrasound RF signals that have been previously proposed include Doppler [65], thresholding [66], and phase locking techniques [67], [68]. Doppler techniques are prone to errors arising from mismatch in the demodulation frequency. Thresholding may fail to capture the artery wall echo due to attenuation. Phase locking is sensitive to the axial window size [69]. Auto-correlation motion estimation [70] based on the ultrasound RF signals in M-mode is a popular approach. This method estimates the relative phase change across quadrature-demodulated RF signal segments via auto-correlation with a reference signal. While this method can yield accurate motion estimation under certain conditions, it still requires the quadrature demodulated signal, and is therefore sensitive to the demodulation frequency. This can lead to inaccuracy in the motion estimate if there is a mismatch between the carrier and demodulation frequency.

One approach to address this issue was proposed in [71], where a Gaussian spec-

trum of the ultrasound RF signal was assumed, and a derivation for motion estimation via complex CC of the RF signals without assuming the demodulation frequency was obtained. This method reduced underestimation of the displacement across frames due to the demodulation mismatch. However, the method is sensitive to the window size and does not provide the absolute depth information of motion estimates.

Additional dynamic echoes and random interference caused by scattering within the signal can cause errors when estimating the motion across two frames via correlation of the ultrasound RF signal segments. Unfortunately, the CC motion estimation only produces a relative motion estimate, meaning the absolute depth of the artery wall echo to be tracked is still required to be known. For automatic and continuous motion tracking of the artery wall using the WUS, a method that is more robust to random interference and additional echoes within the signal segment used for motion estimation is required.

In [69], [72], the authors describe an artery wall motion tracking technique based on dynamic time warping that addresses some limitations of CC methods. To address the failure of the CC in the presence of additional dynamic echoes within the signal segment used for motion estimation, the authors introduced additional flexibility to the signal model via a nonlinear warping map that allows the amplitude and time information to vary across successive frames. The CC assumes a static signal model between two frames, with the only difference being the relative shifts in phase containing the motion. Random interference and the presence of additional dynamic echoes within the signal segment can violate this assumption leading to

inaccuracies in the result. By incorporating the additional flexibility into the signal model, the motion estimation exhibited increased robustness to interference from additional echoes in the signal segment.

While this method addresses primary limitations of CC-based motion tracking, the assumptions made for the automatic identification of the wall echoes may be too simplistic for the high scattering noise of the WUS. It was assumed that the high amplitude and out-of-phase dynamic echoes corresponded to the artery wall; however, for the WUS this may not be a valid assumption due to the increased volume of scattering echoes in the acquired RF signals. This approach was implemented using a UT with higher lateral resolution than the WUS and thus does not suffer from the severity of scattering noise encountered when using the WUS. The high volume of additional dynamic and static echoes in the acquired signals may require a more sophisticated method of artery wall echo isolation and tracking.

3.3   Summary

Most existing techniques for artery monitoring using ultrasound rely on B-mode images for motion tracking and IMT estimation.

IMT estimation based on the RF signal has received less attention than image-based methods using the envelope of the signals. Current methods make use of the B-mode image, but assume the tissue boundaries are well resolved as a result of the high ultrasound frequencies used [37], [43]. When the tissue boundaries used for IMT estimation are not well resolved due to the ultrasound frequencies used or interfering scattering noise, the accuracy of the estimates could be reduced.

Techniques of motion tracking based on the correlation of ultrasound RF signals in M-mode have been previously proposed, but have received less attention in the literature. The existing M-mode motion tracking methods can fail in the presence of a high volume of interfering scattering echoes in the signal segments used for motion estimation [69], [72]. Thus, the existing M-mode methods may need to be improved to solve the problem of isolating and tracking the specific echo corresponding to the artery wall boundary in the noisy signals obtained using the WUS.

The following chapter proposes a RF signal decomposition methodology for IMT estimation and artery wall motion tracking. Additional discussion of supporting literature for the signal decomposition is also presented. IMT estimation is handled under a signal decomposition methodology and could offer a technique that allows the isolation of the artery wall echoes used for IMT estimation when the resolution and interference results in overlap of the echoes. For motion tracking, the signal decomposition approach is extended to isolate and track desired echoes in the received RF signals, avoiding the problem faced using the CC motion estimators, and creating the opportunity for automatic identification of the artery wall echoes.

Chapter 4

Methods of Ultrasound RF Signal Decomposition and Artery Monitoring

This chapter describes the proposed method of ultrasound RF signal decomposition for IMT estimation and artery wall motion tracking. The proposed method uses a mathematical model of the ultrasound echo that is based on the spatial impulse response of the ultrasound system. Each ultrasound RF signal is assumed to be a summation of the echoes arising from the artery wall and surrounding tissue boundaries. IMT estimation is performed using the echo parameters corresponding to the lumen-intima and media-adventitia boundaries within the artery wall. M-mode sequences of ultrasound RF signals are the time series of the ultrasound RF signals. Each RF signal in an M-mode sequence is decomposed into its constituent echoes using a greedy algorithm known as matching pursuit [73]. This algorithm iteratively

estimates the parameters of the echoes comprising the ultrasound RF signal. Then, the parameters corresponding to an artery wall echo in an M-mode sequence are used to estimate the artery wall motion.

Section 4.1 presents the mathematical model of the echo and ultrasound RF signals used in this work. The model of the M-mode sequence is detailed, and the problem of artery monitoring using the models is explained.

Section 4.2 reviews the matching pursuit approach for signal decomposition that is used in this thesis. A discussion is presented to compare matching pursuit to other signal decomposition approaches, such as regression-based deconvolution and wavelet-based signal decomposition. Considerations regarding the implementation of the matching pursuit algorithm for optimally estimating the echoes are discussed.

Section 4.3 discusses the particle swarm optimization algorithm for use in optimizing the cost function used by matching pursuit in each iteration of the signal decomposition. Advantages and limitations of the particle swarm optimization are also detailed.

Section 4.4 contains the IMT estimation and artery wall motion tracking approaches using the parameters in the proposed RF signal and echo models. An IMT estimation approach using the parameters of the lumen-intima and media-adventitia boundary echoes is presented. An artery wall motion tracking method using the parameters of the isolated wall boundary echo is presented.

4.1   Modelling Ultrasound RF Signals

In the pulse-echo technique, the acquired ultrasound RF signals contain echoes from tissue boundary structures in the propagation path of the ultrasound wave. These echoes contain information related to the properties of the reflecting structures, such as their location and echogenicity. Additional acoustic characteristics of the propagation media, such as the frequency-dependent attenuation of the media, can also be inferred through analysis of the ultrasound signal [74]. Thus, the information contained in the echoes of the acquired ultrasound RF signal are essential for interpretation of the underlying structure and dynamics of the probed tissue media.

Ultrasonic frequency, pulse-width, and beam size of the ultrasound system impose spatial resolution limitations. This limitation may lead to overlap of the echoes in the acquired signals. UTs have a finite bandwidth which determine the spatial width of the transmitted ultrasound pulse. Thus, the finite bandwidth determines the axial resolution, and the ultrasound beam size determines the lateral resolution [75]. One way to increase the spatial resolution would be to increase the ultrasound frequency. However, since the acoustic attenuation in biological soft tissues increases with frequency [76], the frequency of the emitted pulse cannot be increased arbitrarily. This poses a challenge when seeking to resolve fine tissue structures such as the artery wall layers within the acquired RF signals.

Reflectors that are spaced closer together than the spatial pulse-width of the ultrasound echo result in overlap of the echoes due to those reflectors [77]. Interference of these echoes can obscure the true boundary location of the reflectors and cause a misinterpretation of the underlying tissue structure. In addition, an echo
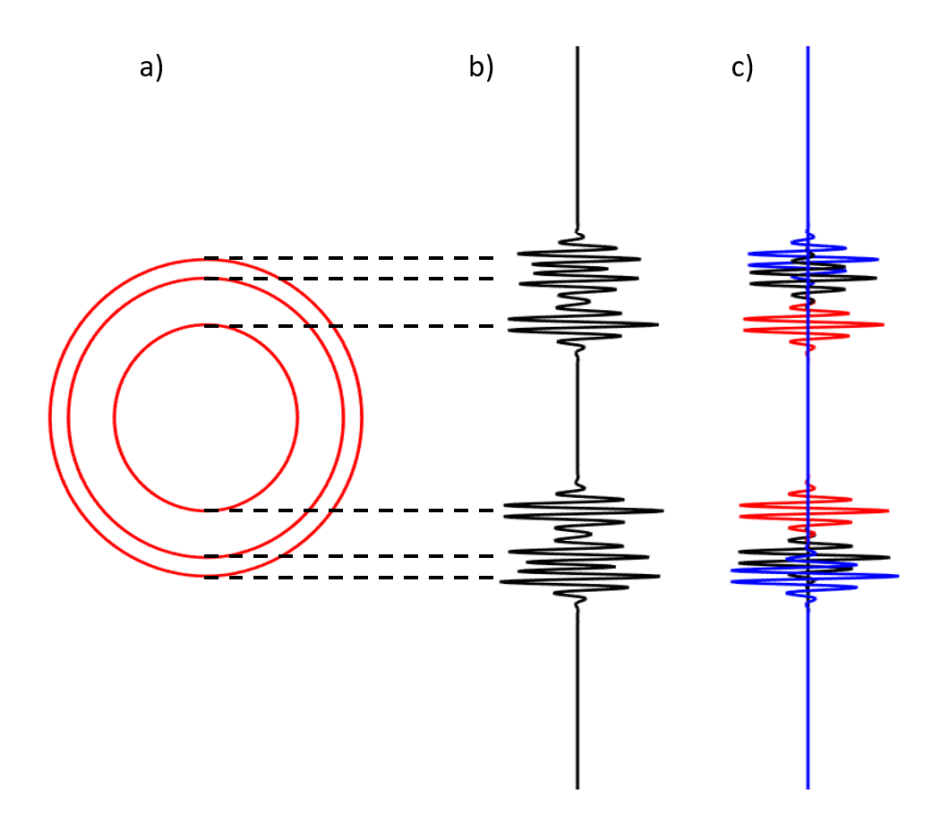
Figure 4.1: *a) Illustration of layered structure of artery containing three radial tissue boundaries. b) Acquired ultrasound RF signal from cross-section of artery structure. c) Decomposed echoes corresponding to the tissue layer boundaries.*

from a boundary where the tissue media composing the interface have close acoustic impedance may have a small echo amplitude due to the resulting low echogenicity. Therefore, a method that can isolate specific echoes under these conditions is useful for identifying the desired artery wall boundary echoes within the received ultrasound RF signals for the artery monitoring applications discussed in this thesis research.

Fig.4.1 shows a) an illustration of the tissue structure of an artery, b) acquired ultrasound RF signal from the structure, and c) decomposed echoes arising from each tissue layer boundary. The acquired RF signal contains overlapping echoes

that obscure the true boundary locations of the tissue layers. However, the acquired
signal is a summation of echoes from each boundary. Isolation of each echo comprising the acquired RF signal could be used to identify the location of the tissue
boundary layers.

In the acquired ultrasound RF signal, the echo shape is related to the spatial
impulse response of the system. This prior knowledge of the general echo shape
allows for the creation of a signal model that can characterize the ultrasound signal. Assuming the echoes in the received ultrasound RF signal arise from physical
structures at specific depths in the propagation path, the dynamics and characteristics of these structures could be captured within the echoes. Then, the M-mode
sequence can be modelled as a time series of ultrasound RF signals where each signal is represented as a summation of echoes. This time dependency can capture
the dynamics of moving structures, such as the artery wall, and could be used to
extract the corresponding motion quantitatively. **Section 4.1.1** and **Section 4.1.2**
describe the echo model and the RF signal model acquired in M-mode, respectively,
used for artery monitoring in this thesis work.

4.1.1 Gaussian Modulated Sinusoidal Echo

The Gaussian modulated sinusoidal (GMS) echo model has been used as an approximation of the acquired ultrasound echo in several works [78]–[80]. The GMS echo
model can describe the general shape of the ultrasound echo, including its amplitude, depth, frequency, and phase [81]. The GMS echo model for the i-th echo in
the acquired RF signal is defined as:

$$g_i(x; \theta_i) = \beta_i e^{-\frac{4\alpha_i}{c^2}(x-d_i)^2} \cos\left[\frac{4\pi f_{c_i}}{c}(x - d_i) + \phi_i\right]. \tag{4.1}$$

x is the depth along the ultrasound propagation path, c is the speed of sound in the

tissue, and the corresponding parameter vector that characterizes the echo is given

by:

$$\theta_i = \begin{bmatrix} \alpha_i \\ \beta_i \\ d_i \\ f_{c_i} \\ \phi_i \end{bmatrix} \tag{4.2}$$

where α_i is the bandwidth factor, β_i is the magnitude of the echo, d_i corresponds

to the depth location of the reflector from which the echo arises, f_{c_i} is the center

frequency of ultrasound, and ϕ_i is the phase. The bandwidth factor α_i is related to

the bandwidth defined as a FWHM (full width at half maximum), denoted B_i, of

the GMS function as follows:

$$\alpha_i = \frac{B_i^2}{2}. \tag{4.3}$$

Except for $\phi_i \in [-\pi, \pi]$, all the other parameters of the model are assumed to be

positive. The depth location of the reflector that produced an echo is given by the

parameter d_i. The parameters α_i and f_{c_i} describe the frequency characteristic of

the echo. ϕ_i describes the relative phase shift of the carrier wave with respect to the

location of max amplitude of the GMS echo envelope, which corresponds to d_i. Other

echo models exist that incorporate additional parameters to characterize frequency

dispersion and diffuse scattering [82]. Dispersion can cause a frequency downshift
of the ultrasound wave within the received echo (chirping). Additionally, statistics
of the ultrasound RF signal envelope change depending on the scattering density
and structure, and can be characterized using a model known as the Nakagami
distribution [83]. The authors in [82] used a Nakagami envelope shape for the
ultrasound RF echo model, and demonstrated lower residual error compared to the
GMS model when fit to an acquired echo.

In this thesis however, as an approximation, the biological tissue is assumed
to have negligible acoustic dispersion, and the scattering condition is assumed to
be specular for all echoes in the received signal (i.e., there is no chirping in the
acquired echoes, and the echo envelopes may all be adequately described by a Gaus-
sian shape). Thus, the GMS echo model is assumed to adequately represent the
desired echoes in the acquired ultrasound RF signal used for artery monitoring ap-
plications. These assumptions were made to simplify the model for preliminary
experimentation.

4.1.2   Acquired Ultrasound RF signals

Each A-mode ultrasound RF signal acquired in B-mode or M-mode is assumed to
be composed of a superposition of the GMS echoes as expressed in Eq.4.1. It is
assumed that along the depth x, there are a total number of N_x echoes interfering
to produce an ultrasound RF signal received by the UT. The characteristics of the
echoes comprising the received RF signal are assumed to be varying with time, due
to the dynamics of the reflecting media such as artery walls. The time-varying

A-mode ultrasound RF signal acquired as an M-mode sequence is given by:

$$s(x,t) = \sum_{i=1}^{N_x} g_i(x; \theta_i(t)) \tag{4.4}$$

where $\theta_i(t)$ is the time-varying parameter of the echo i, t is the time across successive
A-mode signals in the acquired M-mode, and x is the depth from which the echoes
return to the UT situated at $x = 0$. Variables x and t are assumed to be sampled
at sufficiently high rates such that they may be approximated as continuous. Thus,
$s(x,t)$ is considered as the time evolution of the A-mode ultrasound RF signals.
Assume that the desired artery wall boundary is present at the depth x_d used for
artery monitoring. Of all the echoes in the A-mode signals, an echo i_d at $d_{i_d} = x_d$
would correspond to the echo from the artery wall boundary, and the corresponding
parameter vector will be used for artery monitoring discussed in the **Section 4.4**.

4.2 Matching Pursuit

4.2.1 Review of Signal Decomposition

Expressing an acquired ultrasound RF signal in terms of the comprising echoes is
an ill-posed problem, as a unique solution does not exist. Therefore an approximate
solution method is required for practical implementation. It follows that any solution
method will be suboptimal, and requires certain assumptions to implement.

Deconvolution approaches for estimating the echoes composing an ultrasound
signal [84], [85] assume the exact echo shape of the system is known and stationary
throughout the signal, where each reflector can be modelled as a convolution of an

impulse function with the echo at the appropriate depth. Thus, changes in the echo
characteristics along the signal depth, such as phase changes of the carrier wave and
frequency-dependent attenuation cannot be characterized [77]. Additionally, decon-
volution methods are known to have difficulties resolving closely spaced reflectors
[86], [87]. Improvement has been made to permit the echo shape to change along
the depth [88], [89]. However, the problem of separating closely spaced echoes was
not considered.

Wavelet decomposition [90], another approach to nonstationary signal analysis,
has previously been used for decomposition of the ultrasound signal. In [91], the au-
thors used wavelet decomposition to separate overlapping ultrasound echoes. How-
ever, they noted that the wavelet decomposition has a resolution trade-off that can
affect the accuracy of the result. Additionally, the authors in [92] used wavelet de-
composition as a preprocessing step for B-mode image motion tracking of the artery
walls, but showed that the wavelet decomposition parameters had a significant im-
pact on the accuracy of the motion estimation. Thus, the wavelet decomposition
may not be ideal to accurate characterize the echoes comprising an ultrasound signal
due to the inherent resolution trade-off.

In [93], the authors linearized the cost function for echo parameter estimation
(similar to Eq.4.1) via first-order Taylor expansion, and then derived the expression
for the gradient to use for optimization. The convergence of this method is strongly
dependent on the initial condition set for the gradient descent, and therefore requires
relatively precise prior knowledge of the characteristics and location of specific echoes
in the signal. For decomposition of the ultrasound signals obtained from biological

soft tissue, there may be a high number of echoes that linearly combine to form the acquired signal. Thus, suitable initial conditions may not be known in advance.

4.2.2   Ultrasound RF Signal Decomposition Method Using Matching Pursuit

Matching pursuit (MP) [73], [82], [94] methods of signal decomposition, on the other hand, offer a flexible approach for representing signals in terms of localized structures using a selected basis. MP does not suffer from inherent resolution limitations and does not assume a static echo shape along the depth of the signal. MP greedily decomposes the signal by maximizing the correlation between the estimated echo model and the acquired signal in each iteration. The cost function optimized during each iteration is show in Eq.4.5. After each iteration, the estimated echo is subtracted from the acquired signal and the resulting residual signal is used for the proceeding iteration. The cost function to be optimized is defined by:

$$J(\hat{\theta}) = -\langle R_k, g(x; \hat{\theta}) \rangle \tag{4.5}$$

where J is the loss to be minimized, R_k is the residual in iteration k, $\langle \cdot, \cdot \rangle$ denotes the inner product between two real signals, and $\hat{\theta}$ is the estimated parameter vector in the k-th iteration of MP. The residual for proceeding iterations is updated by subtracting the echo estimate:

$$R_{k+1} = R_k - g(x; \hat{\theta}). \tag{4.6}$$
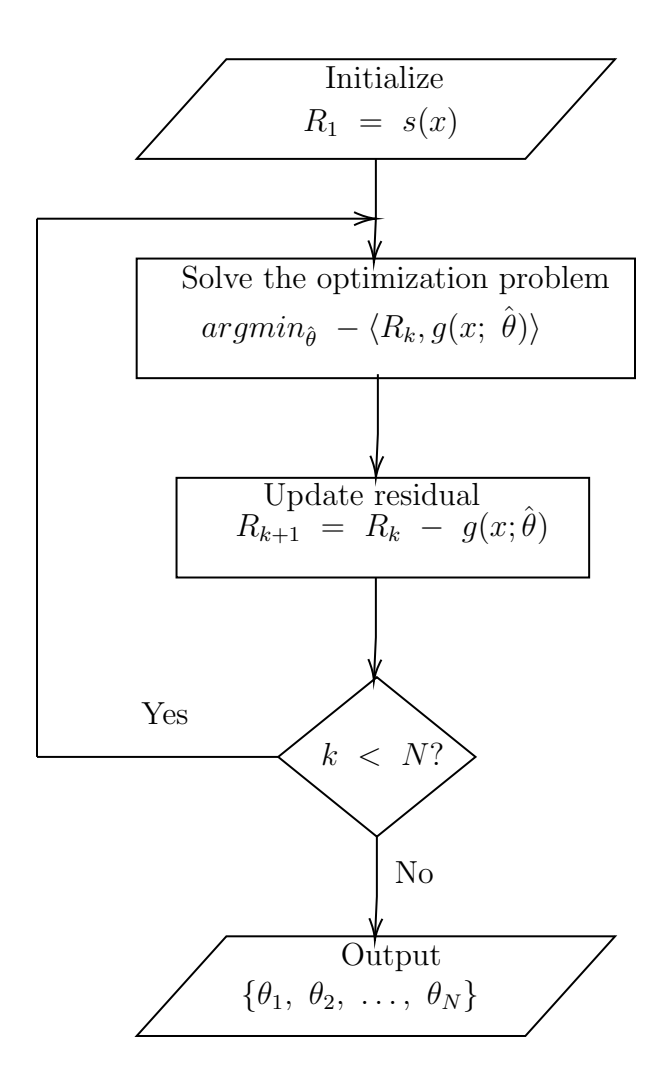
Figure 4.2: *Flowchart of matching pursuit signal decomposition.*

Fig.4.2 shows a flowchart of the MP signal decomposition using the GMS echo

model. An A-mode ultrasound RF signal $s(x)$ is initialized in the first iteration. The

optimization problem is solved to estimate the model parameters, then the residual

is updated for the next iteration. In this work, the iteration number was set as

the stopping criteria. The iteration number N was selected to capture the desired

echoes arising from the artery wall tissues in each RF signal of a particular sequence

used for experimentation. If this number is not known, the residual signal energy

could be used as a stopping criterion. The output is a set of parameter vectors that

describe the echoes composing the input signal.

Maximizing the correlation of the estimated model parameters with the signal
segment is a nonlinear and non-convex optimization problem when using the GMS
basis function. Commonly, a predefined dictionary of candidate functions is used
to evaluate the search space for optimization. This would require sampling the
parameter space appropriately in advance so that the model estimates are optimal
and can be used to resolve the small changes in the parameters containing the
dynamics of the reflectors. Optimization of the cost function in Eq.4.5 requires
an algorithm that can yield optimal model estimates, without requiring the precise
prior knowledge for initialization.

4.3   Particle Swarm Optimization

Swarm intelligence is a class of heuristic algorithms that has been successfully used
in a wide array of nonlinear, non-convex optimization problems [95], [96]. These
algorithms use a population of simple agents that interact locally according to simple
rules in order to efficiently survey the search space for an optimal candidate solution.
Trajectory and velocity information of each agent is updated according to the best
known solution of global and local subsets of the population. Once the population
converges upon a best known candidate solution, the optimization is assumed to
be completed. Since the gradient information is not required, this approach to
optimization is well suited to nonlinear optimization problems; however, convergence
to an optimum is not guaranteed [97]. Recently, swarm intelligence optimization
was used for decomposing ultrasound RF signal using MP without any predefined
dictionary [98].

Of the swarm intelligence optimization algorithms, particle swarm optimization

(PSO) is among the most widely used [99] due to its relatively simple implemen-

tation and acceptable performance [100]. PSO searches for an optimal solution via

a swarm of particles that survey the search space of the cost function. At initial-

ization, a defined number of particles are randomly populated on the search space

used for optimization of the cost function. In each iteration of the optimization, the

particles move toward the best known solution. A further benefit of the optimiza-

tion approach to the signal decomposition is the implicit interpolation that occurs

during the optimization procedure. This can increase the depth location estimates

beyond the sampling resolution of the system, provided the RF signal was suffi-

ciently sampled (above the Nyquist rate). Constrained particle swarm optimization

(PSO) was implemented using MATLAB 2020b (MathWorks, Natick, MA, USA)

Global Optimization Toolbox in this thesis work. For each optimization, a swarm

size of 50 particles was used to ensure consistent convergence to a global solution in

the search space.

$$V_p(h+1) = \omega V_p(h) + c_1 r_1 [pbest(p,h) - P_i(h)] + c_2 r_2 [gbest(h) - P_i(h)], \quad (4.7)$$

$$P_i(h+1) = P_i(h) + V_i(h+1). \quad (4.8)$$

Eq.4.7 and Eq.4.8 show the velocity V and position P update rules for a particle

p during optimization by PSO [99]. ω is a parameter that affects the exploration-

exploitation trade-off, r_1 and r_2 are uniformly distributed random variables, and c_1

and c_2 are coefficients that affect how quickly the particle moves toward the previous
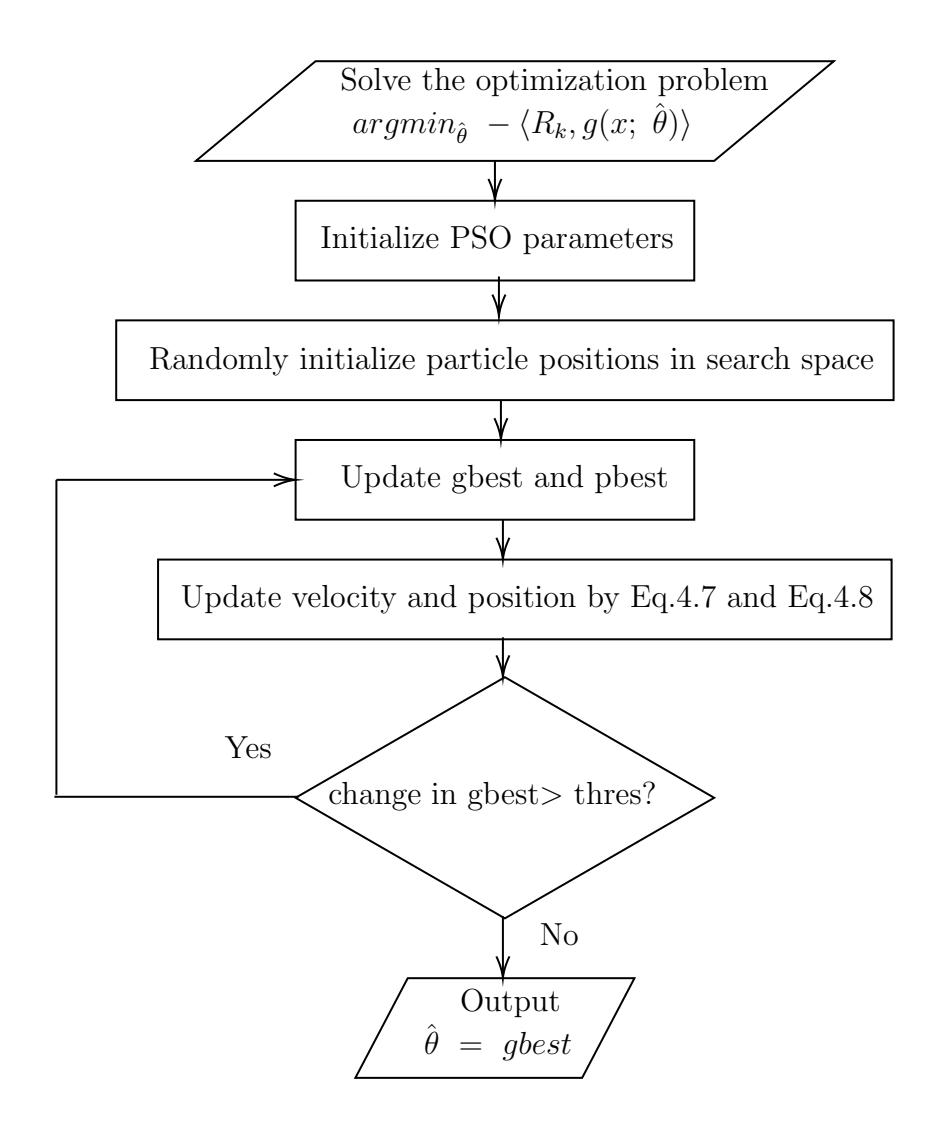
Figure 4.3: *Flowchart of particle swarm optimization.*

or global best known position, respectively. h is the iteration number, and p is the

particle index. The previously best-known position by particle p at iteration h, and

the global best-known position at iteration h is denoted $pbest(p, h)$ and $gbest(h)$,

respectively. If the particle moves out of the imposed constraints, its position is set

to the constraint bound, and its velocity is set to zero.

Fig.4.3 shows a flowchart of the PSO algorithm for optimization of the model

estimate. The position of the particles particles are randomly initialized on the

search space. Each particle evaluates the cost function J at its location, and *gbest*

and *pbest* are updated. Then the velocity and position of each particle are updated
by Eq.4.7 and Eq.4.8, respectively. When the change of the global best-known
solution across an iteration is below a threshold the optimization is assumed to be
completed. The output is the parameter estimate $\hat{\theta}$ of the GMS echo model for the
signal R_k.

Retaining physical interpretation of the echo model estimate and inherent limita-
tions of the motion tracking approach required constraints to be imposed during the
optimization to yield suitable echo estimates. Specifically, the center frequency pa-
rameter of an echo is assumed to be constant. This is required for the phase-based
motion tracking discussed in the proceeding section. Additionally, the estimated
echoes in a signal segment are assumed to have the same bandwidth. This constraint
was required due to the tendency of the cost function (Eq.4.5) to optimize for global
signal structures [101]. Thus, when the bandwidth parameter is unconstrained, the
optimization may converge to an echo estimate that has a wider pulse-width than
the physical echoes produced by the ultrasound system. This removes the physical
interpretation of the echo estimates comprising an ultrasound RF signal.

4.4   Artery Monitoring Methods

The parameters for artery monitoring, such as the displacement of the artery walls
and the IMT, can be estimated using the echoes of interest which were isolated and
identified by using the ultrasound RF signal model described in **Section 4.1** and
by the decomposition method in **Section 4.2** and **Section 4.3**. IMT estimation is
performed using the depth location parameters of the echoes corresponding to the

artery wall layer boundaries (i.e., lumen-intima and media-adventitia boundaries).
The artery wall motion tracking is implemented by a phase-based method using
the phase and depth location parameter of the artery wall echo obtained from each
RF signal in an M-mode sequence. **Section 4.4.1** and **Section 4.4.2** explain the
methods of the IMT estimation and the artery wall motion tracking, respectively,
using the parameters of the decomposed echoes.

4.4.1   Intima-Media Thickness Estimation

Separation of overlapping echoes is a problem that is studied in ultrasound non-
destructive evaluation and biomedical applications. MP methods of decomposition
have received attention in ultrasound nondestructive evaluation [82], [102], [103], and
demonstrated success despite drawbacks in the MP algorithm such as the greedy
selection resulting in suboptimal echo estimates and the tendency to converge to
global signal structures. IMT estimation requires the depth location of the echoes
from the lumen-intima and media-adventitia boundaries of the artery wall. These
echoes may be overlapped if the depth spatial resolution of the ultrasound system
is lower than the IMT to be estimated. IMT estimation was performed in this work
by calculating the difference of the depth location parameters corresponding to the
lumen-intima and media-adventitia wall boundaries obtained after decomposition of
each RF signal. The estimated IMT, denoted δ, is calculated as follows:

$$\delta(t) = |d_{LI}(t) - d_{MA}(t)| \tag{4.9}$$

where d_{LI} and d_{MA} corresponds to the depth location estimate of the lumen-intima

and media-adventitia boundaries, respectively. The average change in the IMT during the cardiac cycle could be approximately 0.041 mm [104]. The clinical system used for *in-vivo* experiments with the proposed method had a depth sampling interval of 0.023 mm. Since the approximate variation of the IMT during the cardiac cycle is proportional to the depth sampling interval of the clinical system, it was not assumed that these details could be observed and therefore the IMT is assumed to be constant during the cardiac cycle for the *in-vivo* experiments.

4.4.2   Artery Wall Motion Tracking

Let n be the M-mode frame number (i.e., A-mode signal index), and T be the M-mode frame acquisition interval, where the sampling of the parameter vector $\theta(t)$ of a chosen echo with the index n is denoted $\theta[n] \triangleq \theta(nT)$. Assuming the center frequency of the chosen artery wall boundary echo is a constant during the M-mode acquisition, the speed of sound is a constant (c), the displacement $\Delta[n]$, (i.e., depth variation of the echo across two successive A-mode signals), can be written as follows:

$$\Delta[n] = d[1] - \frac{c}{4\pi f_c}\phi[1] + \frac{c}{4\pi f_c}\sum_{k=2}^{n}(\angle A_k) \qquad (4.10)$$

Once the ultrasound RF signals acquired in M-mode are decomposed into their constituent echoes using the proposed signal model and decomposition method, the motion of the artery wall boundary echoes can be tracked using Eq.4.10. The relative displacement ($\angle A_k$) of the isolated echo is calculated across each M-mode frame in the sequence by reconstructing the carrier waves using the estimated parameters and performing cross-correlation. The relative displacements are accumulated across the

M-mode to obtain the displacement variation (containing the motion) across the
recording. The initial depth is set to be the phase-adjusted depth location estimate
of the isolated echo in the first M-mode frame of the sequence.

In theory, the phase of an echo should not change unless the viscosity of the
propagation media changes during the M-mode acquisition [105]. However, incor-
porating the phase parameter was found to improve the estimation accuracy in the
experiments. The phase parameter may compensate for errors in the depth location
estimate that arise when interference changes the envelope shape in successive A-
modes. It can be shown in Eq.4.10 that when the phase parameter does not change
across frames, the motion is estimated by tracking the changes in the depth location
parameter.

Chapter 5

Experimental Results

In this chapter, the experimental results using the signal decomposition methodology that was proposed in **Chapter 4** for IMT estimation and motion tracking are presented. All experiments were implemented using MATLAB 2020b (MathWorks, Natick, MA, USA). Discussion of the limitations and strengths indicated by the experimental results are given in each section.

Section 5.1 shows the results of the numerical simulation experiments that were conducted to evaluate the proposed methodology for IMT estimation and artery wall motion tracking. Simulated ultrasound RF signals based on the GMS echo model were created using realistic parameters of ultrasound systems and arteries. The accuracy of the estimated depths for the lumen-intima and media-adventitia boundaries and the corresponding IMT estimations were evaluated with varied IMT and ultrasound frequencies.

Section 5.2 presents the results of *in-vivo* experiments conducted to evaluate the proposed methodology for IMT estimation and motion tracking. IMT estima-

tion is performed using M-mode and B-mode data that was obtained from the far wall of the carotid artery by the clinical ultrasound imaging system. The mean and standard deviation of the estimated IMTs are presented and discussed. IMT estimates obtained by the proposed method are compared with the estimates obtained by manual estimation using an established clinical method [36]. Motion tracking of the artery walls is performed using M-mode data that was obtained by the WUS system. The decomposition and motion tracking results of the carotid artery walls obtained by the proposed method are shown. The diameter changes over the cardiac cycle as estimated by the proposed method is shown. Comparison to the motion tracking results obtained by CC is also presented.

5.1   Numerical Simulation Experiment in IMT Estimation

Numerical simulation experiments are valuable for evaluation of ultrasound DSP algorithms due to the lack of known ground truths for the physiological parameters when using *in-vivo* data [106]. A numerical simulation experiment was conducted to evaluate the feasibility of the proposed method for IMT estimation when the tissue boundary echoes are overlapped. This kind of echo overlap can be considered as a correlated noise when seeking to resolve the locations of the reflectors. White noise was not considered in this work, as it was assumed to be of less importance. However, since the cost function Eq.4.5 is based on a correlation measure, the proposed method would exhibit a strong robustness to uncorrelated white noise. Ultrasound

RF signals were generated using the GMS echo model expressed in Eq.4.1. Simulation experiments for the IMT estimation are given in **Section 5.1.1**. Numerical simulation of the motion tracking simulation is not presented as the simulation of realistic dynamic echoes is an ongoing area of research and requires more sophisticated simulation models that are discussed in **Section 6.2**.

The amplitude of each echo was randomly selected within the given constraint from a Gaussian or normal distribution, $\mathcal{N}(\mu, \sigma)$ with mean μ and standard deviation σ to simulate the random fluctuation of echo amplitudes observed *in-vivo*. The standard deviation of the echo amplitudes was selected based on empirical observation of the echo amplitude fluctuations in A-mode *in-vivo* signals. Phase of each echo was assumed to be a uniformly randomly distributed variable and is denoted by $\mathcal{U}(u_1, u_2)$ in this thesis. $\mathcal{U}(u_1, u_2)$ denotes the parameter selection from the uniform distribution over the range $[u_1, u_2]$.

5.1.1   IMT Estimation

In this subsection, the depth estimation accuracy of the tissue boundary layers used for IMT estimation is evaluated. Of particular interest are conditions when the axial resolution of the ultrasound results in a partial overlap of the two echoes of interest. The simulated RF signal contains two echoes (i.e., the lumen-intima and media-adventitia boundary echoes of the artery wall). The first simulation experiment examines the estimation accuracy of the boundary layer depths and IMT for varying IMT values in **Section 5.1.1.1**, with ultrasound system parameters representative of the clinical ultrasound imaging system used in the *in-vivo* experiment presented

in the **Section 5.2**. The second simulation experiment evaluates the estimation

accuracy with respect to the ultrasound frequency and bandwidth for a fixed IMT

value in **Section 5.1.1.2**.

5.1.1.1   Effect of IMT Value on IMT Estimation Accuracy

Table 5.1: *Parameters of two echo model used to simulate the RF signal for evaluating the effect of IMT values on the IMT estimation accuracy.*

Parameter	Echo 1	Echo 2
$\alpha \ (MHz)^2$	18	18
$\beta \ (a.u.)$	$\mathcal{N}(1, 0.1)$	$\mathcal{N}(1, 0.1)$
$d \ (mm)$	d_1	$d_2 = d_1 + \delta$
$f_c \ (MHz)$	6	6
$\phi \ (rad)$	$\mathcal{U}(-\pi, \pi)$	$\mathcal{U}(-\pi, \pi)$

Table.5.1 presents the simulation model parameters that were used for evaluation

of the IMT estimation accuracy. The simulated RF signal was constructed using

the center frequency ($f_c = 6$ MHz), -6 dB bandwidth ($\alpha = \frac{6^2}{2}$ MHz^2), and depth

sampling interval (23 μm) corresponding to the estimated spectral characteristics of

the far wall signal segments obtained by the clinical ultrasound imaging system used

in the *in-vivo* experiment. A 5 mm signal segment was used to reflect the conditions

of the *in-vivo* experiment. The absolute depth values of the simulation model are

arbitrary and were therefore not selected to correspond to realistic depths of the

artery walls. The IMT value was varied from 0.1 to 0.8 mm with a step 0.1 mm.
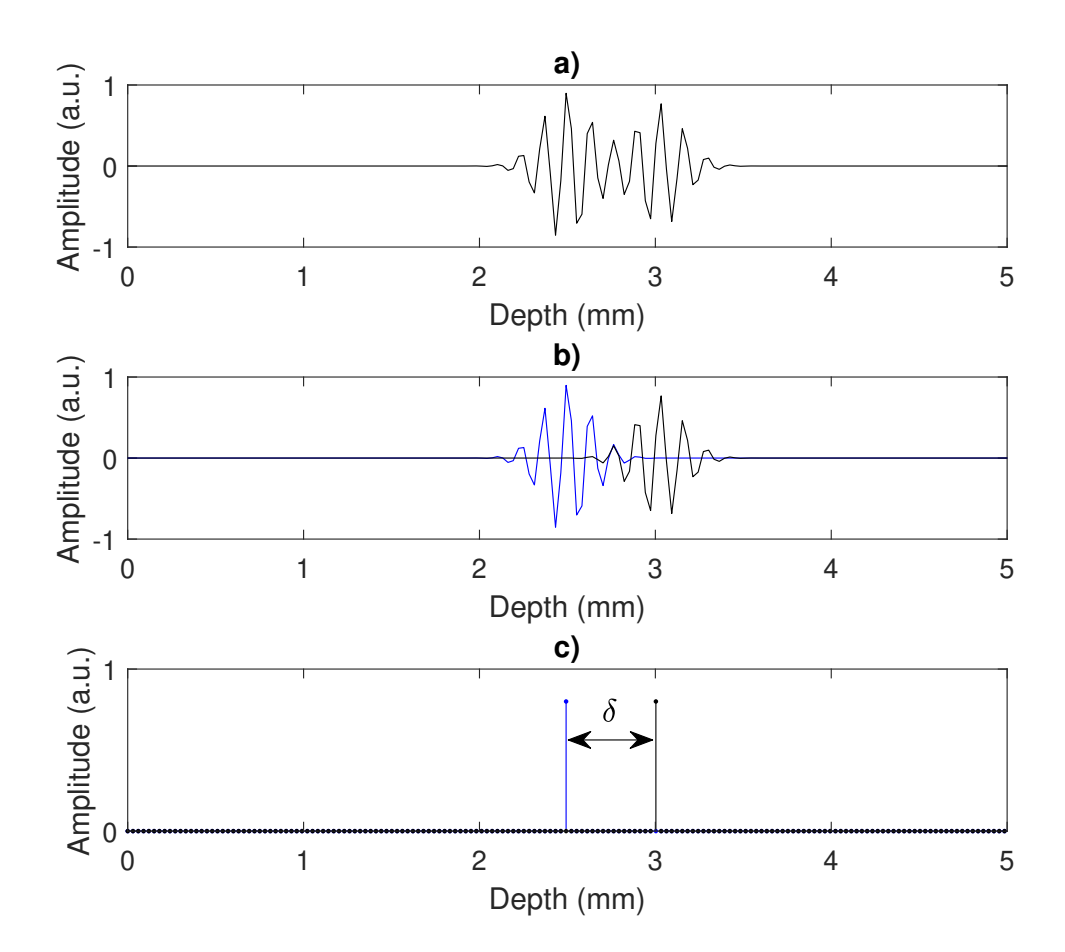
Figure 5.1: *a) Example simulated RF signal for IMT experiment. b) Echoes composing the signal, blue and black are Echo 1 and Echo 2, respectively. c) Illustration showing d_1 (blue), d_2 (black) and δ of the simulated RF signal.*

The variation in IMT values covers the typical range of a human subject (from 0.4 to 0.8 mm) [107].

Fig.5.1 a) shows an example RF signal used for the experiment, b) shows the GMS echoes used to construct the signal, and c) illustrates $d_1 = 2.5$ mm (blue), $d_2 = 3$ mm (black), and $\delta = 0.5$ mm of the simulated signal.

The proposed decomposition method was applied to the simulated RF signals. Table.5.2 presents the search space constraints used for the decomposition of the

Table 5.2: *Search space constraints used to evaluate the effect of IMT values on the IMT estimation accuracy.*

Parameter	Constraint
$\alpha \ (MHz)^2$	18
$\beta \ (a.u.)$	> 0
$d \ (mm)$	depth range of signal segment
$f_c \ (MHz)$	6
$\phi \ (rad)$	$[-\pi, \pi]$

simulated RF signals. The resulting absolute errors of the location estimates and IMT were computed. The experiment was performed 200 times for each IMT value, with the parameters of the echoes generated according to Table.5.1, where δ is the IMT, d_1 is the depth of the Echo 1, and d_2 is the depth of Echo 2. The phase and amplitude were randomly sampled from the corresponding distributions given in Table.5.1 to simulate the random interference of the echoes. The simulated RF signals were decomposed into two echoes by the proposed method, to estimate d_1, d_2 and δ. The search space was constrained for each parameter used to simulate the RF signal, as shown in Table.5.2. The estimated IMT was calculated using Eq.4.9 using the d_1 and d_2, and the IMT estimation error was obtained with respect to the IMT values.

Fig.5.2 summarizes the results of the simulation experiment for depth location estimation. The blue and orange boxes correspond to the location estimates the echo decomposed in iteration 1 and 2 of the algorithm, respectively.
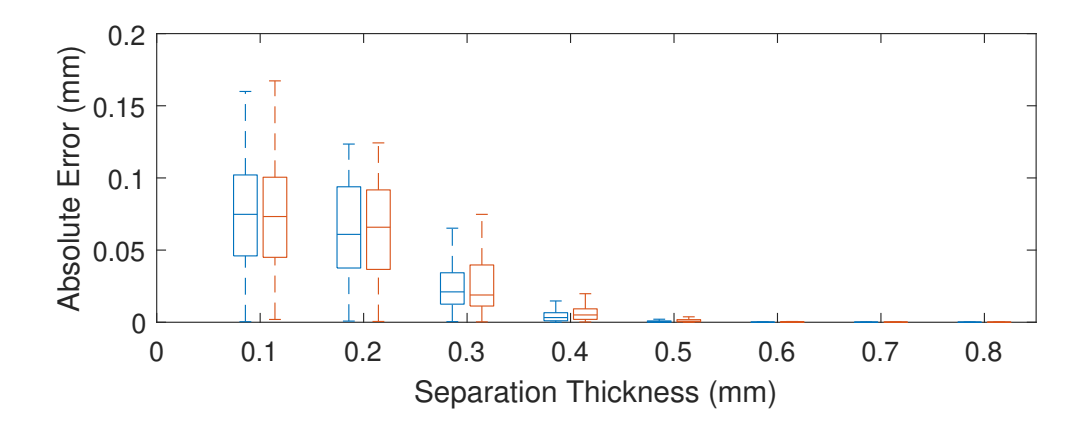
Figure 5.2: *Boxplot of the absolute error in depth estimates with respect to the IMT values. The estimate from iteration 1 is indicated in blue, and iteration 2 in orange.*
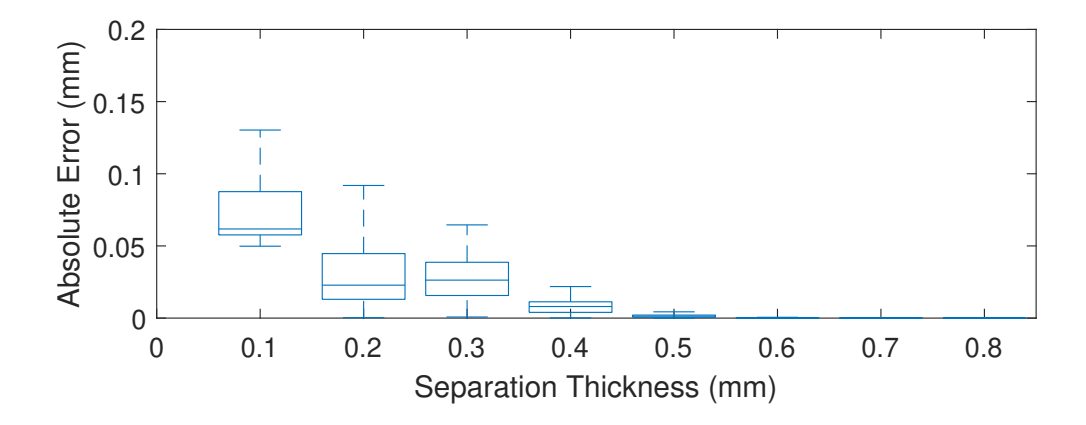
Figure 5.3: *Boxplot of the absolute error of IMT estimates against the IMT.*

Fig.5.3 shows the corresponding boxplot of the absolute errors of the IMT estimates. For realistic IMT values $(0.4 - 0.8$ mm$)$ [108] the error is less than 0.025 mm under the simulation conditions used for experimentation. It is observed that the depth estimation errors increase with smaller IMT values and the corresponding increased overlap of the echoes. This is caused by the greedy strategy that optimizes the model estimate to the global signal structure in each iteration.

5.1.1.2   Effect of Ultrasound Frequency on IMT Estimation Accuracy

Higher frequency and wider bandwidth of the pulsed ultrasound results in greater axial resolution that helps to identify the echoes corresponding to closely space tissue interfaces. However, in biological tissues, the attenuation of the ultrasound wave increases in proportion to the ultrasonic frequency [74]. When the artery of interest is located in a deeper tissue area, the two echoes needed to estimate the IMT may not be separated enough, and may significantly overlap one another due to the chosen ultrasonic frequency. Thus, the effect of the ultrasonic frequency and bandwidth on the IMT estimation accuracy will influence the estimation accuracy and is therefore investigated in this section.

To examine the effect of lowered spatial resolution on the ability to accurately estimate the IMT using the proposed method, an additional numerical simulation experiment was performed. The IMT was set to 0.5 mm, and the ultrasound frequency was varied from 1 MHz to 8 MHz with a step of 1 MHz. The bandwidth of the pulse was selected to be equal to the center frequency in each case.

Fig.5.4 a) shows an example simulated RF signal for an ultrasound frequency of 4 MHz, b) shows the GMS echoes used to construct the signal, and c) illustrates $d_1 = 2.5$ mm (blue), $d_2 = 3$ mm (black), and $\delta = 0.5$ mm of the simulated signal.

The experiment was performed 200 times for each frequency (denoted f_c in the table), with the parameters of the echoes generated according to Table.5.3. The search constraints used for the decomposition is shown in Table.5.4.

Fig.5.5 shows a boxplot of the absolute errors of the depth estimates for varying ultrasound pulse frequencies. The blue and orange boxes correspond to the echo
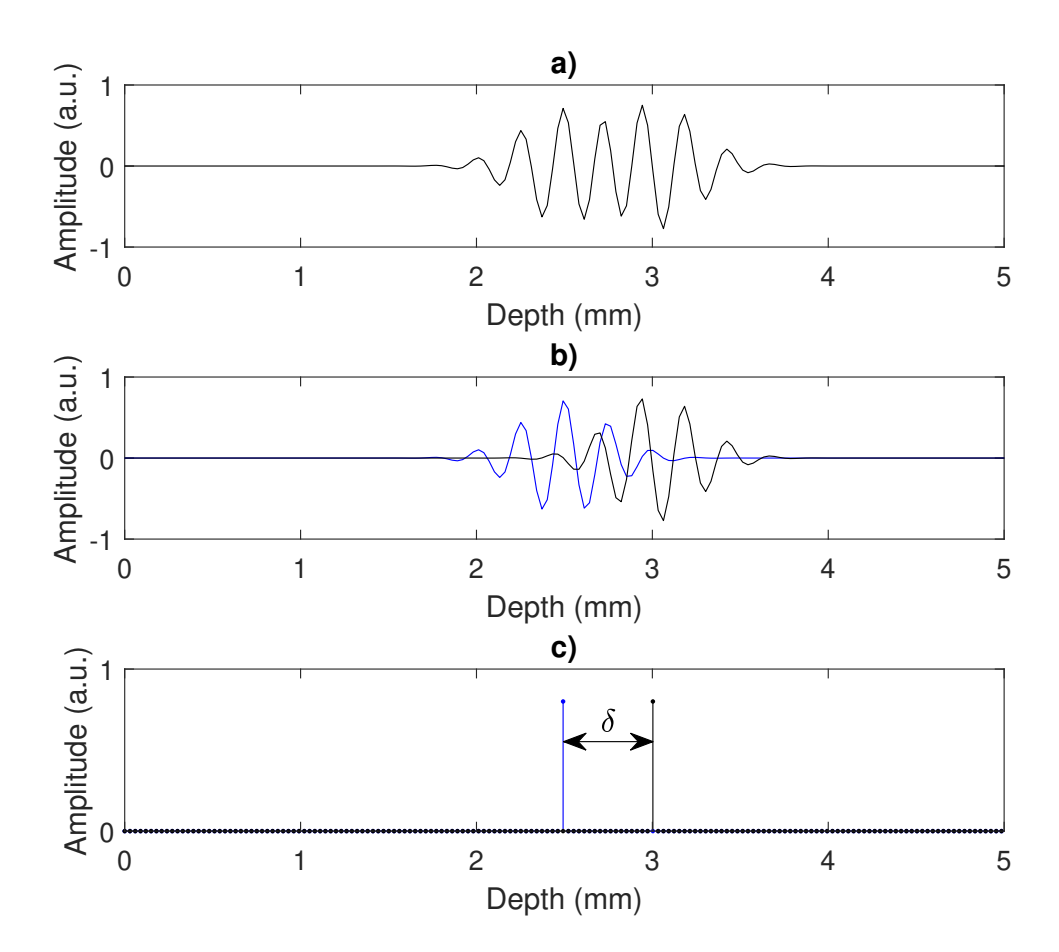
Figure 5.4: *a) Example simulated RF signal for ultrasound frequency experiment.*

b) Echoes composing the signal, blue and black are Echo 1 and Echo 2, respectively.

c) Illustration showing d_1 (blue), d_2 (black) and δ of the simulated RF signal.

estimate obtained in the first and second iteration of the decomposition algorithm,

respectively. Higher errors are observed in the echo estimates obtained in the second

iteration. This is caused by the greedy method propagating errors to proceeding

iterations of the decomposition. When an error is made in a earlier iteration of the

decomposition, signal artifacts are introduced that may change the echo estimation

of proceeding iterations.

Fig.5.6 shows a boxplot of the absolute errors of IMT estimates for varying ul-

Table 5.3: *Parameters of two echo model used to evaluate the effect of ultrasound frequency on IMT estimation accuracy.*

Parameter	Echo 1	Echo 2
$\alpha\ (MHz)^2$	$\frac{f_c^2}{2}$	$\frac{f_c^2}{2}$
$\beta\ (a.u.)$	$\mathcal{N}(1, 0.1)$	$\mathcal{N}(1, 0.1)$
$d\ (mm)$	d_1	$d_1 + 0.5$
$f_c\ (MHz)$	f_c	f_c
$\phi\ (rad)$	$\mathcal{U}(-\pi, \pi)$	$\mathcal{U}(-\pi, \pi)$

Table 5.4: *Search space constraints used to evaluate the effect of ultrasound frequency on IMT estimation accuracy.*

Parameter	Constraint
$\alpha\ (MHz)^2$	$\frac{f_c^2}{2}$
$\beta\ (a.u.)$	> 0
$d\ (mm)$	depth range of signal segment
$f_c\ (MHz)$	f_c
$\phi\ (rad)$	$[-\pi, \pi]$

trasound pulse frequencies. The upper limit of errors in the IMT estimates for 5 MHz is 20%. Thus, the IMT estimation accuracy is better than 80% when the ultrasonic frequency is greater than 5 MHz under the simulation experimental conditions employed.

While the numerical simulation results using the proposed method indicate the
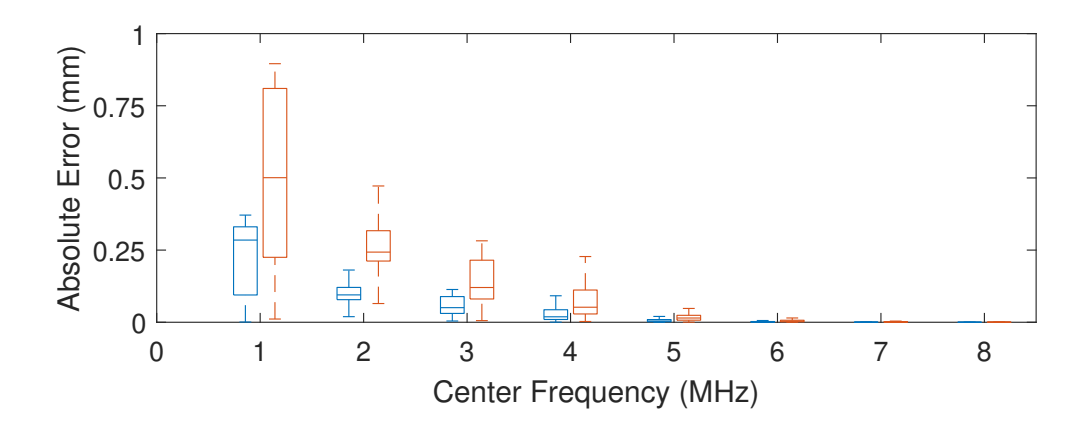
Figure 5.5: *Boxplot of the absolute error in depth estimates against the ultrasound pulse frequency. The estimate from iteration 1 is indicated in blue, and iteration 2 in orange.*
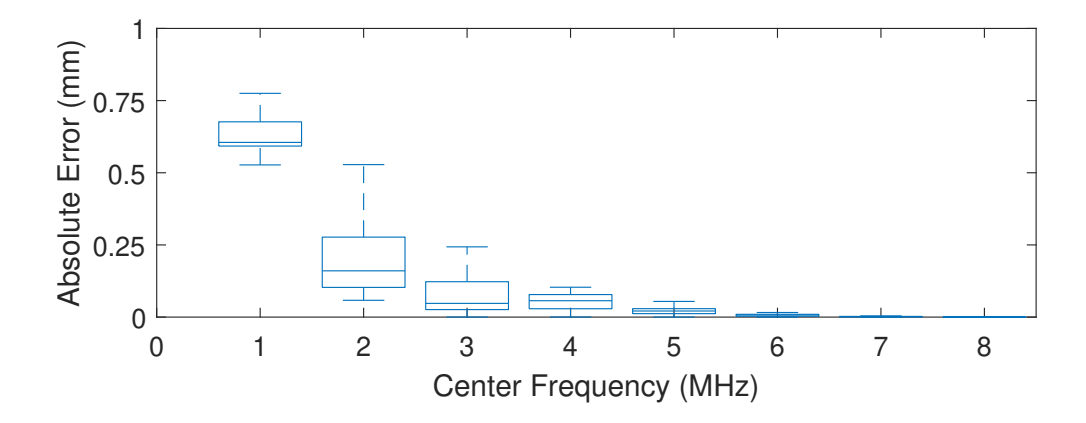
Figure 5.6: *Boxplot of the absolute error in IMT estimates against the ultrasound pulse frequency.*

potential for IMT estimation when there is partial overlap of the echoes, the simplistic simulation model did not account for the random interference of additional scattering echoes that would introduce errors in the decomposition process.

5.2 *In-vivo* Experiments

In-vivo experiments were performed to evaluate the proposed method. Due to COVID-19 restrictions, the ultrasound data used in the *in-vivo* experiments were from existing data that were previously acquired in the biomedical engineering lab at Carleton University [29]. The data were acquired from the CCA of a healthy human subject. IMT estimation was evaluated using data obtained by the clinical ultrasound imaging system, and the artery wall motion tracking was evaluated using data obtained by the WUS system. The details of the ultrasound system used for both experiments were given in the **Section 2.3**. The proposed decomposition method was compared to a reference technique for IMT estimation and motion tracking of the artery walls.

5.2.1 IMT Estimation Using Clinical Ultrasound Imaging System

5.2.1.1 Ultrasound Dataset and Results

A clinical ultrasound system with a linear array probe was used for data acquisition. The frame rate used was 30 Hz, and the spatial sampling frequency was 33.3 MHz. The center frequency and bandwidth were estimated from the far wall signal segments and used to place the constraints of the search space. Each RF signal was interpolated by a factor of 10. A 5 mm window in depth was manually placed around the echoes corresponding to the far wall of the carotid artery.

Table.5.5 shows the constraints used for the ultrasound RF signal decomposition.

Table 5.5: *Search space constraints for IMT estimation using clinical system.*

Parameter	Constraint
$\alpha\ (MHz)^2$	$18\ (\text{MHz})^2$
$\beta\ (a.u.)$	> 0
$d\ (mm)$	depth range of signal segment
$f_c\ (MHz)$	6 MHz
$\phi\ (rad)$	$[-\pi, \pi]$

Three echoes were estimated ($N = 3$ in Fig.4.2) in each signal based on prior knowledge of the dominant echoes arising from the tissue boundaries of the artery wall [72].

Fig.5.7 shows an example signal segment and the resulting decomposition. The decomposition result contains echo estimations corresponding to the echogenic tissue layer boundaries of the artery wall. The IMT estimation is obtained from the location estimates of the lumen-intima echo (blue) and media-adventitia echo (black). The red GMS echo indicated in Fig.5.7 may correspond to the adventitia-tissue boundary.

Fig.5.8 shows an M-mode image at a chosen UT location used for IMT estimation. The UT was selected based on having a detectable lumen-intima boundary echo (the echogenicity of this boundary is low and was not captured by each UT), and the IMT was estimated using each A-mode RF signal in an M-mode sequence obtained by that UT. The red lines correspond to the location estimation of the lumen-intima and media-adventitia boundaries of the artery wall layers, at approximately 22 mm
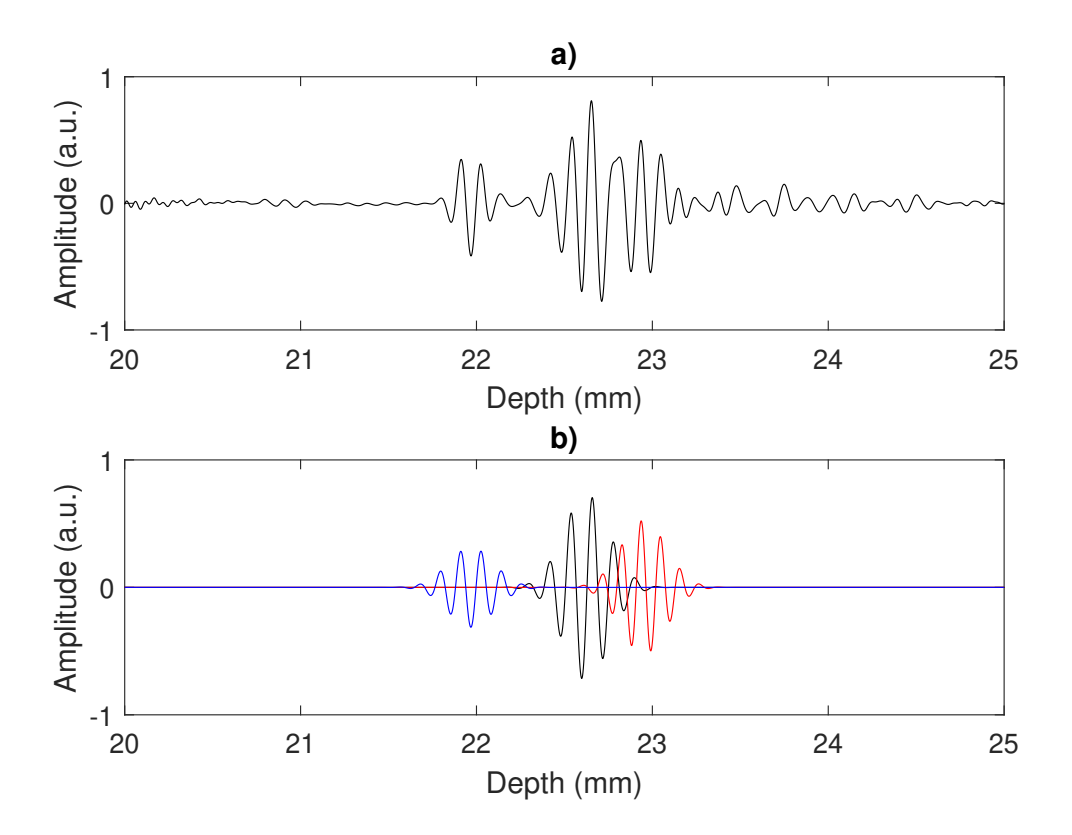
Figure 5.7: *a) Far wall segment of carotid artery obtained using clinical system. b) Decomposition result. Blue corresponds to the lumen-intima boundary echo, black corresponds to the media-adventitia boundary echo used for the IMT estimation and red corresponds to the adventitia-tissue boundary echo.*

22.7 mm, respectively.

The resulting distribution of IMT estimations obtained from the M-mode sequence is shown in Fig.5.9. The mean and standard deviation (SD) of the IMT estimation were 0.67 mm and 0.032 mm, respectively. The mean and SD IMT estimation obtained are within reference values reported in the literature [109].

The IMT was estimated using the RF signals obtained by adjacent UTs within a range of 8 mm along the longitudinal direction of the artery where the lumen-intima boundaries were well-defined. Fig.5.10 shows the estimated lumen-intima
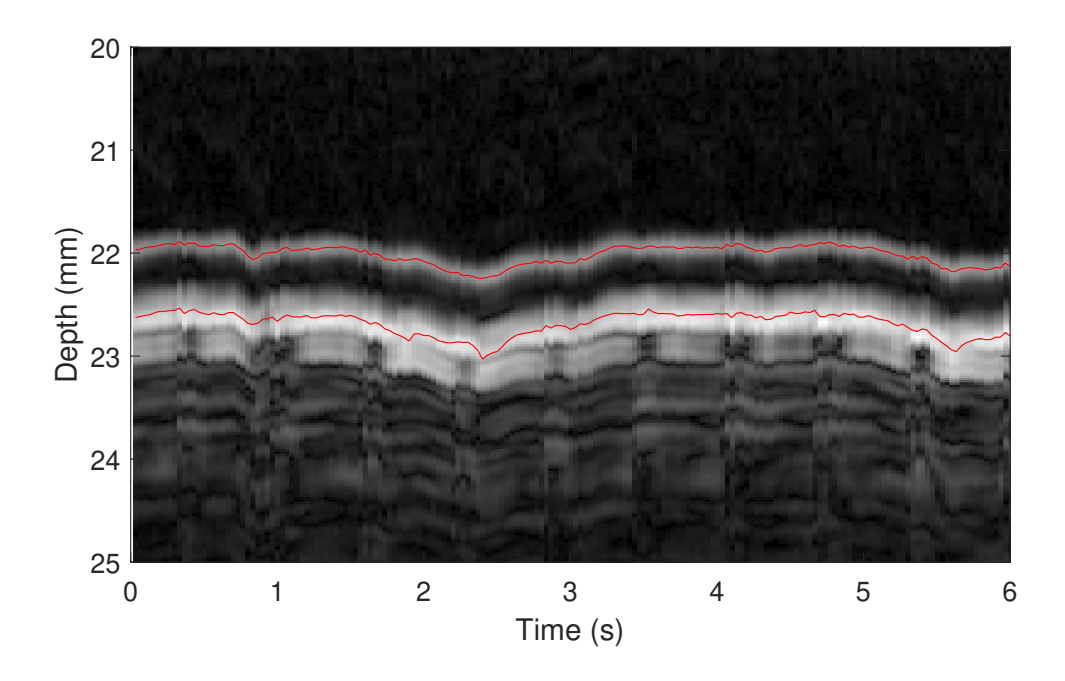
Figure 5.8: *M-mode image of far wall segment overlaid with the estimated lumen-intima and media-adventitia boundaries (shown in red).*
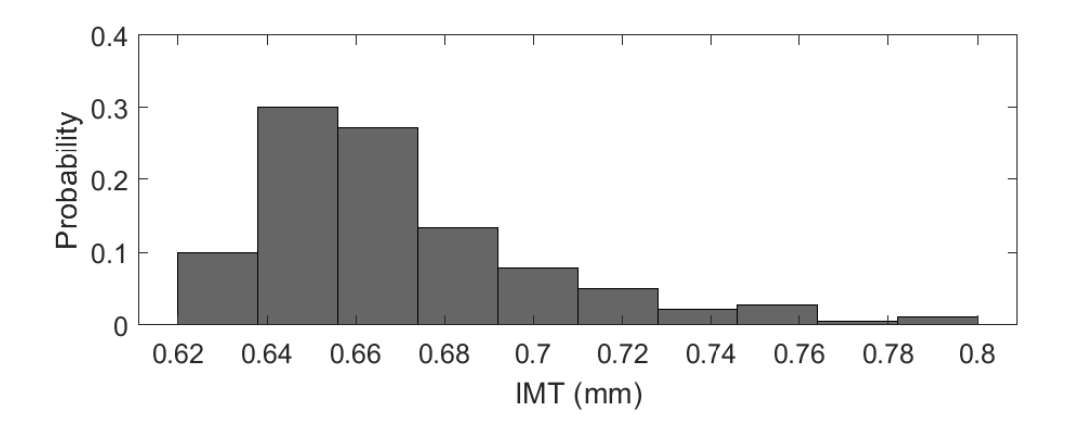
Figure 5.9: *Distribution of estimated IMT values using signal decomposition of RF signals at a chosen UT location in M-mode.*

and media-adventitia boundaries overlaid (red lines) on the corresponding B-mode image segment of the far wall of the carotid artery. Areas where the lumen-intima echo is faint were not captured by the decomposition and resulted in an error.

The distribution of IMT estimates obtained from the corresponding RF signals
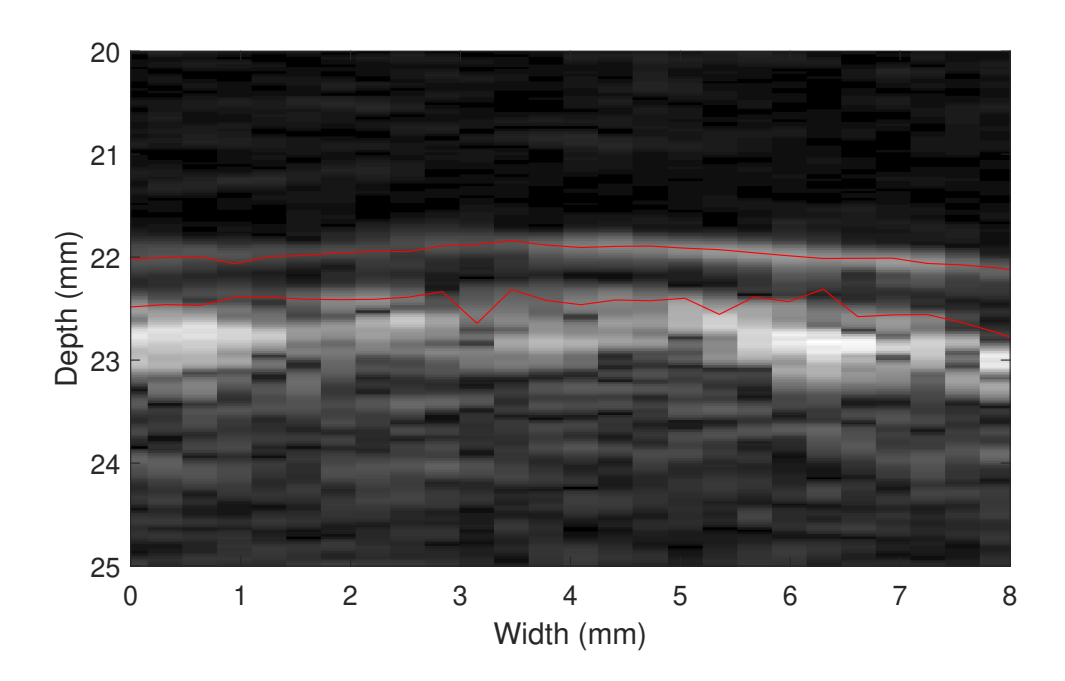
Figure 5.10: *Lumen-intima and media-adventitia boundaries (red lines) estimated by the proposed decomposition method, overlaid on B-mode image of longitudinal region used for estimation.*
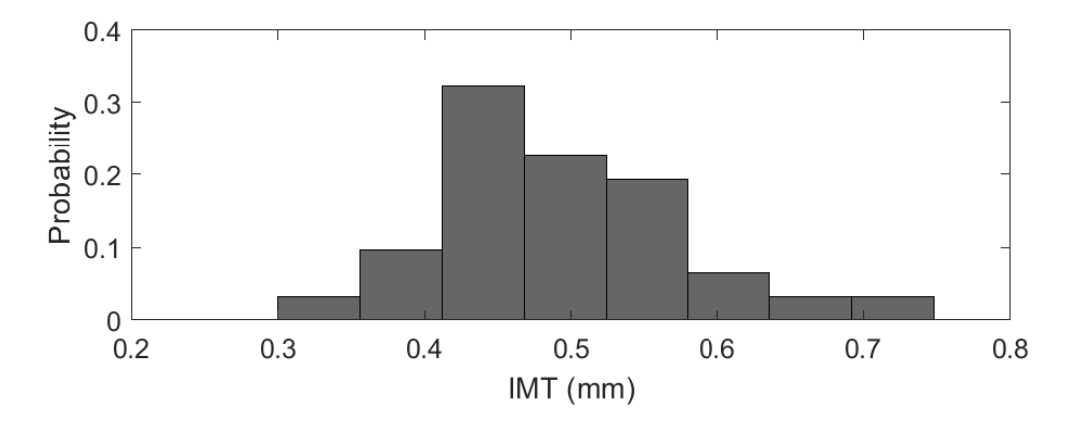
Figure 5.11: *Distribution of estimated IMT values using signal decomposition of RF signals in longitudinal region.*

is shown in Fig.5.11. The mean and SD of the estimates were 0.49 mm and 0.087 mm, respectively. The IMT estimation results using the longitudinal RF signal data resulted in a lower mean and higher SD than those using the M-mode data shown in

Fig.5.9. This may capture the variation of the IMT along the longitudinal direction of the artery in the range of 8 mm. However, underestimation of the IMT also may occur when the faint wall boundary echoes are not captured by the decomposition.

The greedy strategy of the MP method decomposes the echoes of a given signal in descending order of magnitudes. Thus, when the desired boundary echoes are relatively low magnitude compared to other echoes in the signal segment, they may not be captured for a given number of iterations. Increasing the number of estimated echoes does not result in a straightforward solution to this problem. As discussed in the numerical simulation experiment **Section 5.1.1**, artifacts could be introduced when the number of iterations is increased. This can diminish the physical meaning of the echo estimates, and result in errors.

For this preliminary experimentation of the decomposition approach from estimating the IMT, the two estimated echoes with the shallowest depth were assumed to be the lumen-intima and media-adventitia boundary echoes. Automatic identification by identifying the correct boundary echoes within the set of decomposed echoes may avoid the problem of underestimation. The iteration number of the decomposition could then be set based on the residual signal energy to ensure the faint echoes are captured. Automatic identification of the desired echoes is nontrivial and is a future study topic, as discussed in **Section 6.2.1**.

5.2.1.2 Comparison to Manual Estimation

The IMT estimates obtained by the proposed method using the M-mode data (results shown in Fig.5.9) were compared with manual labelling using a clinical method [36]. The manual labelling was performed by the author using reference clinical
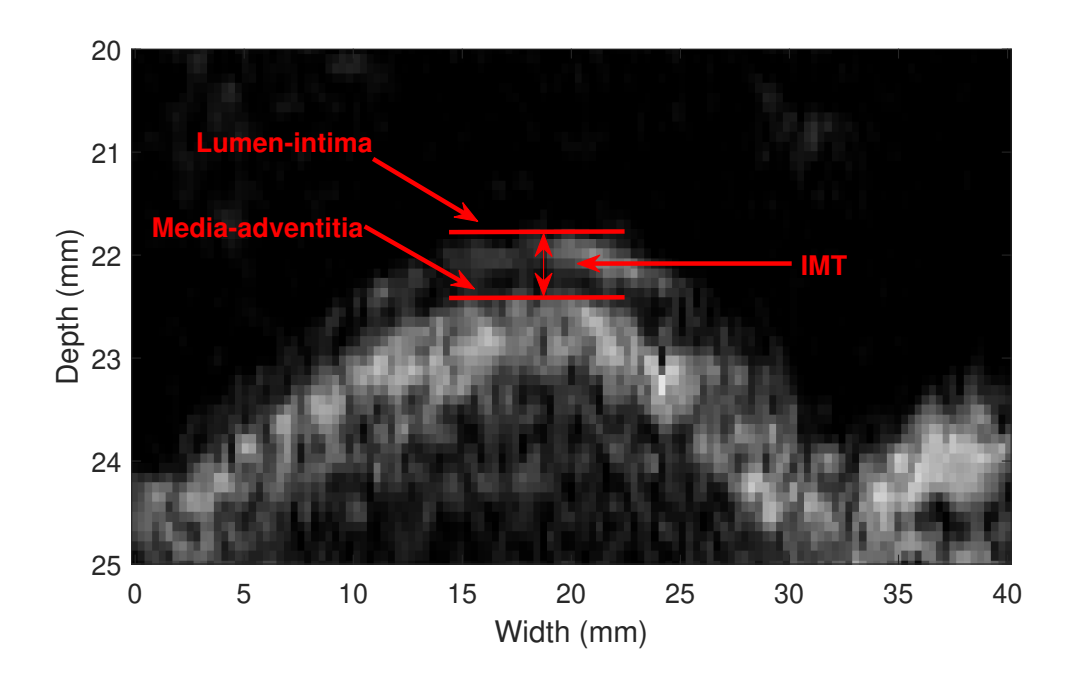
Figure 5.12: *Diagram of the leading edge method of IMT estimation using the B-mode image segment of the far wall of the carotid artery.*

literature. The leading edges (see **Section 3.1**) of the lumen-intima and media-adventitia boundary echoes were manually identified using the B-mode images of the far wall.

A diagram of the manual labelling is shown in Fig.5.12. The B-mode frame-rate was downsampled from 30 Hz to 10 Hz, and the IMT was manually estimated in the 8 mm longitudinal region used previously for each image in the 6 second recording (60 samples).

Fig.5.13 shows the resulting distribution of manual IMT estimates. The mean and SD of the resulting IMT estimates were 0.69 mm and 0.05 mm, respectively.

The manual estimates and those obtained by the proposed method were compared using Bland-Altman analysis [110], as shown in Fig.5.14. Bland-Altman analysis is used to compare two methods of measurement when the true values are un-
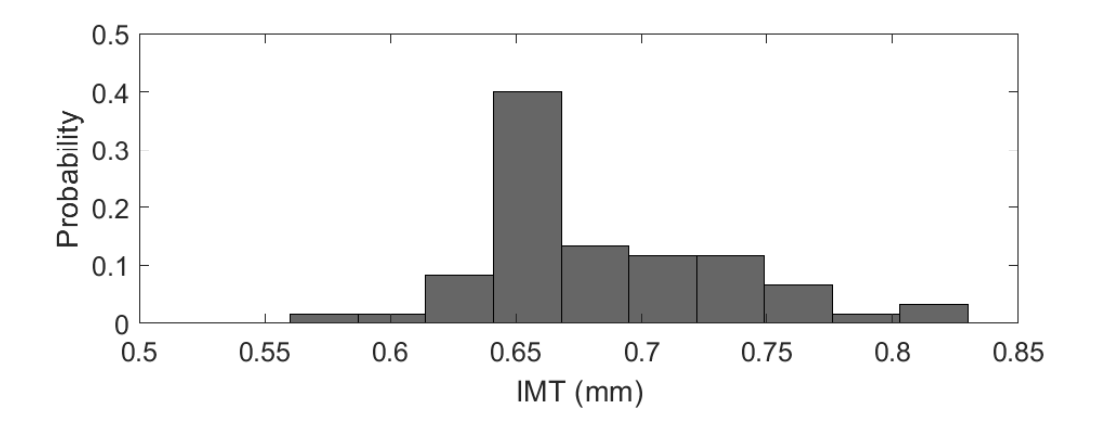
Figure 5.13: *Distribution of manual IMT estimates.*
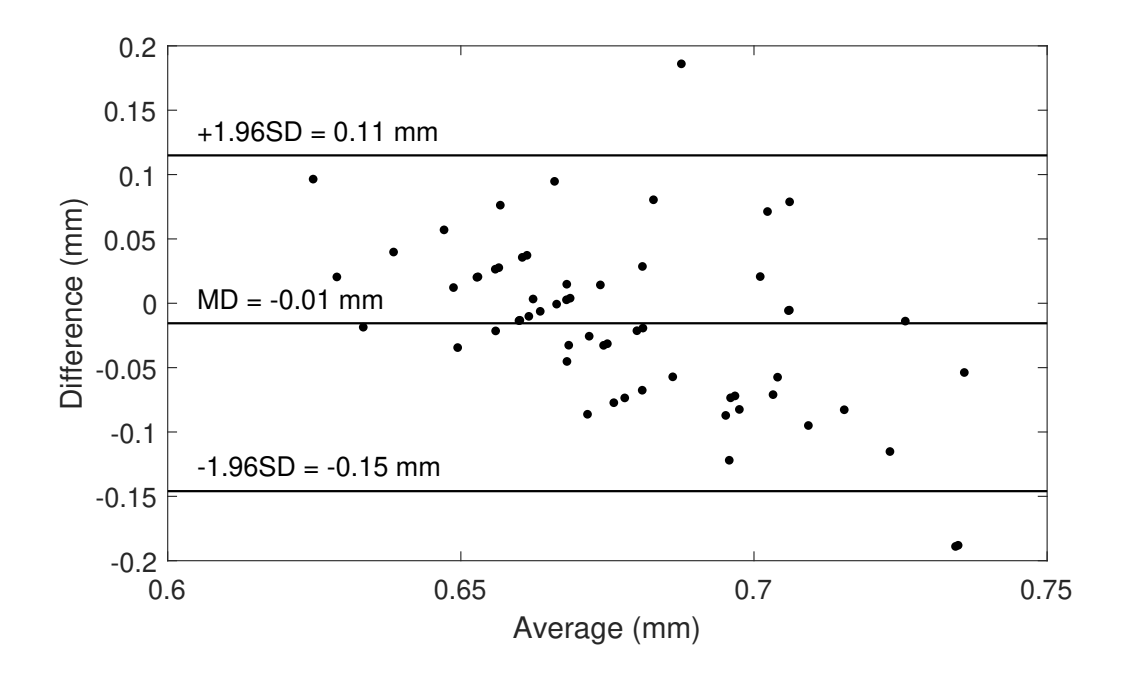
Figure 5.14: *Bland-Altman plot comparing the manual and decomposition IMT estimates.*

known (i.e., both methods may contain error). The Pearson correlation coefficient does not capture biasing errors or difference of scale in the data and is therefore not suitable to compare the agreement between two clinical methods. From the Bland-Altman plot shown in Fig.5.14 it can be seen that the methods agree within 0.11mm and -0.15 mm. This conforms to reported operator variability and may arise from the

manual labelling [111]. Further, in [111] it was noted that operator error increased with increased values of IMT. This could explain the asymmetry and skewness of the Bland-Altman plot. Since the agreement is within operator variability, and there is a low bias (MD = 0.01 mm), it follows from the Bland-Altman analysis that the proposed method may be interchangeable with the manual labelling. Further, the IMT distribution of estimates shown in Fig.5.12 (Manual) and Fig.5.9 (Proposed) indicate the proposed method using the RF signals has reduced variability. The mean and standard deviation of the proposed and manual IMT estimates were 0.67 ± 0.03 mm and 0.69 ± 0.05 mm, respectively. The manual estimates are subject to human error, which may be the source of the increased variability. However, the standard deviation of the manual estimation is the same as the depth sampling interval of the B-mode image (0.046 mm) suggesting a less variable estimate may not be expected using the envelope signals obtained by the clinical ultrasound imaging system at the sampling rates used to acquire the *in-vivo* data used for experimentation. Further study with more subjects is required to verify the accuracy and reliability of the proposed decomposition method for the IMT estimation.

5.2.2   Artery Wall Motion Tracking Using WUS

5.2.2.1   Ultrasound Dataset and Results

The decomposition method for wall echo isolation and motion tracking was applied to M-mode data obtained by the WUS system. Fig.5.15 shows an unprocessed ultrasound RF signal containing the near and far walls of a common carotid artery acquired by the WUS system. Due to the estimated WUS ultrasound frequency of
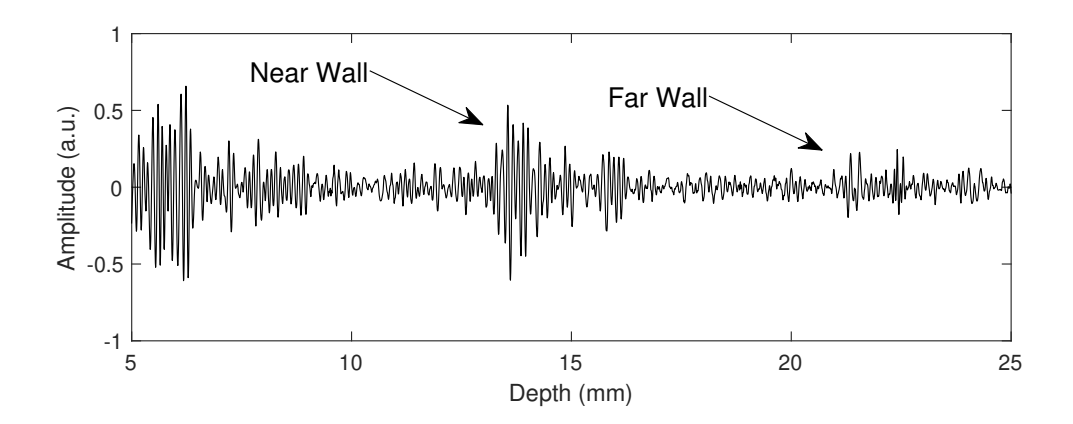
Figure 5.15: *Ultrasound RF signal of CCA acquired by WUS system.*

4 MHZ, which is lower than the clinical ultrasound imaging system, only one echo is observed from each artery wall, which may be composed of multiple echoes from layer boundaries within the artery. Therefore, the echo used for the artery wall motion tracking does not arise from a particular tissue boundary of the artery wall.

The data was manually windowed in 2.5 mm segments around each artery wall echo over the duration of the 4 second recording. Each acquired RF signal was filtered using a 6th order linear phase finite impulse response band-pass filter of 3 MHz bandwidth at the estimated ultrasound center frequency of 4 MHz. The M-mode frame rate was downsampled to 500 Hz to reduce the computational overhead. The WUS acquisition system is highly oversampled and since the pulse of the artery has a fundamental frequency of approximately 1 Hz at rest, the 1 kHz sampling rate is unnecessary for the motion tracking experiment. Four echoes were decomposed in each RF signal of the M-mode for both the near and far wall segments to capture the artery wall echo in each RF signal. It was assumed that one of the decomposed echoes corresponds to the artery wall, and the others were considered as noise. Table 5.6 shows the constraints placed on the search space during the decomposition.

Table 5.6: *Search space constraints for artery wall motion tracking using WUS.*

Parameter	Constraint
α	4 (MHz)^2
β	> 0
d	depth range of signal segment
f_c	4 MHz
ϕ	$[-\pi, \pi]$

After decomposition, the artery wall echo was isolated in each RF signal of the M-mode based on the prior knowledge of the echo characteristics (range of depths, amplitudes). Once isolated, motion tracking using the parameters of the artery wall echo was performed by Eq.4.10. For post-processing, a moving average filter with a span of 30 samples was applied to denoise the artery wall displacement estimates.

Fig.5.16 a) shows a filtered ultrasound RF signal segment containing the near wall, with the resulting decomposition shown in Fig.5.16 b). The artery wall echo (black) was successfully isolated in the decomposition.

Fig. 5.17 b) shows the M-mode of the isolated near wall echo across a 4 second recording. The isolated wall echo contains the dynamics found in the original M-mode of Fig.5.17 a).

An example of a filtered ultrasound RF signal segment containing the far wall and the resulting decomposition is shown in Fig.5.18 a) and b), respectively. The decomposition successfully isolated the wall echo (black) amidst the high amplitude tissue scattering.
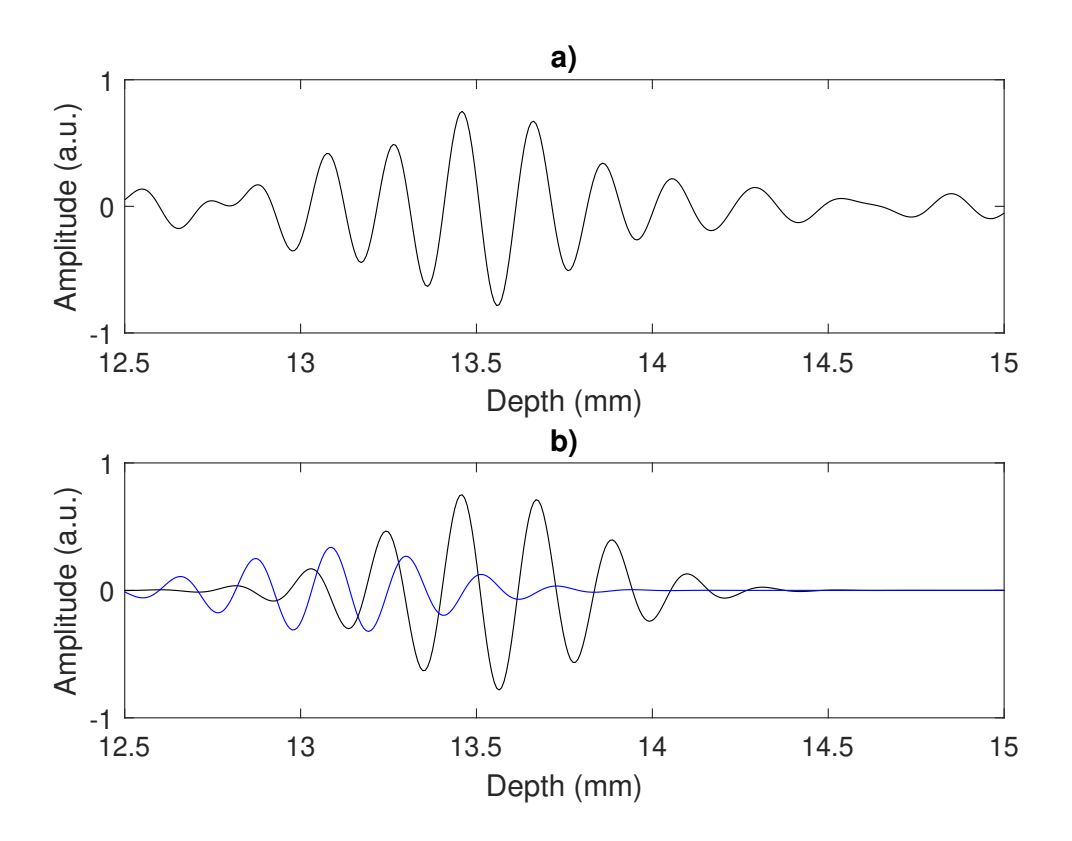
Figure 5.16: *a) Segmented and filtered ultrasound RF signal obtained by the WUS used for decomposition. b) Decomposition result.*

The decomposition captured the far wall echo in the M-mode, as shown in Fig.5.19 a) and b). The dynamics of the far wall are captured in the isolated M-mode.

Using the parameters of the isolated wall echoes in the M-modes, the motion of the near and far wall of the artery was estimated using Eq.4.10. Fig.5.20 a) shows the resulting motion of the near wall over the recording. The motion estimate is noisy due to small errors in the estimated parameters. A moving average filter containing 30 samples was applied to improve the estimated motion waveform, shown in Fig.5.21 b).

In Fig.5.21 a) and b), the raw and smoothing filtered motion estimates of the
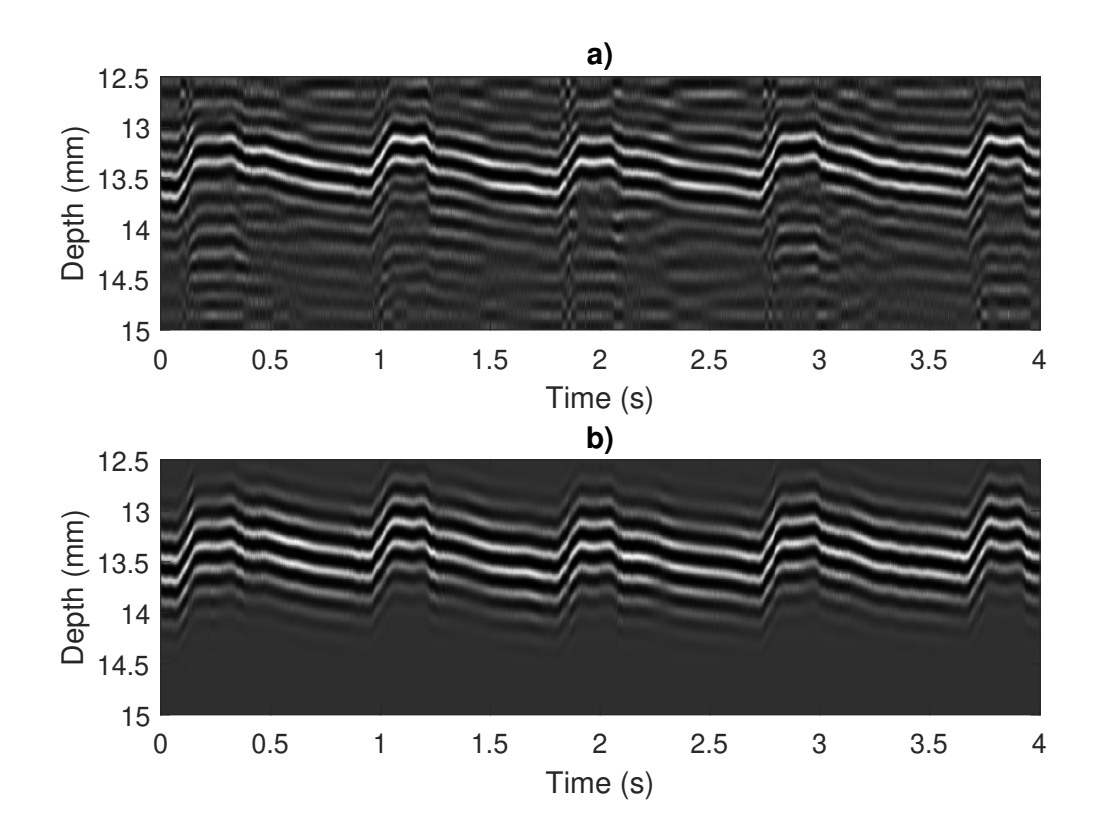
Figure 5.17: *a) Segmented and filtered WUS M-mode of the near wall used for experiment. b) M-mode containing isolated wall echo.*

far wall are shown. The raw motion estimate of the far wall, Fig.5.21 a), exhibits more noise than the near wall. The far wall echoes are highly attenuated, and are lower amplitude relative to the surrounding scattering noise echoes, causing more noise in the parameter estimation. Fig.5.21 b) shows the smoothed far wall motion estimate. Increased oscillatory motion is observed in the far wall, compared to the near wall estimate of Fig.5.20. This may be caused by differences in the mechanical properties of the artery wall tissues. The near wall motion could be damped by the dermal tissues, resulting in less oscillation in response to the blood flow.

The diameter estimate over the M-mode sequence is shown in Fig.5.22. Signal characteristics associated with the blood pressure waveform are observed [112]. The
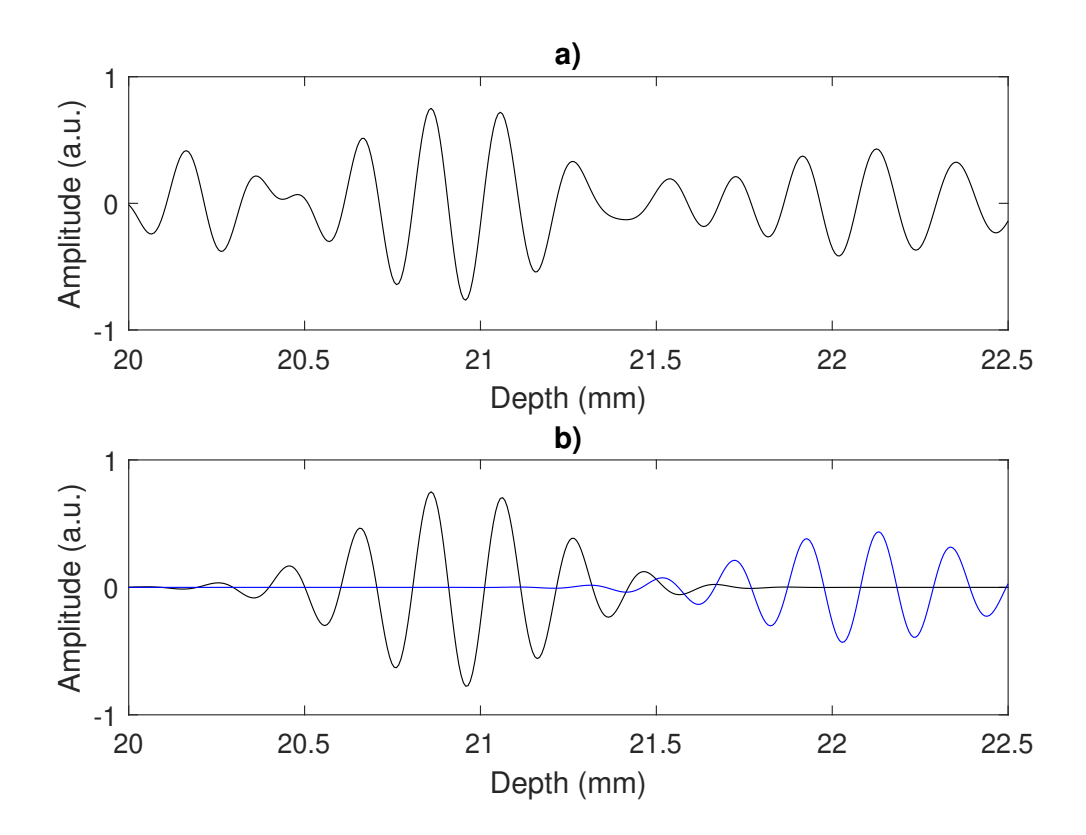
Figure 5.18: *a) Segmented and filtered WUS signal segment containing far wall.*
b) Decomposition result. The black decomposed echo corresponds to the artery far
wall echo.

decomposition approach successfully isolated the artery wall echoes of the near and

far walls in the segmented M-mode sequence. The motion estimate was computed

using prior knowledge to identify the parameter vectors corresponding to the artery

wall echoes.

One consideration is that the diameter estimate is above the references range

reported in the literature (approximately 1 mm larger) [113]. This is likely to be

due to the fact that the clinical convention is to measure the diameter from the

intima-blood boundary locations of the opposite artery walls [36], assuming the

IMT is approximately 0.5 mm on both sides. This could result in a biasing error
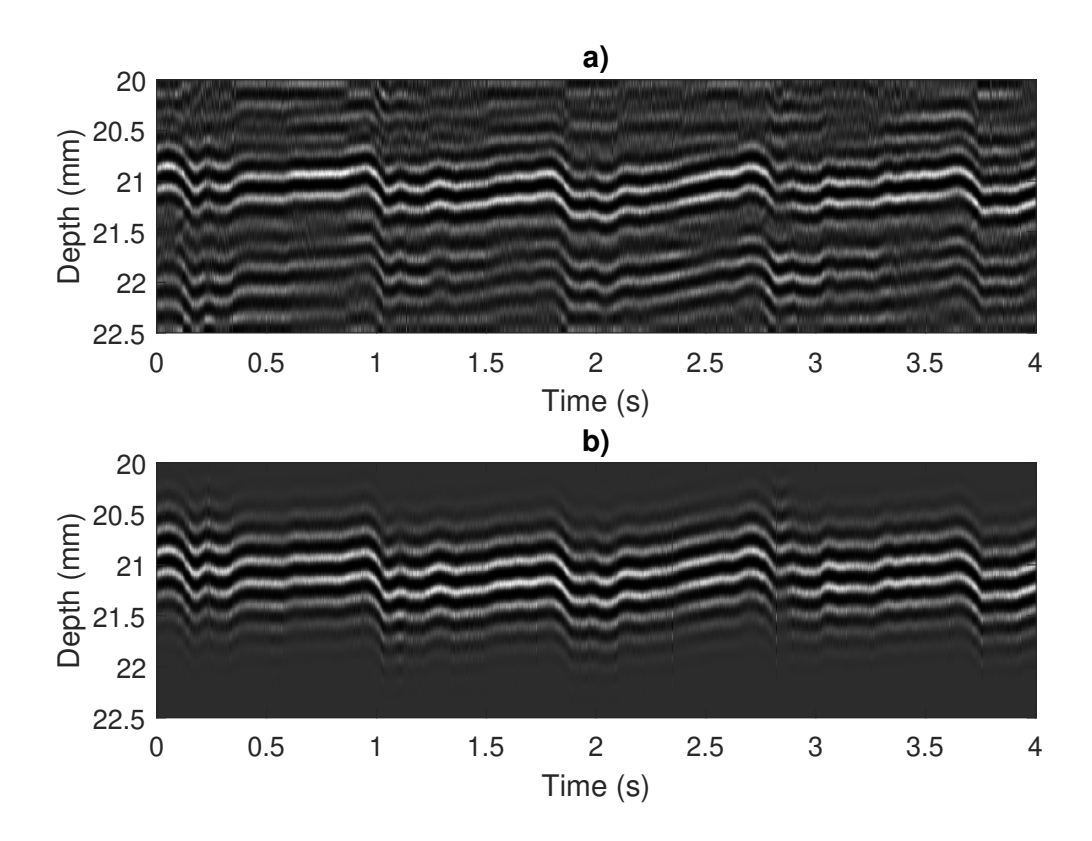
Figure 5.19: *a) Segmented and filtered WUS M-mode of the far wall used for experiment. b) M-mode containing isolated wall echo.*

from the true lumen diameter that should be accounted for and studied further using reference measurements during *in-vivo* experimentation. As can be seen in the M-mode segments shown in Fig.5.17 and Fig.5.19, the artery wall echoes have higher amplitudes compared to the tissue scattering. The echogenicity of the lumen-intima boundary is low, resulting in weak reflections that may not be identifiable within the noisy signals obtained using the WUS. Thus, the diameter measurement may be estimated from the media-adventitia boundaries instead, an interface that has a higher echogenicity, and therefore reflects higher amplitude ultrasound echoes.
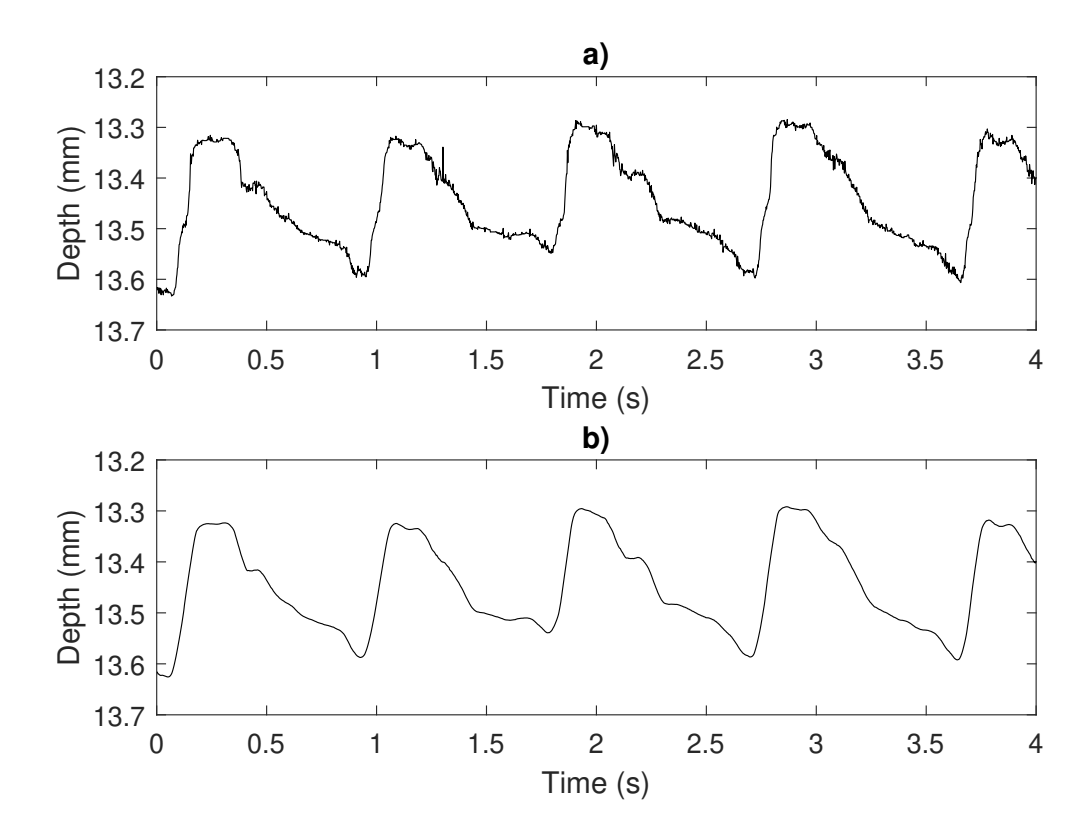
Figure 5.20: *a) Raw motion estimate of near wall. b) Motion estimate of near wall after smoothing filter.*

5.2.2.2   Comparison to Cross-Correlation

The relative motion estimates were compared to CC motion estimation [70] obtained without using the proposed RF signal decomposition and motion tracking (Eq.4.10). The same M-modes of the RF signals at the near and far wall were used for motion estimation using CC. Before motion estimation, the RF signals were interpolated 100 times to increase the depth sampling interval. This was required for the CC method to obtain reasonable motion estimates. A moving average filter was applied to the resulting motion estimates.

Fig.5.23 a) and b) show the near wall motion estimates of the proposed and CC method, respectively. The near wall echoes had higher amplitudes compared to the
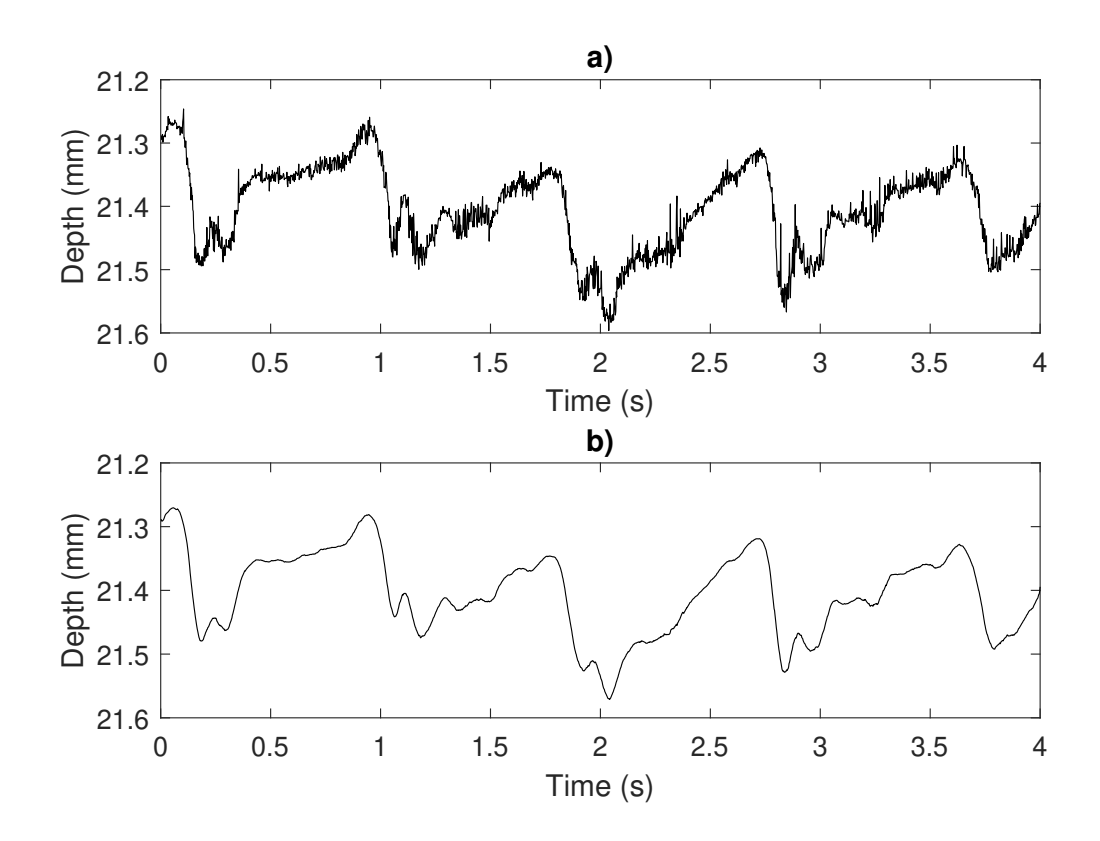
Figure 5.21: *a) Raw motion estimate of far wall. b) Motion estimate of far wall after smoothing filter.*
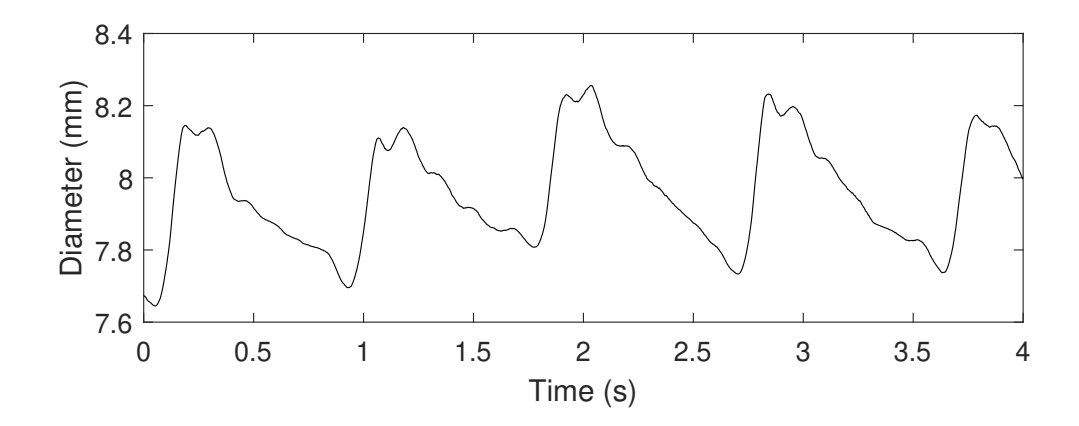
Figure 5.22: *Estimated diameter over cardiac cycles using proposed method.*

adjacent tissue scattering, and therefore the proposed and CC method performed similarly. This is illustrated in Fig.5.23 c), where the absolute difference of the estimated motion of the near wall echoes between the decomposition and CC methods
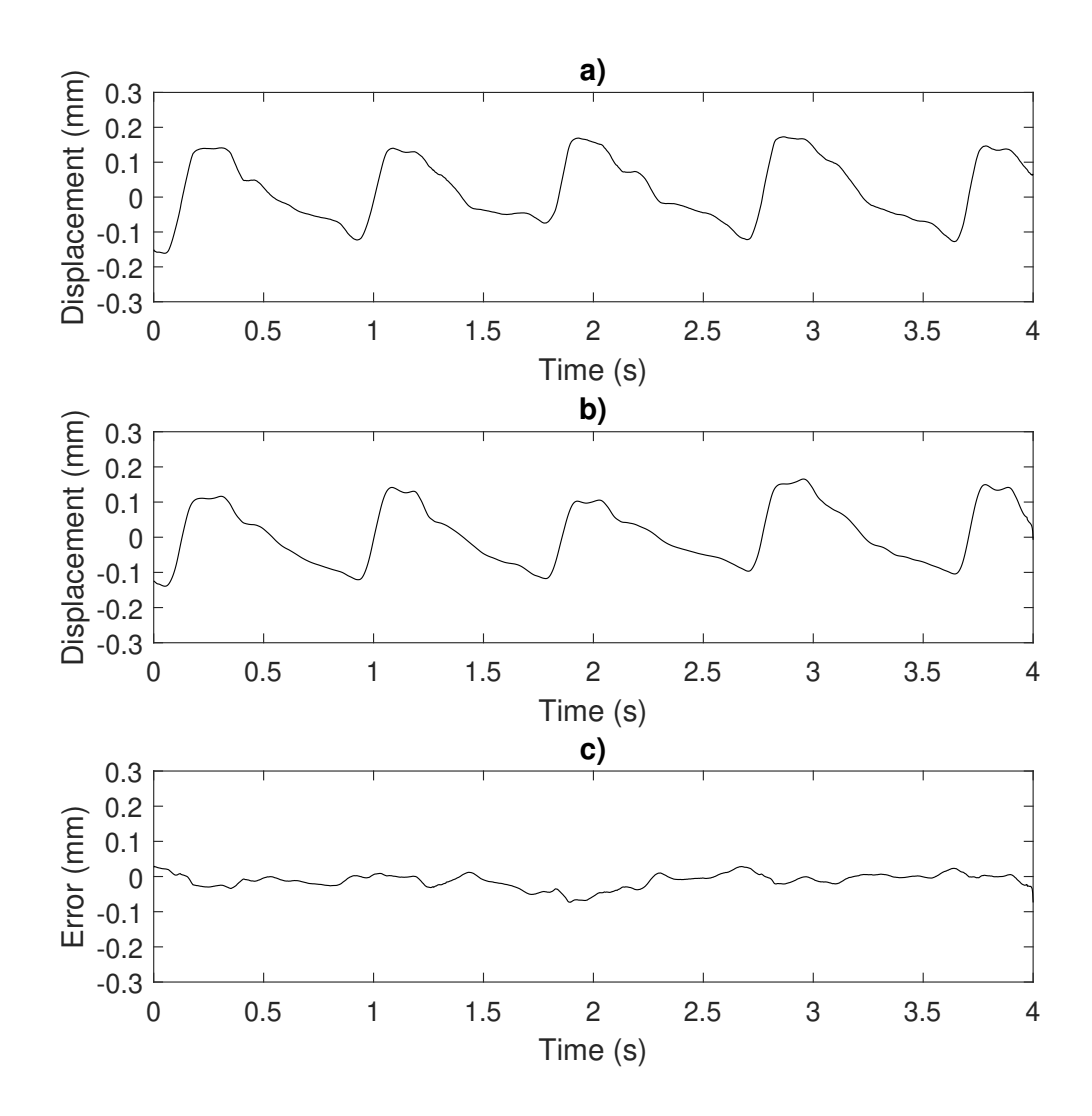
Figure 5.23: *a) Relative displacement of near wall by proposed method. b) Relative*

displacement of near wall by CC. c) Difference between methods.

is below 0.1 mm for the duration of the 4 second recording.

Fig.5.24 a) and b) shows the proposed method and CC motion estimate of the

far wall, respectively. At approximately between 2.3 and 2.4 seconds in Fig.5.24

c), a sudden increase of the displacement of about 0.2 mm can be seen due to the

corresponding sudden increase of the estimated displacement in the CC method in

Fig 5.24 (b). The CC method might have error due to the presence of high amplitude
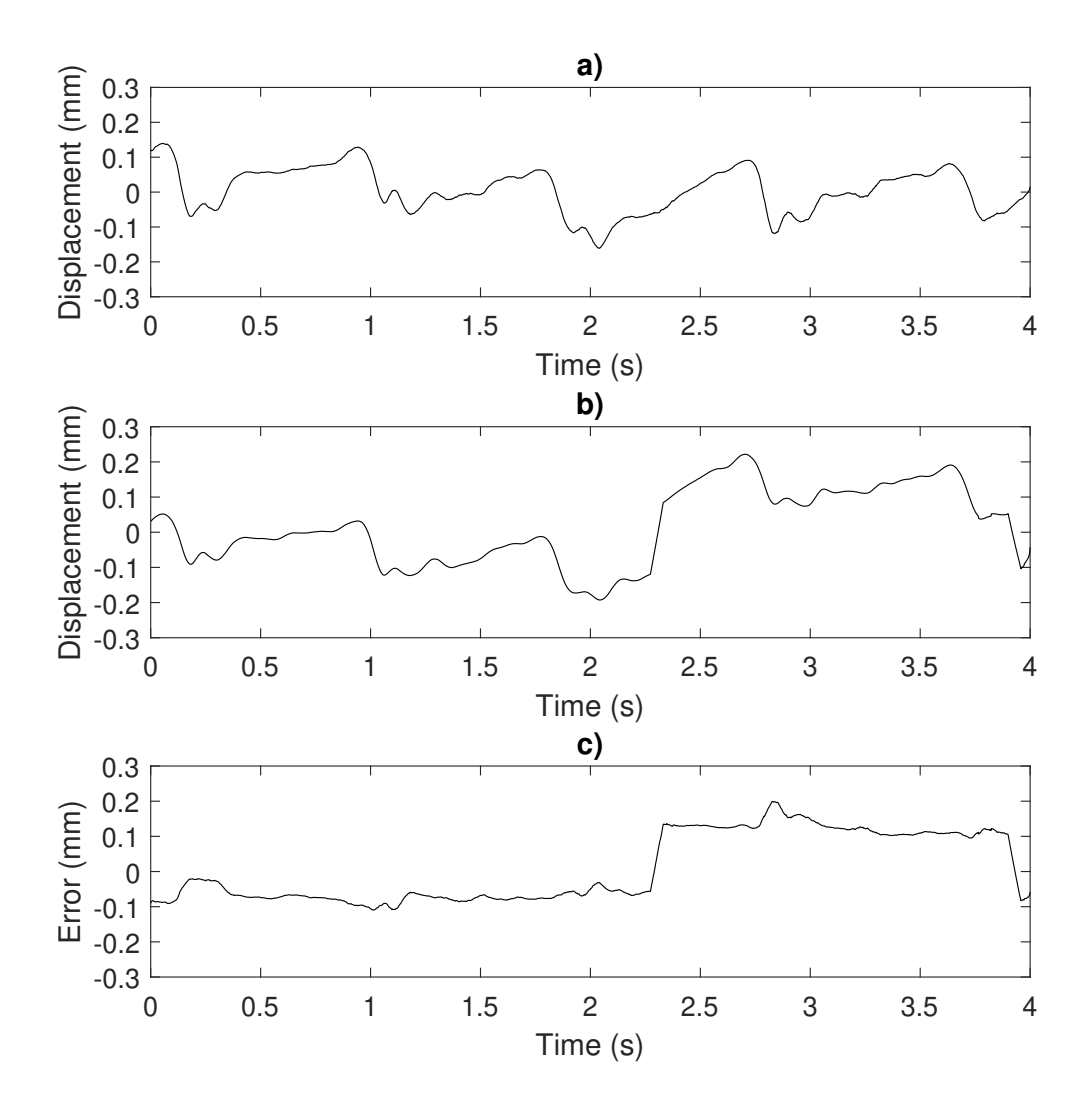
Figure 5.24: *a) Relative displacement of far wall by proposed method. b) Relative displacement of far wall by CC. c) Difference between methods.*

of tissue scattering noise echoes near the fall wall echo in the M-mode. The proposed method demonstrated robust motion tracking in the presence of additional high amplitude echoes in the M-mode, however further work is required to study the accuracy and reliability of the proposed method with multiple human subjects.

Chapter 6

Conclusions and Future Research

This chapter concludes the research study on the signal decomposition methodology for artery monitoring. The results, advantages, and limitations are summarized. A detailed discussion of future research to improve on the signal decomposition framework and address the limitations of the method that was proposed in this thesis are provided.

Section 6.1 summarizes the results of this research study, and the advantages and limitations of the proposed methodology for artery monitoring.

Section 6.2 describes the areas of future research to improve the proposed signal decomposition method for artery monitoring. Construction of a numerical simulation model of the WUS system is discussed, with the motivations and potential implementation approaches outlined. Several signal processing approaches for finding improved basis functions for automatic wall echo isolation are discussed, with the potential areas of consideration presented. Design considerations for the WUS are discussed.

6.1   Conclusions

A signal decomposition approach, using a model based on the GMS echo model was proposed for artery monitoring. The GMS echo model was selected based on its resemblance to the spatial impulse response of the ultrasound system. Decomposition of the ultrasound RF signals was performed by MP with constrained particle swarm optimization.

Numerical simulation experiments were conducted to evaluate the decomposition approach for IMT estimation when the tissue boundary layer echoes are overlapped due to the axial resolution of the ultrasound system. For realistic IMT values ($0.4 - 0.8$ mm), the error was less than 0.025 mm with the simulation conditions reflecting the clinical ultrasound system used in this work. When evaluating the effect of the ultrasound frequency on the accuracy, the upper limit of errors in the IMT estimates for 5 MHz or above was 20%. Thus, the IMT estimation accuracy was better than 80% when the ultrasonic frequency was greater than 5 MHz under the simulation conditions. Numerical simulation experiments were not performed to evaluate motion tracking, as the simulation of realistic dynamic tissue scattering echoes is an ongoing area of research, and is discussed in the future work section.

Preliminary *in-vivo* IMT estimation experiments were conducted using a clinical ultrasound system with focused beam. M-mode and B-mode segments around the far wall were decomposed and used for IMT estimation. Compared to a reference clinical technique for manual estimation of the IMT using B-mode images, the proposed method exhibited less variance on the estimates, while retaining 95% agreement within bounds reflecting operator variability of the manual estimation.

Underestimation of the IMT was observed when the greedy decomposition did not adequately capture the appropriate wall boundary echo. This may be solved by automatic identification of the desired echoes, and is a subject of future work.

The proposed method successfully isolated and tracked the echoes corresponding to the near and far artery walls using the ultrasound RF signals obtained by the WUS. Motion estimates were obtained from the near and far wall using manually segmented M-mode sequences. The diameter waveform captured characteristic signal structures associated with the continuous blood pressure waveform and cardiac events; however, it overestimated the diameter for typical males according to reference literature [114]. This is because the clinical measurement for the artery diameter is taken from the intima boundaries on either side of the artery. These echoes are faint due to the echogenicity of the interface, and thus, are exceedingly difficult to identify using the WUS with the reduced lateral and depth spatial resolution and the resulting high volume of interference in the acquired ultrasound RF signals. Thus, a biasing error is introduced that could be accounted for, for instance, by using an appropriate calibration with a reference measurement. The proposed method exhibited improved robustness for motion tracking when there is high amplitude scattering echoes in the M-mode, compared to the conventional CC motion estimator.

Discrimination of the wall echoes based on features (parameter vectors) of the signal model was not successful, possibly due to the sub-optimal choice of the model, and the constraints imposed in this work for practical implementation using the greedy decomposition method. The main limitation of the method proposed in this

work is the inability to discriminate the wall echoes from the surrounding echoes using the parameters of the chosen model.

6.2   Discussion for Future Research

This section provides a discussion on areas of future research that should be conducted to address limitations of the proposed method. Future research should focus on identifying a method that provides a decomposition basis that results in automatically differentiating the artery wall echo from the undesired scattering echoes. Future research should also include more data collection and statistical analysis of the proposed method for artery wall thickness estimation and motion tracking. Additional simulation experiments for white noise could be considered for further evaluation of the robustness of the proposed method. Further, the numerical simulation model was simplistic and may not provide a realistic evaluation of the *in-vivo* performance. Due to the difficulties obtaining a ground truth measurement *in-vivo*, and the simplicity of many *in-vitro* models, a realistic numerical simulation model is desirable.

Section 6.2.1 describes several signal processing approaches that could be useful in obtaining a discriminable basis for wall echo isolation that retains physical interpretation of the composing echoes. Considerations for each approach are outlined.

Section 6.2.2 provides a discussion on the usefulness of a realistic numerical simulation model of ultrasound RF signals acquired from the artery, particularly those acquired by the WUS system.

6.2.1 Discriminable Basis for Automatic Identification of Wall Echoes

The GMS echo model and the MP-based signal decomposition results in a set of parameter vectors that cannot be used as features for discrimination of the wall echoes from tissue echoes. Originally it was hypothesized, based on [115], that the parameter vectors of the estimated echoes would have characteristics that were different from the tissue echoes. This would create a set of features that could be used to train a model for automatic identification of wall echoes from tissue scatterers. In this scenario, a clustering algorithm such as k-nearest neighbors [116] may be used to learn regions of the parameter space that correspond to the wall echoes. Then, using the learned regions, the search space could be constrained within the wall echo parameter space, resulting in automatic isolation. This was not found to be possible using the GMS model and MP decomposition, in part due to the tight constraints needed to obtain physically interpretable echo estimates, and the subsequent lack of range in the estimated parameters. Future work should focus on developing a method to provide a decomposition basis that results in differentiating the artery wall echo from the undesired scattering echoes. Several potential approaches could be taken toward achieving this and are discussed in the proceeding subsections.

6.2.1.1 Dynamic Mode Decomposition

Dynamic mode decomposition (DMD) [117] is an emerging method of data-driven dynamical analysis of complex systems, of which the governing equations are unknown or are difficult to model. Using measurement snapshots of the time evolution

of a system, DMD seeks to extract spatiotemporal eigenvalues that describe the system dynamics. Building upon this, DMD could be used to design a selective filter that isolates dynamic artery wall echoes from stationary tissue echoes.

One weakness of the DMD approach for extracting spatiotemporal modes from data is the inability to correctly capture low-rank dynamics in the presence of rotational or translational invariant structures in the data [118]. Translational invariance is present in the ultrasound RF signals comprising an M-mode sequence as correlated signal structures (i.e. the echo shape) and thus the dynamical modes of the system are not well captured. Extraction of the low-rank spatiotemporal modes using DMD in the presence of translational invariance in the data is an ongoing area of research.

Multi-resolution DMD, a reformulation of the algorithm with incorporation of concepts similar to the wavelet transform has been proposed as a candidate approach to address this issue. The dynamical modes can then be separated based on their velocity and location [119]. This technique divides the data snapshots into partitions, where the partitions do not contain translational or rotational invariance. However, multi-resolution approaches may not be sufficient to extract the wall echo dynamics from stationary tissue echoes, since they are within the same location and velocity bands. Additional research is needed to implement DMD on the ultrasound signals due to the correlated echo structures.

6.2.1.2   Empirical Wavelet Transform

The empirical wavelet transform [120] is an adaptive method of signal decomposition that seeks to incorporate the flexibility and usefulness of extracting non-stationary

signal components given by the empirical mode decomposition [121] with the mathematically rigorous underpinnings of the wavelet transform. This approach proposes a subdivision of the frequency spectrum of a signal as a means of extracting wavelet structures that are adapted to the analyzed signal.

The empirical wavelet transform may be considered for learning the basis functions from the data to discriminate the wall echoes. While the method proposed in [120] adapts the wavelets to the signal, the spectrum shape is not used to construct the adapted wavelets (i.e., the adaptation is performed on the bandwidth of the Butterworth filters used for the wavelet decomposition). Thus, the proposed method only adapts the wavelet frequency-bands used for the multi-resolution analysis. To find basis wavelets for wall echo isolation, it could be useful to incorporate the spectrum shape for construction of each adapted wavelet. An additional challenge that would have to be addressed for implementation of this decomposition approach is that varying spectra of the received ultrasound signals across successive pulses. This could create difficulties extracting the most representative wavelets from the data.

6.2.1.3   Shapelet Transform

The shapelet transform is a recently proposed method for time series data mining, with application to anomaly and event detection and classification within a signal [122]. Shapelets have found application in seismic signal processing for earthquake detection, tornado prediction and breaking wave identification [123]. The shapelet transform uses subsequences within the analyzed signals for class discrimination or even detection problems. These can either be automatically mined from the data, or defined by the designer as features for a system. An approach similar to shapelet

transform could facilitate learning the optimal basis functions for discrimination of the wall echo regions.

An attractive feature of shapelets is that they result in fully interpretable and explainable systems when coupled with machine learning algorithms for automatic identification. For automated medical systems, an issue that could require significant attention is retaining explainability in the model. This could be important for clinicians to understand and have confidence in the results of such systems to inform medical decision-making.

6.2.2   Construction of a Simulation Phantom for Wearable Ultrasound System

The simulation experiments conducted in this work are too idealistic to pragmatically evaluate the *in-vivo* performance of the signal processing methodology. The effectiveness of *in-vivo* experimentation for the evaluation of novel methods is often limited due to the lack of ground truth for the physiological parameters of interest. Further, *in-vitro* models are often too simplistic to offer a pragmatic assessment of the algorithm performance, and thus are not suitable for algorithm verification. Alternatively, computer simulation models have demonstrated utility in validating new ultrasound signal processing algorithms by allowing control of the physiological and system parameters used for experimentation while retaining realistic measurement conditions [124]–[126].

The proposed future research involves the construction of a realistic artery phantom using numerical simulations, and an ultrasound signal simulation representative

of the WUS system. Of particular interest is simulating the ultrasound RF signals obtained from the artery by the WUS technology. Since the WUS is a novel sensor, the acoustic properties differ from the conventional UTs. Realistically simulating the pressure field emitted by the WUS and the received ultrasound RF signals from the artery monitoring area, including the surrounding tissues with cardiac cycles, would help optimize the WUS design, monitoring configuration, and signal processing algorithms.

6.2.3   Considerations for WUS Design

Several design considerations may be investigated for further development of the WUS. These include sensor configurations, and design of the excitation pulse.

Array-type WUS may be designed using the PVDF material, similar to [127]. This would allow focusing of the ultrasound beam, resulting in improved lateral resolution that could reduce the severity of scattering noises in the acquired RF signals. Further, the array-type WUS would allow continuous monitoring of B-mode images. Multi-sensor approaches may also be considered using the WUS (not in array configuration). These could include multiple WUS at different locations for the estimation of the pulse wave velocity, a key parameter in noninvasive blood pressure estimation. Additionally, multi-modal sensing may be considered by simultaneously monitoring the electrocardiogram signals.

Design of the excitation pulse may offer some advantages over excitation schemes using impulse functions. Chirp coded excitation was shown to improve the signal-to-noise ratio without lowering axial resolution [128]. Further, coded excitation

may improve the penetration depth of higher frequency ultrasound [129]. Multiple frequency excitation could also be useful for automatic identification of the artery wall tissues based on their acoustic properties [130].

Chapter A

Appendix

A.1   Ultrasound Scattering Conditions
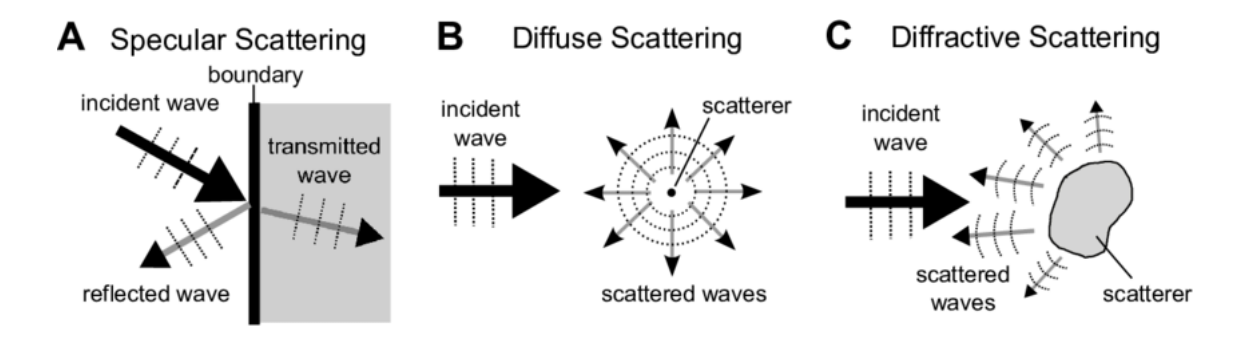
Figure A.1: *Illustration of the types of ultrasound scattering. Figure from [131].*

When a propagating ultrasound wave encounters an interface of two materials with differing acoustic impedance, a reflection of some of the acoustic energy occurs. The characteristics of this reflection is dependent, in part, on the size and geometry of the interface. Specular scattering occurs when there is a smooth boundary greater than the wavelength of the ultrasound wave. This results in the reflection of some of the acoustic energy in a defined direction determined by the angle of incidence. Diffuse scattering occurs when the interface is much smaller than the wavelength of the ultrasound. In this case, the reflection propagates in many directions, interfering with other acoustic waves and structures in the media. Diffractive scattering occurs when the reflecting object is large with respect to the wavelength, but has a rough boundary. This again results in the reflected acoustic wave propagating in many directions. Non-specular scattering is a major source of noise in medical ultrasound imaging, causing interference and obscuring the structure of underlying tissues.

A.2   Ultrasound Resolution

Distinguishing closely spaced reflectors using ultrasound imaging requires the resolution of the system to be sufficiently high with respect to the spacing of the reflectors.

Axial resolution refers to the ability to discern closely spaced reflectors that are spaced parallel to the beam propagation. This is affected by the ultrasound frequency and bandwidth (spatial pulse-width).

The lateral resolution refers to the ability to discern closely spaced reflectors that are spaced perpendicular to the beam propagation. This is affected by the transducer geometry and focusing of the beam. The lateral resolution is roughly comparable to the wavelength of the ultrasound beam at the focal point.
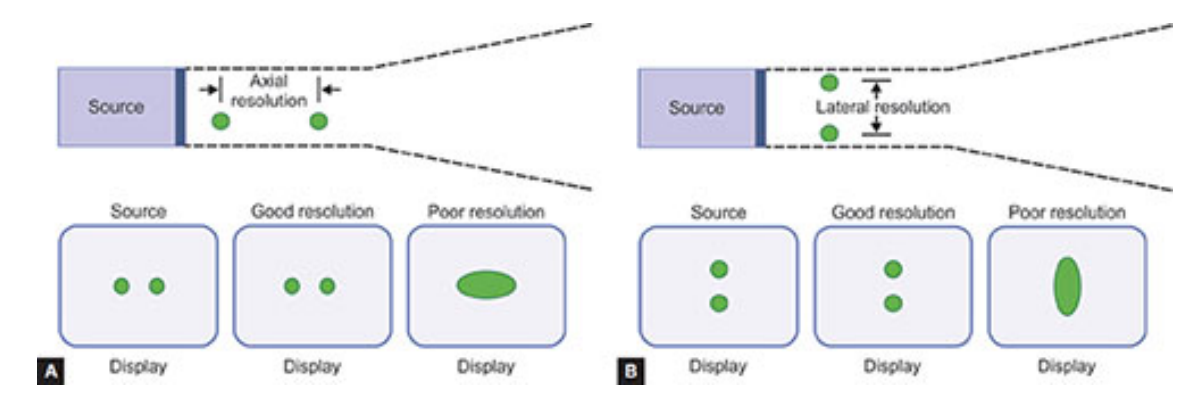
Figure A.2: *Illustration of axial and lateral resolution in ultrasound. Figure from [132].*

A.3   Cross-Correlation

CC is a similarity measure between two signals that describes the correlation of one signal with shifted copies of another. The CC between two signals is defined as:

$$(f * g)(\tau) = \int_{-\infty}^{\infty} f(t)\overline{g(t - \tau)}d\tau \tag{A.1}$$

where $\overline{g(t - \tau)}$ denotes the shifted complex conjugate of the signal $g(t)$.

Bibliography

[1] G. of Canada. (2021). "Action for seniors report," [Online]. Available: `https://www.canada.ca/en/employment-social-development/programs/seniors-action-report.html` (visited on 06/15/2021).

[2] J. Evans, A. Papodopoulos, C. Tsien Silvers, *et al.*, "Remote health monitoring for older adults and those with heart failure: Adherence and system usability," *Telemedicine Journal and E-Health*, vol. 22, no. 6, pp. 480–488, 2016.

[3] G. of Canada. (2021). "Heart disease in Canada," [Online]. Available: `https://www.canada.ca/en/public-health/services/publications/diseases-conditions/heart-disease-canada.html` (visited on 06/15/2021).

[4] S. Chrysant, "A new paradigm in the treatment of the cardiovascular disease continuum: Focus on prevention," *Hippokratia*, vol. 15, no. 1, pp. 7–11, 2011.

[5] J. Lee, Z. Ghasemi, C.-S. Kim, H.-M. Cheng, and C.-H. Chen, "Investigation of viscoelasticity in the relationship between carotid artery blood pressure and distal pulse volume waveforms," *IEEE Journal of Biomedical and Health Informatics*, vol. 22, no. 2, pp. 460–470, 2017.

[6] M. J. Roman, Z. N. Tasneem, J. M. Gardin, M. Gerhard-Herman, M. Jaff, and E. Mohler, "Clinical application of noninvasive vascular ultrasound in cardiovascular risk stratification: A report from the American society of echocardiography and the society of vascular medicine and biology," *American Society of Echocardiography Report*, vol. 19, no. 8, pp. 943–954, 2006.

[7] G. M. London and B. Pannier, "Arterial functions: How to interpret the complex physiology," *Nephrology Dialysis Transplantation*, vol. 25, no. 12, pp. 3815–3823, 2010.

[8] R. T. Hurst, D. W. Ng, C. Kendall, and B. Khandheria, "Clinical use of carotid intima-media thickness: Review of the literature," *Journal of the American Society of Echocardiography*, vol. 20, no. 7, pp. 907–914, 2007.

[9] A. Huang, M. Yoshida, Y. Ono, and S. Rajan, "Continuous measurement of arterial diameter changes using a wearable and flexible ultrasonic sensor," *IEEE International Ultrasonics Symposium*, pp. 1–4, 2017.

[10] Z. Wang, M. J. Golob, and N. C. Chesler, "Viscoelastic properties of cardiovascular tissues," in *Viscoelastic and viscoplastic materials*, 2nd ed., InTech, 2016, ch. 7, pp. 141–163.

[11] C. G. Caro, T. J. Pendley, R. C. Schroter, and W. A. Seed, "The mechanics of circulation," in, 2nd ed. Cambridge University Press, 2011, ch. 7, pp. 86–104.

[12] (2021). "Artery structure, function, and disease," [Online]. Available: `https://www.thoughtco.com/artery-anatomy-373235` (visited on 07/31/2021).

[13] J. D. Humphrey, "Cardiovascular solid mechanics: Cells, tissues, and organs," in, 1st ed. Springer Science & Business Media, 2013, ch. 2, pp. 249–364.

[14] P. Segers, E. R. Rietzschel, and J. A. Chirinos, "How to measure arterial stiffness in humans," *Arteriosclerosis, Thrombosis and Vascular Biology*, vol. 40, no. 5, pp. 1034–1043, 2020.

[15] D. Mehta and A. B. Malik, "Signaling mechanisms regulating endothelial permeability," *Physiological Reviews*, vol. 86, no. 1, pp. 279–367, 2006.

[16] D. Versari, E. Daghini, A. Virdis, L. Ghiadoni, and S. Taddei, "Endothelial dysfunction as a target for prevention of cardiovascular disease," *Diabetes and Cardiovascular Disease*, vol. 32, no. 2, pp. 314–321, 2009.

[17] R. J. Widmer and A. Lerman, "Endothelial dysfunction and cardiovascular disease," *Global Cardiology Science and Practice*, vol. 2014, no. 3, p. 43, 2014.

[18] J. W. Hunt, M. Arditi, and F. S. Foster, "Ultrasound transducers for pulse-echo medical imaging," *IEEE Transactions on Biomedical Engineering*, no. 8, pp. 453–481, 1983.

[19] A. Carovac, F. Smajlovic, and D. Junuzovic, "Application of ultrasound in medicine," *Acta Informatica Medica*, vol. 19, no. 3, p. 168, 2011.

[20] R. S. C. Cabbold, *Foundations of biomedical ultrasound*, Illustrated. 2007.

[21] I. AlMohimeed and Y. Ono, "Ultrasound measurement of skeletal muscle contractile parameters using flexible and wearable single-element ultrasonic sensor," *Sensors*, vol. 20, no. 13, p. 3616, 2020.

[22] R. Giannetti, A. Petrella, J. Bach, and A. Silverman, "Feasibility of in-vivo bone depth measurement using high frequency ultrasound," *IEEE Instrumentation and Measurement Technology Conference*, pp. 762–766, 2015.

[23] A. J. Fernandes, Y. Ono, and E. Ukwatta, "Flexible and wearable ultrasonic sensors and method for classifying individual finger flexions," *IEEE International Conference of Flexible, Printable Sensors and Systems*, pp. 5–8, 2020.

[24] X. Yang, X. Sun, D. Zhou, Y. Li, and H. Liu, "Towards wearable a-mode ultrasound sensing for real-time finger motion recognition," *IEEE Transactions on Neural Systems and Rehabilitation Engineering*, vol. 26, no. 6, pp. 1199–1208, 2018.

[25] Y. Xin, C. Guo, X. Qi, *et al.*, "Wearable and unconstrained systems based on PVDF sensors in physiological signals monitoring: A brief review," *Ferroelectrics*, vol. 500, no. 1, pp. 291–300, 2016.

[26] L. F. Brown, "Design considerations for piezoelectric polymer ultrasound transducers," *IEEE Transactions on Ultrasonics, Ferroelectrics, and Frequency Control*, vol. 47, no. 6, pp. 1377–1396, 2000.

[27] I. AlMohimeed, H. Turkistani, and Y. Ono, "Development of wearable and flexible ultrasonic sensor for skeletal muscle monitoring," *IEEE International Ultrasonics Symposium*, pp. 1137–1140, 2013.

[28] P. E. Bloomfield, W.-J. Lo, and P. A. Lewin, "Experimental study of the acoustical properties of polymers utilized to construct PVDF ultrasonic transducers and the acousto-electric properties of PVDF and P(VDF/TrFE) films,"

IEEE Transactions on Ultrasonics, Ferroelectrics, and Frequency Control, vol. 47, no. 6, pp. 1397–1405, 2000.

[29] S. Krishnasamy Venugopal, *Automatic arterial wall detection and diameter tracking using M-mode ultrasound*, M.A.Sc Thesis, Department of Systems and Computer Engineering, Carleton University, 2020.

[30] J. F. Polak, M. J. Pencina, K. M. Pencina, C. J. O'Donnell, P. A. Wolf, and R. B. D'Agostino Sr, "Carotid wall intima-media thickness and cardiovascular events," *New England Journal of Medicine*, vol. 365, no. 3, pp. 213–221, 2011.

[31] M. Rafieian-Kopaei, M. Setorki, M. Doudi, A. Baradaran, and H. Nasri, "Atherosclerosis: Process, indicators, risk factors and new hopes," *International Journal of Preventive Medicine*, vol. 5, no. 8, pp. 927–946, 2014.

[32] M. L. Bots and D. E. Grobbee, "Intima media thickness as a surrogate marker for generalised atherosclerosis," *Cardiovascular Drugs and Therapy*, vol. 16, no. 4, pp. 341–351, 2002.

[33] K. Cheng, D. P. Mikhailidis, G. Hamilton, and A. M. Seifalian, "A review of the carotid and femoral intima-media thickness as an indicator of the presence of peripheral vascular disease and cardiovascular risk factors," *Cardiovascular Research*, vol. 54, no. 3, pp. 528–538, 2002.

[34] P. J. Touboul, M. G. Hennerici, S. Meairs, *et al.*, "Mannheim carotid intima-media thickness consensus (2004–2006)," *Cerebrovascular Diseases*, vol. 23, no. 1, pp. 75–80, 2007.

[35] B. Coll and S. B. Feinstein, "Carotid intima-media thickness measurements: Techniques and clinical relevance," *Current Atherosclerosis Reports*, vol. 10, no. 5, pp. 444–450, 2008.

[36] J. Wikstrand, "Methodological considerations of ultrasound measurement of carotid artery intima-media thickness and lumen diameter," *Clinical Physiology and Functional Imaging*, no. 6, pp. 341–345, 2007.

[37] F. Molinari, G. Zeng, and J. S. Suri, "A state of the art review on intima-media thickness (imt) measurement and wall segmentation techniques for carotid ultrasound," *Computer Methods and Programs in Biomedicine*, vol. 100, no. 3, pp. 201–221, 2010.

[38] A. Mohamed Moubark, D. M. Cowell, S. Harput, and S. Freear, "New denoising unsharp masking method for improved intima media thickness measurements with active contour segmentation," *IEEE International Ultrasonics Symposium*, pp. 1–4, 2018.

[39] F. Destrempes, J. Meunier, M. F. Giroux, G. Soulez, and G. Cloutier, "Segmentation of ultrasonic B-mode images of healthy carotid arteries using mixtures of Nakagami distributions and stochastic optimization," *IEEE Transactions on Medical Imaging*, vol. 28, no. 2, pp. 215–229, 2009.

[40] Q. Liang, I. Wendelhag, J. Wikstrand, and T. Gustavsson, "A multiscale dynamic programming procedure for boundary detection in ultrasonic artery images," *IEEE Transactions on Medical Imaging*, vol. 19, no. 2, pp. 127–142, 2000.

[41] X. Xu, Y. Zhou, X. Cheng, E. Song, and G. Li, "Ultrasound intima-media segmentation using hough transform and dual snake model," *Computerized Medical Imaging and Graphics*, vol. 36, no. 3, pp. 248–258, 2012.

[42] S. Dogan, Y. Plantinga, J. M. Dijk, *et al.*, "Manual B-mode versus automated radio-frequency carotid intima-media thickness measurements," *Journal of the American Society of Echocardiography*, vol. 22, no. 10, pp. 1137–1144, 2009.

[43] P. J. Touboul, M. G. Hennerici, S. Meairs, *et al.*, "Mannheim carotid intima-media thickness and plaque consensus (2004–2006–2011)," *Cerebrovascular Diseases*, vol. 34, no. 4, pp. 290–296, 2012.

[44] S. E. Greenwald, "Ageing of the conduit arteries," *The Journal of Pathology: A Journal of the Pathological Society of Great Britain and Ireland*, vol. 211, no. 2, pp. 157–172, 2007.

[45] N. M. Van Popele, D. E. Grobbee, M. L. Bots, *et al.*, "Association between arterial stiffness and atherosclerosis: The rotterdam study," *Stroke*, vol. 32, no. 2, pp. 454–460, 2001.

[46] M. E. Safar, R. Asmar, A. Benetos, *et al.*, "Interaction between hypertension and arterial stiffness: An expert reappraisal," *Hypertension*, vol. 72, no. 4, pp. 796–805, 2018.

[47] F. Alva, V. Samaniego, V. Gonzalez, R. Moguel, and E. Meaney, "Structural and dynamic changes in the elastic arteries due to arterial hypertension and hypercholesterolemia," *Clinical Cardiology*, vol. 16, no. 8, pp. 614–618, 1993.

[48] S. J. Zieman, V. Melenovsky, and D. A. Kass, "Mechanisms, pathophysiology, and therapy of arterial stiffness," *Arteriosclerosis, Thrombosis, and Vascular Biology*, vol. 25, no. 5, pp. 932–943, 2005.

[49] A. N. Lyle and U. Raaz, "Killing me unsoftly: Causes and mechanisms of arterial stiffness," *Arteriosclerosis, Thrombosis, and Vascular Biology*, vol. 37, no. 2, pp. 1–11, 2017.

[50] S. R. Waldstein, S. C. Rice, J. F. Thayer, S. S. Najjar, A. Scuteri, and A. B. Zonderman, "Pulse pressure and pulse wave velocity are related to cognitive decline in the Baltimore longitudinal study of aging," *Hypertension*, vol. 51, no. 1, pp. 99–104, 2008.

[51] C. Vlachopoulos, K. Aznaouridis, and C. Stefanadis, "Prediction of cardiovascular events and all-cause mortality with arterial stiffness: A systematic review and meta-analysis," *Journal of the American College of Cardiology*, vol. 55, no. 13, pp. 1318–1327, 2010.

[52] J. D. Humphrey, D. G. Harrison, C. A. Figueroa, P. Lacolley, and S. Laurent, "Central artery stiffness in hypertension and aging: A problem with cause and consequence," *Circulation Research*, vol. 118, no. 3, pp. 379–381, 2016.

[53] S. S. Franklin, "Arterial stiffness and hypertension: A two-way street?" *Hypertension*, vol. 45, no. 3, pp. 349–351, 2005.

[54] E. C. Godia, R. Madhok, J. Pittman, *et al.*, "Carotid artery distensibility: A reliability study," *Journal of Ultrasound in Medicine*, vol. 26, no. 9, pp. 1157–1165, 2007.

[55] Z. Gao, H. Xiong, Z. Liu, *et al.*, "Robust estimation of carotid artery wall motion using the elasticity-based state-space approach," *Medical Image Analysis*, vol. 37, pp. 1–21, 2017.

[56] A. Giachetti, "Matching techniques to compute image motion," *Image and Vision Computing*, vol. 18, no. 3, pp. 247–260, 2000.

[57] M. Persson, A. Ryden Ahlgren, A. Eriksson, T. Jansson, H. Persson, and K. Lindstrom, "Non-invasive measurement of arterial longitudinal movement," *IEEE International Ultrasonics Symposium*, vol. 2, pp. 1783–1786, 2002.

[58] S. Golemati, A. Sassano, M. J. Lever, A. A. Bharath, S. Dhanil, and A. N. Nicolaides, "Carotid artery wall motion estimated from B-mode ultrasound using region tracking and block matching," *Ultrasound in Medicine and Biology*, vol. 29, no. 3, pp. 387–399, 2003.

[59] M. Cinthio, A. R. Ahlgren, T. Jansson, A. Eriksson, H. W. Persson, and K. Lindstrom, "Evaluation of an ultrasonic echo-tracking method for measurements of arterial wall movements in two dimensions," *IEEE Transactions on Ultrasonics, Ferroelectrics and Frequency Control*, vol. 52, no. 8, pp. 1300–1311, 2005.

[60] Z. Gao, Y. Li, Y. Sun, *et al.*, "Motion tracking of the carotid artery wall from ultrasound image sequences: A nonlinear state-space approach," *IEEE Transactions on Medical Imaging*, vol. 37, no. 1, pp. 273–283, 2018.

[61] R. Kandepu, B. Foss, and L. Imsland, "Applying the unscented Kalman filter for nonlinear state estimation," *Journal of Process Control*, vol. 18, no. 7-8, pp. 753–768, 2008.

[62]   C. Xiao, Z. Li, J. Lu, *et al.*, "A new deep learning method for displacement tracking from ultrasound RF signals of vascular walls," *Computerized Medical Imaging and Graphics*, vol. 87, p. 101 819, 2021.

[63]   H. Zhang, W. Ni, W. Yan, J. Wu, H. Bian, and D. Xiang, "Visual tracking using Siamese convolutional neural network with region proposal and domain specific updating," *Neurocomputing*, vol. 275, pp. 2645–2655, 2018.

[64]   T. Mitsa. (2019). "How do you know you have enough training data?" [Online]. Available: `https://towardsdatascience.com/how-do-you-know-you-have-enough-training-data` (visited on 06/17/2021).

[65]   A. P. G. Hoeks, P. J. Brands, F. A. M. Smeets, and R. S. Reneman, "Assessment of the distensibility of superficial arteries," *Ultrasound in Medicine and Biology*, vol. 16, no. 2, pp. 121–128, 1990.

[66]   J. O. Arndt, J. Klauske, and F. Mersch, "The diameter of the intact carotid artery in man and its change with pulse pressure," *Pflugers Arch Gesamte Physiol Menschen Tiere*, vol. 301, pp. 230–240, 1968.

[67]   D. H. Groves, T. Powalowski, and D. N. White, "A digital technique for tracking moving interfaces," *Ultrasound in Medicine and Biology*, vol. 8, no. 2, pp. 185–190, 1982.

[68]   D. E. Hokanson, D. J. Mozersky, D. S. Summer, and D. E. Strandness, "A phase-locked echo tracking system for recording arterial diameter changes in-vivo," *Journal of Applied Physiology*, vol. 32, no. 5, pp. 728–733, 1972.

[69] V. Raj Kiran, P. Nabeel, M. Sivaprakasam, and J. Joseph, "Phantom evaluation of a time warping based automated arterial wall recognition and tracking method," *IEEE International Symposium on Medical Measurements and Applications*, pp. 1–6, 2021.

[70] S. Rabben, S. Bjaerum, V. Sorhus, and H. Torp, "Ultrasound-based vessel wall tracking: An auto-correlation technique with RF center frequency estimation," *Ultrasound in Medicine and Biology*, vol. 28, no. 4, pp. 507–517, 2002.

[71] P. Brands, A. Hoeks, L. Ledoux, and R. S. Reneman, "A radio frequency domain complex cross-correlation model to estimate blood flow velocity and tissue motion by means of ultrasound," *Ultrasound in Medicine and Biology*, vol. 23, no. 6, pp. 911–920, 1997.

[72] R. Kiran V, J. Joseph, N. PM, and M. Sivaprakasam, "A dynamic time warping method for improved arterial wall-tracking using a-mode ultrasound frames: A proof-of-concept," *IEEE International Symposium on Medical Measurements and Applications*, pp. 1–6, 2020.

[73] S. G. Mallat and Z. Zhang, "Matching pursuits with time-frequency distributions," *IEEE Transactions on Signal Processing*, vol. 41, no. 12, pp. 3397–3415, 1993.

[74] S. W. Flax, N. J. Pelc, G. H. Glover, F. D. Gutmann, and M. McLachlan, "Spectral characterization and attenuation measurements in ultrasound," *Ultrasonic Imaging*, vol. 5, no. 2, pp. 95–116, 1983.

[75] A. Ng and J. Swanevelder, "Resolution in ultrasound imaging," *Continuing Education in Anaesthesia Critical Care & Pain*, vol. 11, no. 5, pp. 186–192, 2011.

[76] F. d'Astous and F. Foster, "Frequency dependence of ultrasound attenuation and backscatter in breast tissue," *Ultrasound in Medicine and Biology*, vol. 12, no. 10, pp. 795–808, 1986.

[77] E. Mor, A. Azoulay, and M. Aladjem, "A matching pursuit method for approximating overlapping ultrasonic echoes," *IEEE Transactions on Ultrasonics, Ferroelectrics, and Frequency Control*, vol. 57, no. 9, pp. 1996–2004, 2010.

[78] R. Demirli and J. Saniie, "Asymmetric Gaussian chirplet model for ultrasonic echo analysis," *IEEE International Ultrasonics Symposium*, pp. 124–128, 2010.

[79] Y. Lu and J. E. Michaels, "Numerical implementation of matching pursuit for the analysis of complex ultrasonic signals," *IEEE Transactions on Ultrasonics, Ferroelectrics, and Frequency Control*, vol. 55, no. 1, pp. 173–182, 2008.

[80] X. Zeng, Y. Zhang, Z. Li, J. Yang, L. Gao, and J. Zhang, "Locations of optimally matching Gabor atoms from ultrasound RF echoes for inter-scatterer spacing estimation," *Computer Methods and Programs in Biomedicine*, vol. 184, p. 105 281, 2020.

[81] R. Demirli and J. Saniie, "Model-based estimation of ultrasonic echoes part I: Analysis and algorithms," *IEEE Transactions on Ultrasonics, Ferroelectrics, and Frequency Control*, vol. 48, no. 3, pp. 787–802, 2001.

[82] M. Lian, H. Liu, Q. Bo, T. Zhang, T. Li, and Y. Wang, "An improved match-
      ing pursuit method for overlapping echo separation in ultrasonic thickness
      measurement," *Measurement Science and Technology*, vol. 30, no. 6, p. 06 501,
      2019.

[83] P. M. Shankar, "Ultrasonic tissue characterization using a generalized Nak-
      agami model," *IEEE Transactions on Ultrasonics, Ferroelectrics, and Fre-
      quency Control*, vol. 48, no. 6, pp. 1716–1720, 2001.

[84] M. S. O'Brien, A. N. Sinclair, and S. M. Kramer, "Recovery of a sparse
      spike time series by L1 norm deconvolution," *IEEE Transactions on Signal
      Processing*, vol. 42, no. 12, pp. 3353–3365, 1994.

[85] J. L. Rojo-Alvarez, M. Martinez-Ramon, J. Munoz-Mari, G. Camps-Valls,
      C. M. Cruz, and A. R. Figueiras-Vidal, "Sparse deconvolution using sup-
      port vector machines," *EURASIP Journal on Advances in Signal Processing*,
      pp. 1–13, 2008.

[86] K. F. Kaaresen and E. Bolviken, "Blind deconvolution of ultrasonic traces
      accounting for pulse variance," *IEEE Transactions on Ultrasonics, Ferro-
      electrics, and Frequency Control*, vol. 46, no. 3, pp. 564–573, 1999.

[87] C. Soussen, J. Idier, E. Carcreff, L. Simon, and C. Potel, "Ultrasonic nonde-
      structive testing based on sparse deconvolution," *Journal of Physics: Con-
      ference Series*, vol. 353, no. 1, p. 012 018, 2012.

[88] M. Alessandrini, L. De Marchi, and N. Speciale, "Recursive least squares
      adaptive filters for ultrasonic signal deconvolution," *IEEE International Sym-
      posium on Circuits and Systems*, pp. 2937–2940, 2008.

[89] D. Adam and O. Michailovich, "Blind deconvolution of ultrasound sequences using nonparametric local polynomial estimates of the pulse," *IEEE Transactions on Biomedical Engineering*, vol. 49, no. 2, pp. 118–131, 2002.

[90] D. Zhang, "Wavelet transform," in *Fundamentals of Image Data Mining*, Springer, 2019, pp. 35–44.

[91] G.-M. Zhang, D. M. Harvey, and D. R. Braden, "Resolution improvement of acoustic microimaging by continuous wavelet transform for semiconductor inspection," *Microelectronics Reliability*, vol. 46, no. 5-6, pp. 811–821, 2006.

[92] N. N. Tsiaparas, A. Gastounioti, S. Golemati, and K. S. Nikita, "Multiscale motion analysis of the carotid artery wall from B-mode ultrasound: Investigating the optimal wavelet parameterization," *IEEE International Conference on BioInformatics and BioEngineering*, pp. 1–4, 2013.

[93] Y. Lu, R. Demirli, G. Cardoso, and J. Saniie, "A successive parameter estimation algorithm for chirplet signal decomposition," *IEEE Transactions on Ultrasonics, Ferroelectrics, and Frequency Control*, vol. 53, no. 11, pp. 2121–2131, 2006.

[94] F. Boßmann, G. Plonka, T. Peter, O. Nemitz, and T. Schmitte, "Sparse deconvolution methods for ultrasonic NDT," *Journal of Nondestructive Evaluation*, vol. 31, no. 3, pp. 225–244, 2012.

[95] J. Kennedy and R. Eberhart, "Particle swarm optimization," *IEEE International Conference on Neural Networks*, vol. 4, pp. 1942–1948, 1995.

[96] J. Tang, G. Liu, and Q. Pan, "A review on representative swarm intelligence algorithms for solving optimization problems: Applications and trends," *IEEE Journal of Automatica Sinica*, vol. 8, no. 10, pp. 1627–1643, 2021.

[97] E.-G. Talbi, *Metaheuristics: from design to implementation*, 1st ed. John Wiley & Sons Inc., 2009.

[98] A.-L. Qi, G.-M. Z, M. Dong, H.-W. Ma, and D. M. Harbey, "An artifical bee colony optimization based matching pursuit approach for ultrasonic echo estimation," *Ultrasonics*, vol. 88, pp. 1–8, 2018.

[99] Y. Zhang, S. Wang, and G. Ji, "A comprehensive survey on particle swarm optimization algorithm and its applications," *Mathematical Problems in Engineering*, vol. 2015, 2015.

[100] B. Bassimir, A. Raß, and M. Schmitt, "Theory of particle swarm optimization: A survey of the power of the swarm's potential," *Information Technology*, vol. 61, no. 4, pp. 169–176, 2019.

[101] K. Zhang, T. Wu, Z. Duan, Q. Meng, and Q. Meng, "An adaptive approach for recovering overlapping echoes in oil film thickness measurement by ultrasound," *Industrial Lubrication and Tribology*, vol. 69, no. 5, pp. 788–797, 2017.

[102] S. Das, A. Papandreou-Suppappola, X. Zhou, and A. Chattopadhyay, "On the use of the matching pursuit decomposition signal processing technique for structural health monitoring," *Smart Structures and Materials 2005: Smart Structures and Integrated Systems*, vol. 5764, pp. 583–594, 2005.

[103] W. Liang, P.-W. Que, H.-M. Lei, and L. Chen, "Matching pursuit for decom-
       position and approximation of ultrasonic pulse-echo wavelet and its appli-
       cation in ultrasonic nondestructive evaluation," *Review of Scientific Instru-
       ments*, vol. 79, no. 7, p. 075 105, 2008.

[104] J. F. Polak, C. Johnson, A. Harrington, *et al.*, "Changes in carotid intima-
       media thickness during the cardiac cycle: The multi-ethnic study of atheroscle-
       rosis," *Journal of the American Heart Association*, vol. 1, no. 4, p. 001 420,
       2012.

[105] V. Shah and K. Balasubramaniam, "Effect of viscosity on ultrasound wave
       reflection from a solid/liquid interface," *Ultrasonics*, vol. 34, no. 8, pp. 817–
       824, 1996.

[106] A. Swillens, G. De Santis, J. Degroote, L. Lovstakken, J. Vierendeels, and P.
       Segers, "Accuracy of carotid strain estimates from ultrasonic wall tracking:
       A study based on multiphysics simulations and in-vivo data," *IEEE Trans-
       actions on Medical Imaging*, vol. 31, no. 1, pp. 131–139, 2012.

[107] I. Simova, "Intima-media thickness: Appropriate evaluation and proper mea-
       surement," *E-Journal of the ESC Council of Cardiology Practice*, vol. 13,
       no. 21, pp. 1–14, 2015.

[108] E. Randrianarisoa, R. Rietig, S. Jacob, *et al.*, "Normal values for intima-
       media thickness of the common carotid artery – an update following novel
       risk factor profiling," *Vasa*, vol. 44, no. 6, pp. 444–450, 2015.

[109] E. Jarauta, R. Mateo-Gallego, A. Bea, E. Burillo, P. Calmarza, and F.
       Civeira, "Carotid intima-media thickness in subjects with no cardiovascu-

lar risk factors," *Revista Espanola de Cardiologia (English Edition)*, vol. 63, no. 1, pp. 97–102, 2010.

[110] D. G. Altman and J. M. Bland, "Measurement in medicine: The analysis of method comparison studies," *Journal of the Royal Statistical Society: Series D (The Statistician)*, vol. 32, no. 3, pp. 307–317, 1983.

[111] E. Stensland-Bugge, K. H. Bønaa, and O. Joakimsen, "Reproducibility of ultrasonographically determined intima-media thickness is dependent on arterial wall thickness: The tromsø study," *Stroke*, vol. 28, no. 10, pp. 1972–1980, 1997.

[112] I. Moxham, "Understanding arterial pressure waveforms: Registrar prize," *Southern African Journal of Anaesthesia and Analgesia*, vol. 9, no. 1, pp. 40–42, 2003.

[113] F. Fritze, S. GroB, T. Ittermann, *et al.*, "Carotid lumen diameter is associated with all-cause mortality in the general population," *Journal of the American Heart Association*, vol. 9, no. 16, e015630, 2020.

[114] N. Denarie, J. Gariepy, G. Chironi, *et al.*, "Distribution of ultrasonographically-assessed dimensions of common carotid arteries in healthy adults of both sexes," *Atherosclerosis*, vol. 148, no. 2, pp. 297–302, 2000.

[115] R. Demirli and J. Saniie, "Model-based estimation of ultrasonic echoes part II: Nondestructive evaluation applications," *IEEE Transactions on Ultrasonics, Ferroelectrics and Frequency Control*, vol. 48, no. 3, pp. 803–811, 2001.

[116] N. Altman, "An introduction to kernel and nearest neighbor nonparameteric regression," *The American Statistician*, vol. 46, no. 3, pp. 175–185, 1991.

[117] P. J. Schmid, "Dynamic mode decomposition of numerical and experimental data," *Journal of Fluid Mechanics*, vol. 656, pp. 5–28, 2009.

[118] N. J. Kutz, S. L. Brunton, B. W. Brunton, and J. L. Proctor, *Dynamic Mode Decomposition*, 1st ed. Society for Industrial and Applied Mathematics, 2016.

[119] N. J. Kutz, X. Fu, and S. L. Brunton, "Multiresolution dynamic mode decomposition," *SIAM Journal on Applied Dynamical Systems*, vol. 15, no. 2, pp. 713–735, 2016.

[120] J. Gilles, "Empirical wavelet transform," *IEEE Transaction on Signal Processing*, vol. 61, no. 16, pp. 3999–4010, 2013.

[121] N. E. Huang, Z. Shen, S. R. Long, *et al.*, "The empirical mode decomposition and the Hilbert spectrum for nonlinear and non-stationary time series analysis," *Proceedings of the Royal Society of Mathematical, Physical and Engineering Sciences*, vol. 454, no. 1971, pp. 903–995, 1998.

[122] L. Ye and E. Keogh, "Time series shapelets: A new primitive for data mining," *International Conference on Knowledge Discovery and Data Mining*, pp. 947–956, 2009.

[123] M. Arul and A. Kareem, "Applications of shapelet transform to time series classification of earthquake, wind and wave data," *Engineering Structures*, vol. 228, p. 111 564, 2021.

[124] A. Swillens, J. Degroote, J. Vierendeels, L. Lovstakken, and P. Seger, "A simulation environment for validating ultrasonic blood flow and vessel wall imaging based on fluid-structure interaction simulations," *Medical Physics*, vol. 37, no. 8, pp. 4318–4330, 2010.

[125] S. Balocco, O. Basset, J. Azencot, P. Tortoli, and C. Cachard, "3D dynamic model of healthy and pathologic arteries for ultrasound technique evaluation," *Medical Physics*, vol. 35, no. 12, pp. 5440–5450, 2008.

[126] J. Stoitsis, S. Golemati, V. Koropouli, and K. Nikita, "Simulating dynamic B-mode ultrasound image data of the common carotid artery," *IEEE Workshop on Imaging Systems and Techniques*, pp. 144–148, 2008.

[127] C. Wang, X. Li, H. Hu, Z. Lin, and Z. Huang, "Monitoring of the central blood pressure waveform via a conformal ultrasonic device," *Nature Biomedical Engineering*, vol. 2, pp. 687–695, 2018.

[128] J. Kang, Y. Kim, W. Lee, and Y. Yoo, "A new dynamic complex baseband pulse compression method for chirp-coded excitation in medical ultrasound imaging," *IEEE Transactions on Ultrasonics, Ferroelectrics, and Frequency Control*, vol. 64, no. 11, pp. 1698–1710, 2017.

[129] N. Wang, C. Yang, J. Xu, *et al.*, "An improved chirp coded excitation based on compression pulse weighting method in endoscopic ultrasound imaging," *IEEE Transactions on Ultrasonics, Ferroelectrics, and Frequency Control*, vol. 68, no. 3, pp. 446–452, 2020.

[130] C. F. Otesteanu, S. J. Sanabria, and O. Goksel, "Robust reconstruction of elasticity using ultrasound imaging and multi-frequency excitations," *IEEE Transactions on Medical Imaging*, vol. 37, no. 11, pp. 2502–2513, 2018.

[131] K. P. Mercado-Shekhar. (2015). "Types of ultrasound scattering," [Online]. Available: `https://www.researchgate.net/figure/Types-of-ultrasound-scattering-A-Specular-scattering-occurs-when-the-structure-is_fig2_280444277` (visited on 06/20/2021).

[132] (2021), [Online]. Available: `https://www.jaypeedigital.com/eReader/chapter/9789352700929/ch1` (visited on 08/12/2021).